Communicated by Prof. Dr. Janos Urai

Rheinisch-Westfälisch Technische Hochschule Aachen
Fakultät für Georessourcen und Materialtechnik
Lehr- und Forschungsgebiet Geologie - Endogene Dynamik

Microveins in Limestones of the Oman Mountains - A Structural Study of the Fundamental Building Blocks of a Crack-Seal-System

B. Sc.-Thesis
Christian Meeßen



Supervisor:
Prof. Dr. Janos L. Urai

Christian Meeßen
Chr.-Jos.-Matzerath Str. 20
52441 Linnich

Hiermit erkläre ich an Eides statt, dass ich die von mir vorgelegte Arbeit selbstständig verfasst habe, dass ich keine weiteren Hilfsmittel als die angegebenen benutzt habe.

Darüber hinaus erkläre ich mein Einverständnis, dass diese Arbeit eingesehen werden darf und Auszüge daraus kopiert werden dürfen. Bibliographische Angaben zu dieser Arbeit dürfen sowohl im Bibliothekskatalog als auch auf den Internetseiten des Lehr- und Forschungsgebietes Geologie - Endogene Dynamik, des Geologischen Instituts und der Hochschulbibliothek der RWTH Aachen verzeichnet werden.

Aachen, den 19.09.11

_____

Christian Meeßen

Die vorgestellten Arbeiten sind Teil des DGMK- Projektes 718 ,,Mineral Vein Dynamics Modelling“. Das Vorhaben wird von den Firmen ExxonMobil Production Deutschland GmbH, GDF SUEZ E&P Deutschland GmbH, RWE Dea AG und Wintershall Holding GmbH im Rahmen des E&P-Forschungsfonds des WEG Wirtschaftsverband Erdöl- und Erdgasgewinnung e.V. gefördert.

Abstract - Crack seal is a ubiquitous process in the upper crust. It has been studied and know for a long time but it's details are not well understood. In particular the individual events of crack seal have not been studied in great detail. In this work microveins are hypothesized to be the fundamental building blocks representing one crack-seal event and that they have a minimum opening aperture. In this study rocks from the Oman Mountains were sampled which contain a wide range of calcite veins in limestone and it was aimed to find rock samples which were devoid of veins. Many of these rock samples do not have macroscopic veins. In all these samples many microveins were found and based on a series of criteria to identify veins that belong to single crack-seal events they were selected and their properties were analyzed. The microveins typically are coarser in grain size than the surrounding matrix and based on the observed data the hypothesis that there is a minimum opening width of crack seal veins can not be rejected. The coarser grain fill is epitaxially grown inside the grain-boundary fractures in the matrix. It is proposed that these microveins represent the fundamental building blocks of crack seal and are the product of one crack seal event.

Zusammenfassung - Crack-Seal ist in der oberen Kruste ein ubiquitärer Prozess. Er wurde bereits seit langem eingehend untersucht aber die genauen Vorgänge sind bisher nicht ausreichend verstanden. Besonders die Einzel-Events der Crack-Seal-Prozesse wurden nur periphär behandelt. Die zentrale Hypothese dieser Arbeit besagt, dass Microveins die Grundbausteine des Crack-Seal-Prozesses sind und dass diese eine minimale Apertur besitzen. Hierfür wurden in den Bergen von Oman Proben in größtmöglichem Abstand zu makroskopischen Veins genommen. Viele dieser Proben enthalten keine makroskopischen Veins, weisen aber eine hohe Dichte an Mikroveins auf. Basierend auf einer Reihe von Kriterien, die eine Unterscheidung zwischen Veins aus einem oder mehreren Bruchereignissen ermöglichen, wurden Einzel-Event-Veins identifiziert und auf ihre Eigenschaften untersucht. Im Allgemeinen wuchs der Zement der Mikroveins epitaxial innerhalb der Brüche und wies eine gröbere Korngröße als die der umgebenden Matrix auf. Die Brüche propagierten zwischen den Körnern der Matrix, durchschlugen aber Körner die wesentlich größer als die Korngröße der Matrix waren. Basierend auf den Ergebnissen der Untersuchungen konnte die Hypothese einer minimalen Apertur nicht widerlegt werden.

Contents

Contents iii

1. Introduction 1
- 1.1. Motivational background . . . 1
- 1.2. Tectonic setting . . . 2
- 1.3. About Veins . . . 4
  - 1.3.1. Fracture mechanics . . . 4
  - 1.3.2. What are veins and why do we see them? . . . 6
  - 1.3.3. Crack-Seal processes . . . 7

2. Methods 8
- 2.1. Hand specimens . . . 8
  - 2.1.1. Sampling . . . 8
  - 2.1.2. Sample preparation . . . 9
  - 2.1.3. Sample digitization and measuring . . . 10
  - 2.1.4. Data processing . . . 11
- 2.2. Thin sections . . . 12
  - 2.2.1. Preparation . . . 12
  - 2.2.2. Thin section digitization and measuring . . . 12
  - 2.2.3. Data processing . . . 15
- 2.3. SEM analysis . . . 21

3. Observations and results 22
- 3.1. Hand specimens . . . 22
- 3.2. Thin sections . . . 24
- 3.3. SEM Imagery . . . 35
- 3.4. Vein description . . . 39
  - 3.4.1. Spatial distribution and orientation . . . 39
  - 3.4.2. Aperture and Length . . . 41
  - 3.4.3. Microfabric . . . 45
  - 3.4.4. Interaction . . . 50
  - 3.4.5. Microvein types . . . 52

4. Discussion 53
- 4.1. One event criteria . . . 53
- 4.2. Structure . . . 53
- 4.3. Aperture distribution . . . 56
  - 4.3.1. Monte Carlo Simulation . . . 56

5. Conclusion 62

6. Outlook 62

7. Acknowledgements **64**

References **65**

A. MATLAB Code **67**
A.1. Spatial orientation calculation 67
A.1.1. StrikeDipEW_HOR.m 67
A.1.2. StrikeDipNS_HOR.m 68
A.1.3. readPS.m 71
A.1.4. stere32.m 71
A.2. Automated aperture measurement 72
A.2.1. execute_me.m 72
A.2.2. aperture.m 73
A.2.3. process.m 74
A.3. Modelling aperture distribution 76
A.3.1. model.m 76

B. Outcrops **80**

C. Additional material **87**

D. Field measurements **89**

E. Data DVD **91**

1. Introduction

This thesis presents the investigation of limestone rock samples that were taken from the Oman Mountains. The samples were investigated at meter to 100 nanometer scale to study structure and attributes of microveins. Additional information, mainly orientation-data, about microveins was collected in the field. The fundamental question I would like to address in this work is whether microveins have specific properties that can be used to understand their origin and whether microveins are the consequence of one crack-seal event and therefore the fundamental building blocks of crack seal processes. This thesis is an attempt to answer these questions. The following subsections present the motivation to carry out this study together with an introduction to basic fracture mechanics.

All images of this study as well as the MATLAB® Scripts are attached as DVD at the end of the thesis.

1.1. Motivational background

In literature microveins have several different names. They can be called *veinlets* (Becker et al., 2011; Holland and Urai, 2010), *hairline veins* (Paulsen et al., 2002) or *mineralized microfractures* (Wang and Sun, 1990) and they are basically all the same thing. The are typically less than a millimeter thick, sometimes only visible by the microscope and filled with a mineral that can be same as the matrix or different. But often the term "microvein" is used interchangeably as fracture even though fractures are open voids and veins are mineralized former fractures. However, in many study veins are called fractures.

There is a wide and well established fundamental knowledge regarding the structure and statistics of fractures (Atkinson, 1989; Wong et al., 1989; Wang and Sun, 1990; Twiss and Moores, 2007) while there is very little known about structure and statistics of veins.

On one hand in many studies fracture aperture correlates with fracture length (Vermyle and Scholz, 1995; Olson, 2003) and suggests that fractures opening occurs at all scales. On the other hand, due to equidistant host rock flakes, inclusion bands suggest that there is a minimum vein aperture (Ramsay, 1980; Renard et al., 2005; Holland and Urai, 2010). They form in veins where the cracking occurs at the vein matrix boundary many times after the other. In contrast microveins form when the fracturing is delocalized, which is the main difference between inclusion bands and microveins. This was the initial idea in the crack-seal theory proposed in 1980 by John G. Ramsay (Sec. 1.3.3). Another

example of crack-seal microstructures is found in vein tip splays where one macroscopic vein branches into large bundles of microveins (Holland and Urai, 2010). These bundles were interpreted to have formed by a very large number of crack-seal events where many crack-seal events only occurred once and formed a microvein. Statistics of the size of inclusion bands suggest that there is a minimum size so one can ask: Are microveins distributed in such a way that there is a minimum size? How big is these increments?

A second motivation for this study is to better understand the timing and occurrence of microveins in Jabal Akhdar Anticline. When were the microveins formed? Are all microveins older or younger than macroveins or did they form contemporaneously?

This study gives an insight into microvein structures and their general occurrence throughout the Jabal Akhdar Anticline, using field work observations as well as light and scanning electron microscopy. This thesis attempts to test the hypothesis of minimum vein apertures and suggest improvements for further investigations.It is an approach to tackle the challenge of minimum vein apertures and gives an outlook for further investigation methods and enhancements of the used techniques.

1.2. Tectonic setting

The investigated area is situated on the south-western flank of the Jebel Akhdar window (Fig. 1).

The Jebel Akhdar window consists of an anticline with a wavelength of 70 km and an amplitude of at least 3 km (Searle, 1985). The anticline axis strikes WNW-ESE and bends at the eastern part of the Jebel Akhdar window towards NNE until it bends again towards ESE, passing over to the Saih Hatat window (Searle, 2007). It contains a Pre-Permian basement that is unconformably overlain by autochthonous Permian to late Cretaceous carbonates of the Hajar-Unit. Those are overridden by the allochthonous Hawasina Nappes and Samail Ophiolites (Breton et al., 2004).

In the course of closing Neotethys since Cenomian a subduction zone developed in the Arabian Plate associated with the North Muscat Microplate. The autochthonous sediments at Jebel Akhdar were deformed and subducted up to temperatures of 200 °C and pressures of 4 kb at the south-western flank (Breton et al., 2004). The studied area mostly contains upper Anchizone facies rocks. After a northeastward movement of the North Muscat plate the former subducted autochthonous units came in direct contact to Hawasina Nappes and the overlying oceanic crust in late Campanian (Breton et al., 2004). Afterwards Jebel Akhdar anticline was formed during Maastrichtian to Paleocene times and was most likely finally uplifted by late Tertiary compression (Poupeau, 1998).

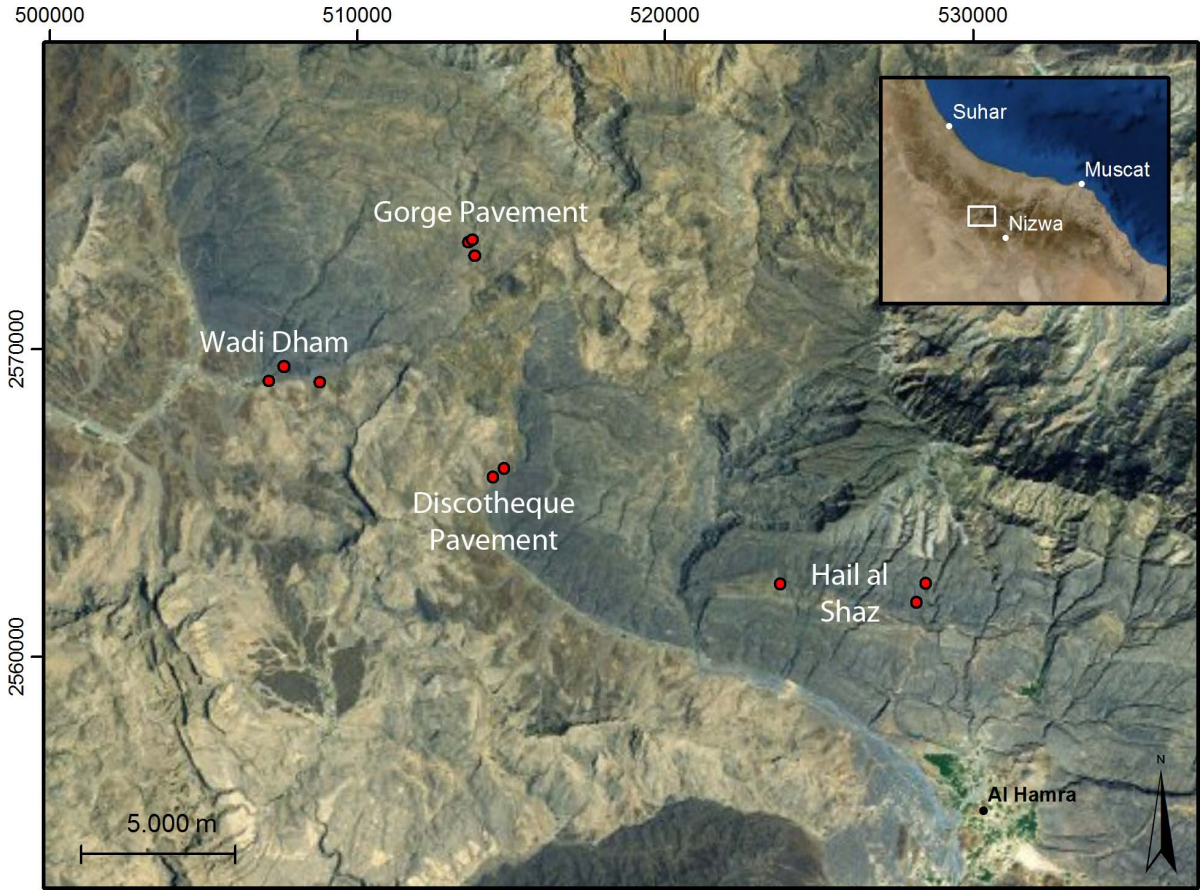


Figure 1: Overview of the investigated area. The box in the small map in the upper right corner shows the pane of the detailed map. Red dots illustrate the sampling spots. The dark brown-black rocks in the South are Ophiolites, the light brownish rocks belong to the Hawasina Nappes and the blueish rocks are autochthonous limestones.

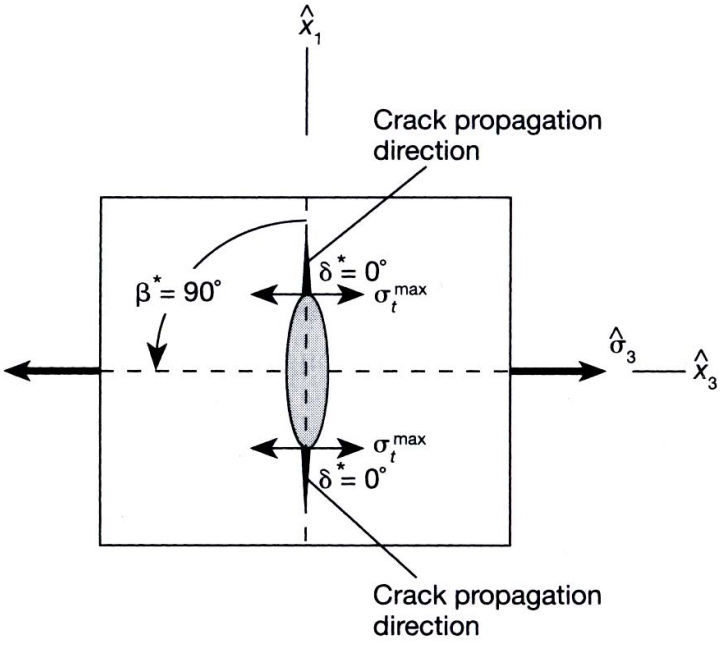


Figure 2: Illustration of a Griffith crack, oriented parallel to σ_1. The maximum tensile stress is located at $\delta^* = 0°$ resulting in a crack propagation direction perpendicular to σ_3 (Twiss and Moores, 2007).

1.3. About Veins

This section gives a short introduction into fracture mechanics, explains what veins consist of and why they can be seen in the microscope. At the end the principles of crack-seal processes are outlined.

1.3.1. Fracture mechanics

The Griffith Theory of fracture describes the formation of joints in solids. Therefore it is assumed that the whole rock is penetrated with submicroscopic ellipsoidal cracks with a randomly distributed orientation. These cracks represent weaknesses in crystals or matrix and have a much larger diameter than aperture. By this property cracks reduce the tensile strength of the material since the amount of stress depends on the relation of aperture versus length. Once the rock is prone to tensile stress, cracks having an orientation parallel to σ_1 accumulate the stress at their tip (Fig. 2). Thus the tensile strength can be exceeded locally although the general applied stress is subcritical. If the applied tension is bigger than the tensile strength the crack propagates and only stops when the criteria for fracture propagation are not satisfied anymore (e.g. by reaching an area of insufficient driving stress) (Twiss and Moores, 2007).

Stress applied on a rock can be visualized using the two-dimensional Mohr Circle diagram. The stresses σ_1 (maximum stress) and σ_3 (minimum stress) are applied onto a plane orientated randomly in space (Fig. 3, right hand side), defining θ as the small

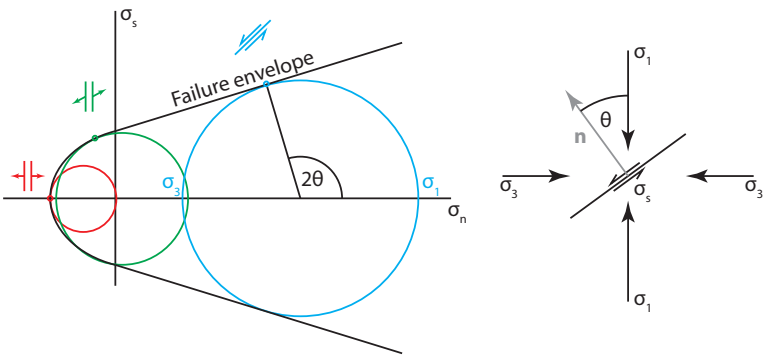


Figure 3: Left hand side: Mohr Circle diagram for two-dimensional stress, illustrating the three basic types of fractures. Red: pure extension fractures, green: mixed mode fractures, blue: shear fractures. Right hand side: illustration of randomly orientated plane with applied principal stresses σ_1 and σ_3.

angle between σ_1 and $\mathbf{n}$, where $\mathbf{n}$ represents the plane's surface normal vector. The stress state of a plane can also be defined by shear stress σ_s, parallel to the plane's surface, and normal stress σ_n, normal to the plane's surface. Plotting both stress values into one diagram results in the Mohr's diagram (Figure 3 left hand side). A stress system is characterized by σ_1, σ_3 and θ and can then be visualized in the Mohr's diagram. Therefore stresses σ_1 and σ_3 are plot onto the abscissa. Drawing a circle around the center $(\sigma_1 + \sigma_3)/2$ leads to all possible states of stress of a plane of any orientation. The plane's orientation is defined by the angle 2θ, rotating counterclockwise around the circle's center. The intersection point of a line, defined by 2θ and the circle represents the shear and normal stresses applied on a plane. The material hosting the plane is represented by a failure envelope where the intersection point represents cohesion and the slope for $\sigma_n > 0$ is defined by the internal friction Φ. If a Mohr circle reaches the failure envelope, the rock fails. The colored circles represent the three basic types of fractures that can be described by a Mohr diagram. The red circle represents pure tension fractures which only appear for σ_1 and σ_3 less than zero. Mixed mode fractures (green) occur for tensile σ_3 and compressive σ_1 while shear fractures (blue) are produced for compressive σ_1 and σ_3 (Twiss and Moores, 2007).

Fractures are created by stress applied on a material which acts brittle reaching it's failure criterion. Stress σ hereby is defined as force F per area A. Generally fractures are classified into three different types: Mode I fractures open perpendicular to the crack's surface by tensile force. Mode II and mode III arise of in-plane and anti-plane shear (see Fig 4). The crack-hosting material is assumed to act linear elastic, however, many materials also act non-linear at the very crack tip. Whether a crack propagates or not depends on the stress next to the crack's tip. The stress is proportional to $1/\sqrt{r}$ where r represents the distance from the crack tip. So the stress concentrates next to the crack tip and tends towards infinity for small r thus making it possible to

reach the fracture criterion of the material. Furthermore the criterion of propagation is influenced by a coefficient K, the stress intensity factor, describing additional external parameters like applied load or the body's shape. It is defined as $K = Y\sigma_r \ (\pi c)^{1/2}$ for a two dimensional crack of any mode. The modification factor Y describes external factors such as crack geometry or loading conditions, σ_r represents external applied stress and c describes the half crack length. A fracture propagates if the stress intensity factor is reached by changing external conditions, resulting in a fast crack propagation that may reach the speed of sound of the hosting material. However, some cracks also propagate below the critical value of K (called subcritical crack growth). As the speed of crack propagation depends on K, Figure 5 shows the general relationship between stress intensity factor and crack velocity where K_C represents the critical stress intensity value. Crack propagation starts at a minimum stress intensity K_0 by subcritical crack growth. The crack velocity rises with larger stress intensity factors and leaps towards much higher velocities, reaching K_C, speaking of dynamic crack growth. At very high stress intensity factors also crack branching may occur (Atkinson, 1989).

1.3.2. What are veins and why do we see them?

Veins arise from fractures by mineralization. After a crack is formed it is filled with a fluid providing the material for crystal growth. Additionally veins can contain information about their opening for example by mineral lineations (Twiss and Moores, 2007). Crack-seal processes, which are a special kind of microstructure, are introduced in the following Section 1.3.3 and show that one vein does not necessarily represent one fracture.

Veins generally can be recognized as linear features mostly showing a different mi-

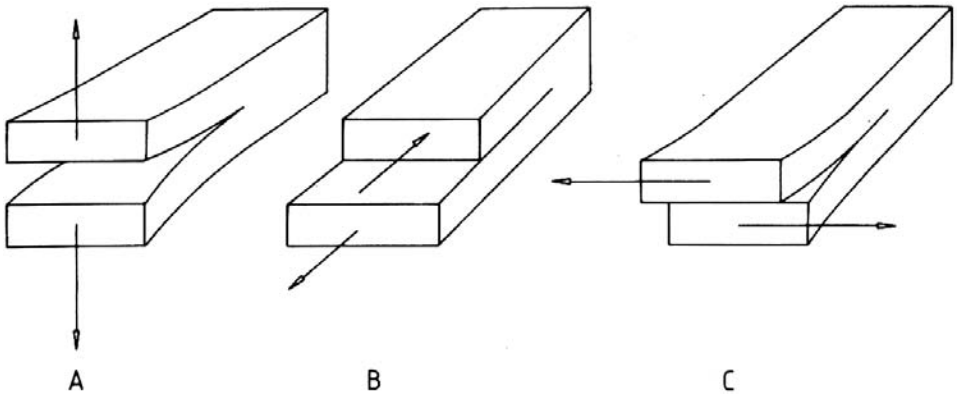


Figure 4: Three principal fracture modes. A: Mode I, B: Mode II, C: Mode III (Atkinson, 1989)

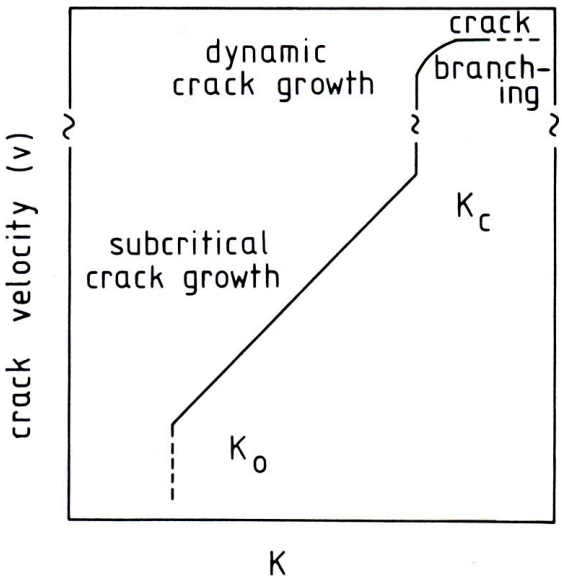


Figure 5: Basic crack propagation phases, depending on stress intensity factor K. K_0 represents minimum stress intensity for crack propagation. K_C marks the changeover from subcritical crack growth to dynamic crack growth (after Atkinson, 1989).

crostructure and high contrast to the surrounding rocks depending on their mineral cement. Their bright appearance is either due to frequent fluid or gas inclusions in the crystals scattering the light or their inherent color. Observing microveins in microscopical analysis shows veins as bright lines as well. But in contrast the veins are recognizable since the light is scattered by the host rock. In the limestones of the examined area micrite grains create a strong inhomogeneity in the thin section and disperse the transmitting light into every direction. Thus the light passes with less interaction where the inhomogeneity is lower. This is mainly in microveins or fossils.

1.3.3. Crack-Seal processes

Crack-seal processes were firstly introduced by Ramsay in 1980 who published "The crack-seal mechanism of rock deformation" (Ramsay, 1980). Based on inclusion band microstructures he reasoned that some veins are formed of multiple events which are an alternating sequence of fracturing and healing of rocks. Ramsay proposed that at first fluid-filled microfractures develop which afterwards are sealed with crystals. The material for this crystal growth was transferred by pressure solution from the host rock into the microfracture. Repeating this process leads to multiple inclusion bands with antitaxially orientated crystals (Fig. 6). The inclusion bands usually consist of host rock fragments detached from the interface (Ramsay, 1980).

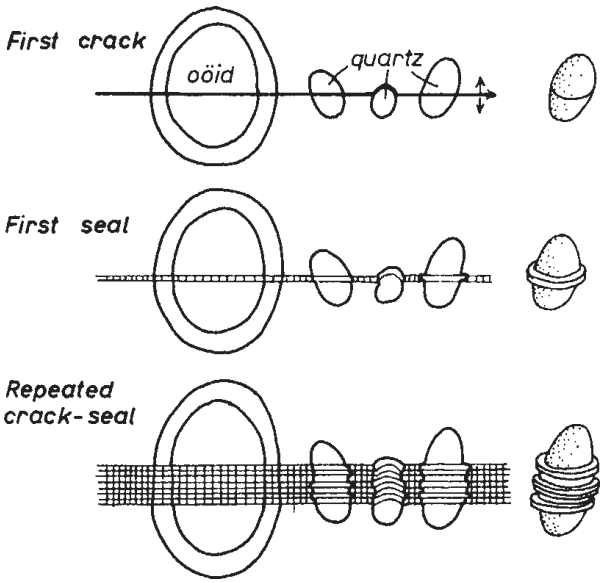


Figure 6: Simplified illustration of crack-seal processes (Ramsay, 1980).

2. Methods

The methods used to acquire results are explained as followed. At first hand specimen were collected in the field to gain more detailed information in the laboratory about microveins. The samples were formatted to smaller specimen after a systematic cutting procedure. This was followed by scanning the polished surfaces to acquire first information about azimuth and dip. Afterwards some samples were chosen to create thin sections for microstructural analysis. This analysis was conducted manually as well as semi-automatic. As the last step one specimen was studied in a scanning electron microscope (SEM) which allowed observation of microvein structures at much higher magnifications.

2.1. Hand specimens

The procedure of hand specimens preparation will be explained in the following subsections. Hand specimens were taken to support fieldwork based information with microstructural analysis. Therefore mainly computer-based methods were used.

2.1.1. Sampling

Taking samples in the field requires their orientation to be marked carefully. To ensure a clear sample orientation when formatting them in the laboratory the horizontal plane

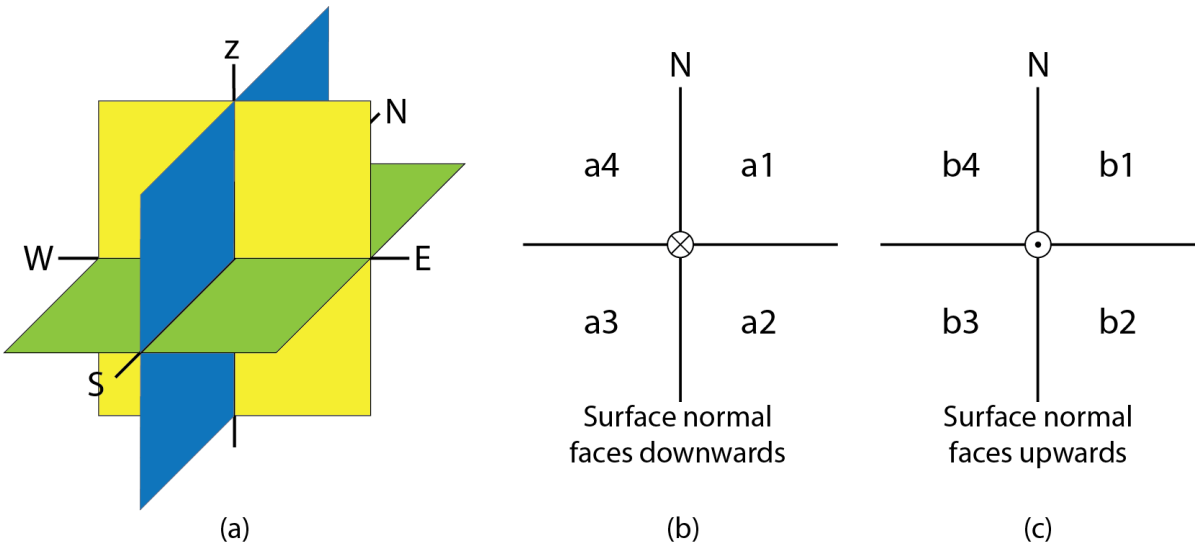


Figure 7: (a) Illustration of cut planes in different colors; blue: NS-cut, yellow: EW-cut, green: horizontal cut. (b) and (c) show the naming of the quadrants for further data processing.

and magnetic north have been marked on the sample. The declination in Oman is between 0 and 2° (NOAA/NGDC & CIRES, 2009) and can, referring to the reading error, be neglected.

2.1.2. Sample preparation

For azimuth- and dip-calculation three orthogonal planes were cut into the samples. The surface normals point vertical, north-south and east-west, making it possible to calculate dip and dip-direction efficiently. Each plane of the cut hand specimen was polished using an abrasive with a grain size of 1200 grit.

For further handling (see Sec. 2.1.4) each sample was formatted to sub-samples, classified into one of eight specific sections. Figure 7 illustrates all possible sections and their nomenclature. Sub-samples located in the a-quadrants have surface normals pointing downwards which means that the sample can be classified as one of the sections above the green plane in Figure 7a. Accordingly all b-quadrant specimen belong into one section of the space below the green plane. An example specimen for quadrant a_2 is shown in Figure 8a. For the orientation analysis it is important that in each stitched image one plane must be horizontal facing North upwards and East to the right as shown in Figure 8. Otherwise the calculation algorithm would become too complicated (see Sec. 2.1.4).

2.1.3. Sample digitization and measuring

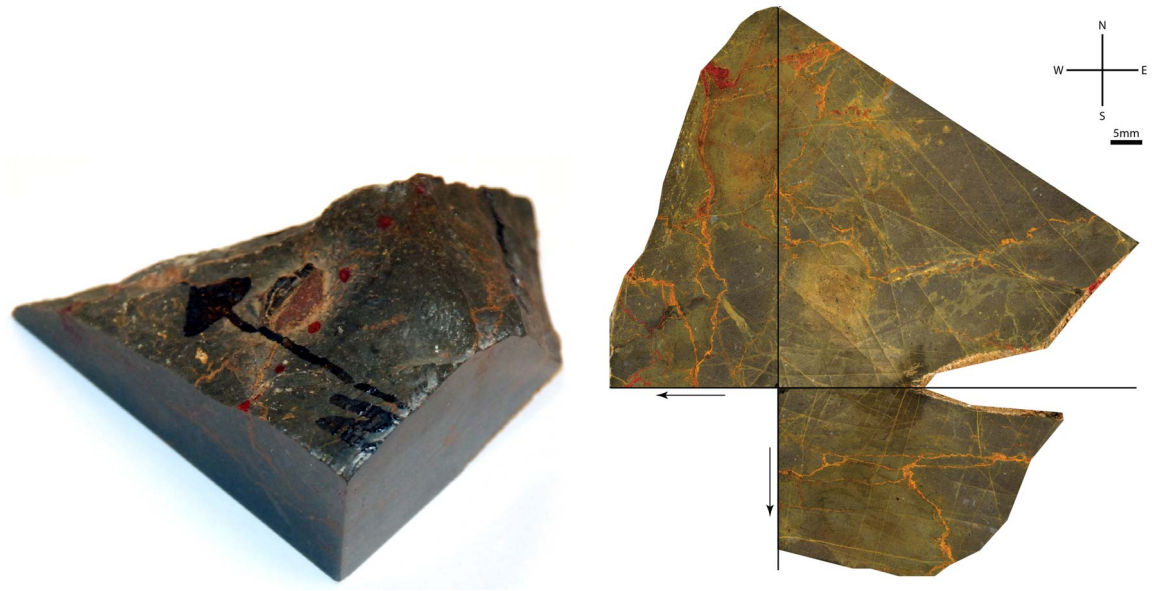
The grinded planes were scanned at a resolution of 4800 DPI using an Epson Perfection 2450 Photo scanner. To achieve maximum contrast, as well as to reduce refraction and deflection at the interface, a thin water film was applied between scanner and sample.

Resolution power

The resolution power of scanning at 4800 DPI is theoretically at 5.3 μm per pixel. However, the true resolution has been estimated to 20 μm by examining the level of detail in the imagery.

Processing

The scanned images of the planes were assembled together so that features that turn around corners are connected (Fig. 8 b). Afterwards the intersection lineation of microveins and cutting planes were measured using the Ruler Tool of Adobe Photoshop CS 5 ®. Then the resulting azimuth and pseudo dip were computed using MATLAB ®.



(a) (b)

Figure 8: (a) Sample CM002 after preparation. The Sub-sample is allocated in quadrant a_2 as the north arrow on top of the sample shows. (b) Scanned and stitched images of sample CM002. The top right plane is horizontal while the vertical NS- and EW-planes are stitched to the appropriate sides of the image. The arrows placed adjacent to the cuts point upwards. Note that the images are mirrored so that the viewpoint for the stitched image seems to be situated in the specimen.

2.1.4. Data processing

Since the coordinate system of Photoshop CS 5 ® an not be changed for personal needs the measured angles firstly were converted into appropriate angles of strike and pseudo dip.

For this purpose for each quadrant a specific algorithm was written. In this section only a rough overview over the workflow is given while the precise procedure including all MATLAB ® scripts can be found in the appendix (A.1 ff.) and on the DVD.

Figure 9 shows the simplified workflow of the programmed MATLAB ® scripts. From Photoshop a text file was exported that contains information as the angle of the measured feature in the Photoshop CS ® coordinate system. Because for calculation of a plane at least two support vectors are needed, the datafile contains alternating records of angles either from the horizontal plane or from a vertical plane. At first the script separates the angle pairs into two arrays. Thereafter strike is obtained immediately from the horizontal plane angle. For pseudo dip calculation the quadrant of the sample has to be determined at first (see 2.1.2). Afterwards the surface normal vector is calculated using supporting vectors that are defined by pseudo dip and strike. The dip δ can now be calculated by

$$\delta = \frac{\pi}{2} - asin\,(n_z) \tag{1}$$

where n_z is the z-component of the surface normal vector. For dip direction calculation, which is a coordinate transformation from cylindrical to cartesian coordinates, at first a variable ξ must be defined by

$$\xi = \frac{n_x}{|n_x|} \cdot acos\,(n_y) \tag{2}$$

with n_x,n_y as components of the surface normal vectors. The variable ξ defines which of the following cases must be used to calculate the dip direction γ:

$$\gamma = \begin{cases} \frac{\pi}{2} + \frac{n_x}{|n_x|} \cdot acos\left(\frac{n_y}{\|\mathbf{n}\|}\right) & \text{if } \xi < 0, \\ \frac{n_x}{|n_x|} \cdot acos\left(\frac{n_y}{\|\mathbf{n}\|}\right) & \text{if } \xi \geq 0. \end{cases} \tag{3}$$

The vector $\mathbf{n}$ is the surface normal vector of the microveins' plane. At the very end the script writes a Stereo32 compatible output file containing all dip and dip direction values that allows stereographic plots.

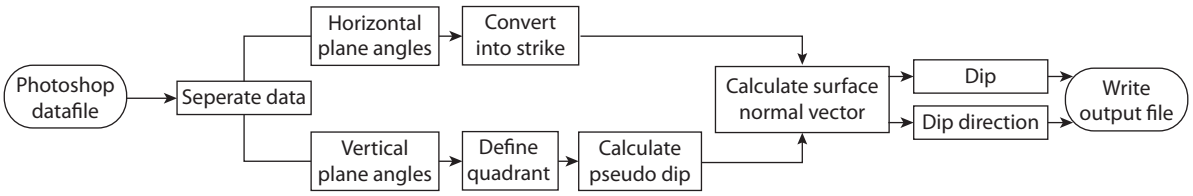


Figure 9: Simplified workflow of MATLAB ® script for calculation of dip and dip-direction.

2.2. Thin sections

Scanned hand specimen reveal information about dip and dip direction as well as age relationships and apertures of veins in mm-scale. To obtain more detailed information, for example about microstructures and apertures in μm-scale, creation of thin sections is necessary. The following sections briefly describe the process from preparation, digitizing to data processing.

2.2.1. Preparation

The scanned images of all samples allow to select interesting spots of investigation for thin sections. Further information about selection criteria are given in section 3. After selecting spots the rock samples were glued on a microscope slide and cut to a thickness of about 2 mm. Then they were polished to a thickness of about 30 μm and covered with a coverglass.

2.2.2. Thin section digitization and measuring

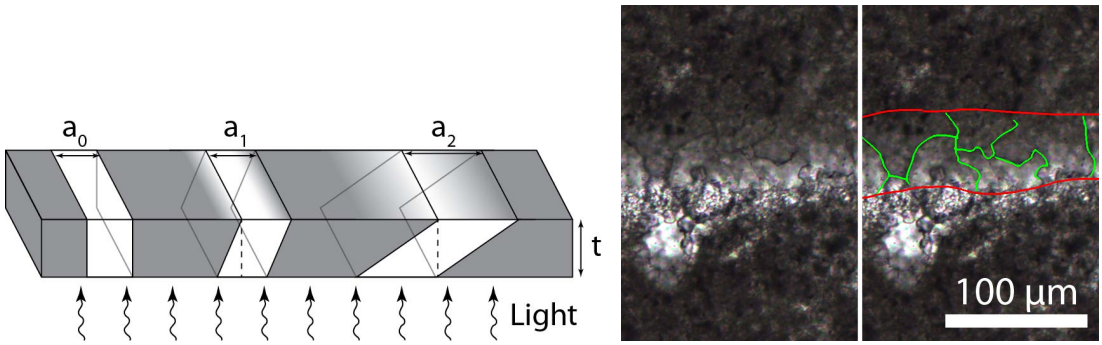
For sample digitization a ZEISS AXIO Scope.A1 microscope with an attached AxioCam ICc3 was used. The overview images were shot using an EC Epiplan-NEOFLUAR 1,25x/0,03 objective while all detail images and measurements were conducted using an EC EPIPLAN 20x/0,04 objective.

Resolving power

According to ZEISS' AcquisitionAdvisor 2.0 ® software the resolving power of the microscope can be estimated using the formula:

$$d_{real} = 0,6\frac{\lambda}{N_A} \tag{4}$$

Where d is the minimum distance of two points to be distinguished using the wavelength λ and the objectives numerical aperture N_A. This leads to a minimum resolving power for the 20x-objective ($N_A = 0.4$) of 975 nm using red light ($\lambda = 650nm$) or 675 nm



(a) (b)

Figure 10: (a) This diagram illustrates two problems of microvein measurement in thin sections. Three veins of equal aperture a_0 are cut in different angles with respect to the thin section plane. (b) Microscopic image from sample CM004. Left hand side shows the original image with gradient caused by high cutting angle and too thick thin section. Right hand side shows the vein border (red) and the grain boundaries (green) as interpreted manually.

using blue light ($\lambda = 450\,nm$). Since the images were shot using polychromatic light, the maximum resolving power is estimated with 975 nm. Using the 20x-objective the ICc3 camera creates images with a resolution of 0.3432 nm per pixel. Hence two features can only be differentiated if they are at least three pixel apart which means the final resolving power is about 1 μm.

Setup and problems

Measuring microvein apertures in thin sections seems trivial at first but turned out to be challenging. Generally microveins in thin sections with a thickness of 30 μm can examined best by using non-polarized light. Unlike that super-thin thin sections show very low contrast in non-polarized light (Fig. 36, p. 48). Therefore usage of parallel polarized or cross-polarized light is necessary. Two main problems (cutting angle and thin section thickness) occurred and will be described in the following paragraphs. A third problem (interface roughness) showed up during interpretation and will be discussed in Section 4.2.

A - Cutting angle

The first error occurs when veins are cut in any angle to the section plane. Then the aperture always is measured as apparent aperture (Fig. 10) which always is larger than the true aperture. Figure 11 shows the dependency between relative deviation from true aperture and cutting angle which can be derived from $a_a = a_0/sin\alpha$ with a_a as apparent aperture, a_0 as true aperture and cutting angle α. Accepting an error of 10 % on the

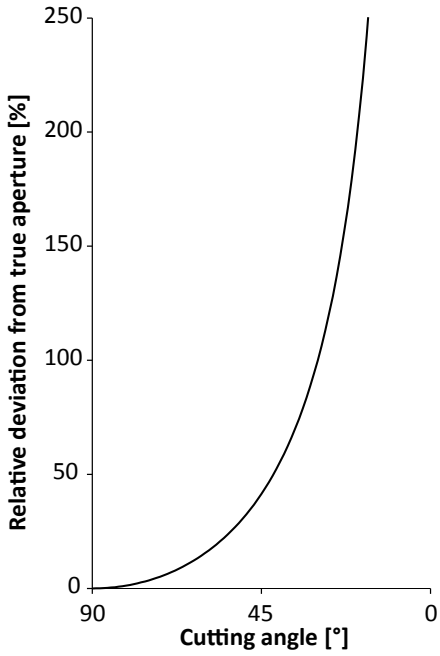


Figure 11: Relation between cutting angle and relative deviation from true aperture.

apparent aperture to assume it as true aperture leads to an allowed cutting angle of up to about 65°. Above this angle the true aperture should be recalculated.

B - Thin section thickness

Because thin sections have a certain thickness another effect occurs which makes the vein-host rock interface fuzzy. A gradient illumination develops with its brightness peak where the vein has the biggest thickness perpendicular to the thin sections' surface. The brightness declines from this point towards the host rock. Figure 10 a illustrates this effect and shows that the true vein-host rock interface is located where the gradient changes to white or grey. The large images in Figure 12 show crosscuts of thin sections containing microveins with apertures of 1 and 3 μm, intersecting the thin sections in different angles from 90 to 60°. Noise was added to simulate light scattering by micrite grains. The smaller images display the average colors of each column and so represent the top views as they would be observed through a microscope. The simulation shows that veins with apertures about 1 μm can barely be detected if they intersect at an angle lower than 70°. Thus the resolution power can be reduced severely if small microveins intersect at low angles, which produces a LHT fall-off (Pickering et al., 1995).

By focussing the topmost layer of the thin section, aperture can still be measured by examining grain boundaries (Figure 10b, right hand side). Thus automated microvein analysis is not well applicable for thin sections unless they are super thin. For more proposals regarding enhancements of measurements see Section 6.

As a consequence of issues with thin section thickness several measurements were done manually. Some veins, showing good conditions for automated measuring, were measured semi-automatic using a simple MATLAB® algorithm which is explained in the following Subsection.

C - Interface roughness

As showed later, there is another aspect regarding very thin veins and the roughness of the host rock interface. This issue is described in Section 4.2

2.2.3. Data processing

For detailed investigation two extending en-echelon veins were analyzed using MATLAB®. Observations to derive from automated analysis are detailed aperture distribution, sinuosity as well as relation between length and aperture. First attempts using a Sobel filter (Mathworks, 2011) for edge detection failed since the observed microveins are in the same order of size as the noise produced by the host rock. Thus the best way is to manually discretize veins. Because manual interpretation involves subjectivity and is relatively tedious the veins were discretized using a semi-automatic discretization which is explained in the following.

At first the whole microvein was photographed in 200-fold magnification (Fig. 14 a). Adjusting tonal values in AxioVision® software was conducted to create a higher contrast of vein cement versus host rock. The values were adjusted so that the vein appeared white representing the vein interface as best as possible. Applying a threshold afterwards allowed to create a binary image of the vein (Fig. 14 b). The discretization reveals that the images contain a lot of noise at the surrounding of the microveins. This noise is produced by micrite grains scattering the light. One possibility to reduce the noise would usually be an erosion and dilation algorithm. Therefore the image firstly would be eroded, which means the white areas would be shortened. But this would not only reduce the noise but also reduce the size of the features, so in a second step the image would be dilated. Since noisy areas in the images are about the same size or even bigger than the vein, the dilation would destroy information about vein aperture. Therefore the noise had to be removed manually. After removing the noise (Fig. 14 c) the veins still show discontinuities that would affect the measurement (Sec. 4.2). To remove the discontinuities the image was dilated 10 px and eroded 9 px using the Maximum and Minimum filter of Adobe Photoshop CS 5® (Fig. 14 d).

The discretized images fit well to the microvein's interface, as it would be interpreted

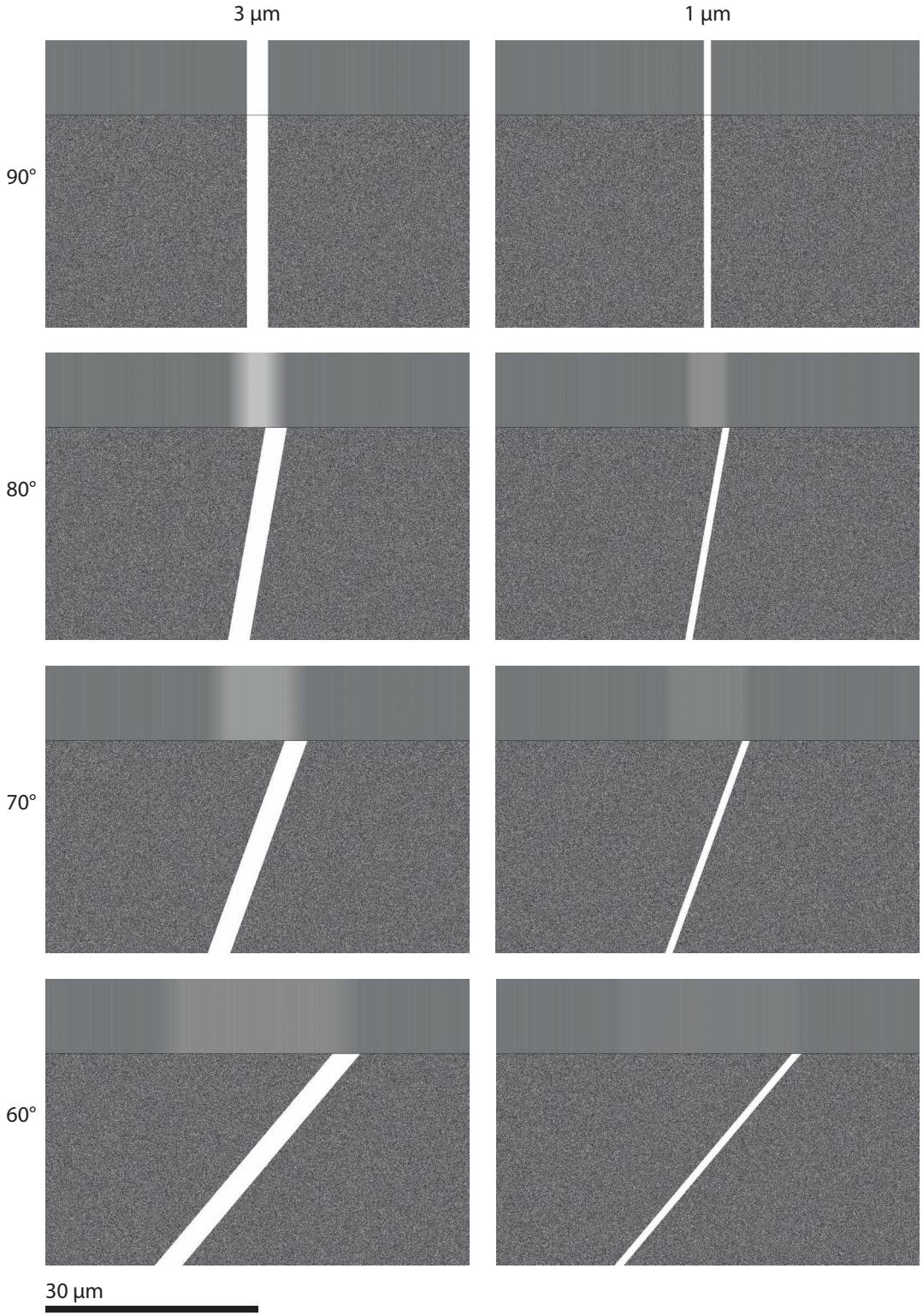


Figure 12: Simulation of vein visibility at different cutting angles. Narrow images show the top view through a microscope. Bigger images represent a cross-section through a thin section. Applied noise represents scattering of noise by micrite grains. The vein's apertures are 3 μm (left) and 1 μm (right).

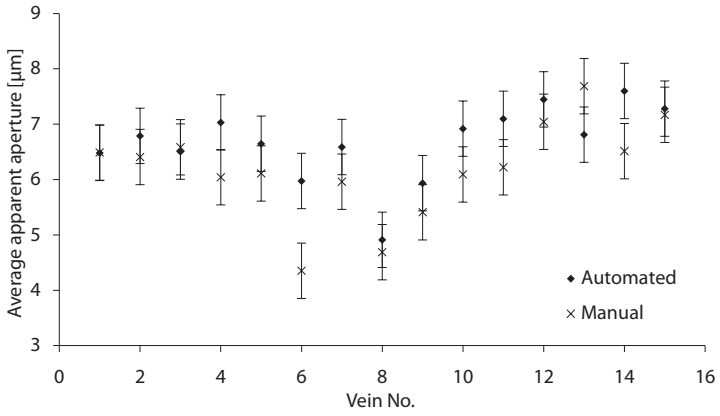


Figure 13: Comparing automated and manual measured apparent apertures of thin section C09. The error bars are ± 0,5 μm. A generally good correlation of both datasets is given with an average deviation of 0,6 μm. Only two measurements do not fit.

manually. According to the measurement accuracy derived in Section 2.2.2 a deviation of about 3 px is acceptable. A comparison between automated and manual measurement is displayed in Figure 13. The generally good correlation has an average error of 0.6 μm which is less than the resolution power of the microscope setup.

Measurements inside the discretized imagery were conducted using a simple algorithm. To avoid complicated calculations the algorithm evaluates the image column by column. Since the vein is aligned subparallel to the x-axis no major errors in aperture occur. The error caused by this assumption is also described by Figure 11. The algorithm counts the number of pixels from the bottom of the image to the first white pixel which is representative for the microvein interface. Hence vein aperture n_{vein} is calculated by subtracting the number of black pixels $n_{b,top}$ from the top and the number of black pixels $n_{b,bottom}$ from the bottom to the vein interface from the actual image height n_{height} : $n_{vein} = n_{height} - n_{b,top} - n_{b,bottom}$.

Before calculating mean aperture, areas where the vein can not be measured must be deleted, otherwise they would falsify the result. These areas are mainly caused by big grains or other veins that crosscut the observed vein (Fig. 15). In some cases (Sec. 3.4.4) the vein borders can be determined, showing that the veins continue in the grains. However, generally the veins do not show enough contrast against the cross-cutted grains to determine the host rock interface. Sometimes usage of polarized light can show some borders but in general the crystal orientation of the vein is epitaxial. The second to last step before calculating the average aperture is data smoothing which eliminates outliers. This was conducted by using the "rlowess" filter which already is implemented in MATLAB ® and calculates weighted local regression with low weight to outliers. The span of smoothing, which affects the size of included neighboring values, was set to 50 μm. Dilation and erosion of the image, which was conducted to remove discontinuities, causes steps at the host rock interface (Fig. 14 d). Smoothing was conducted to reduce errors

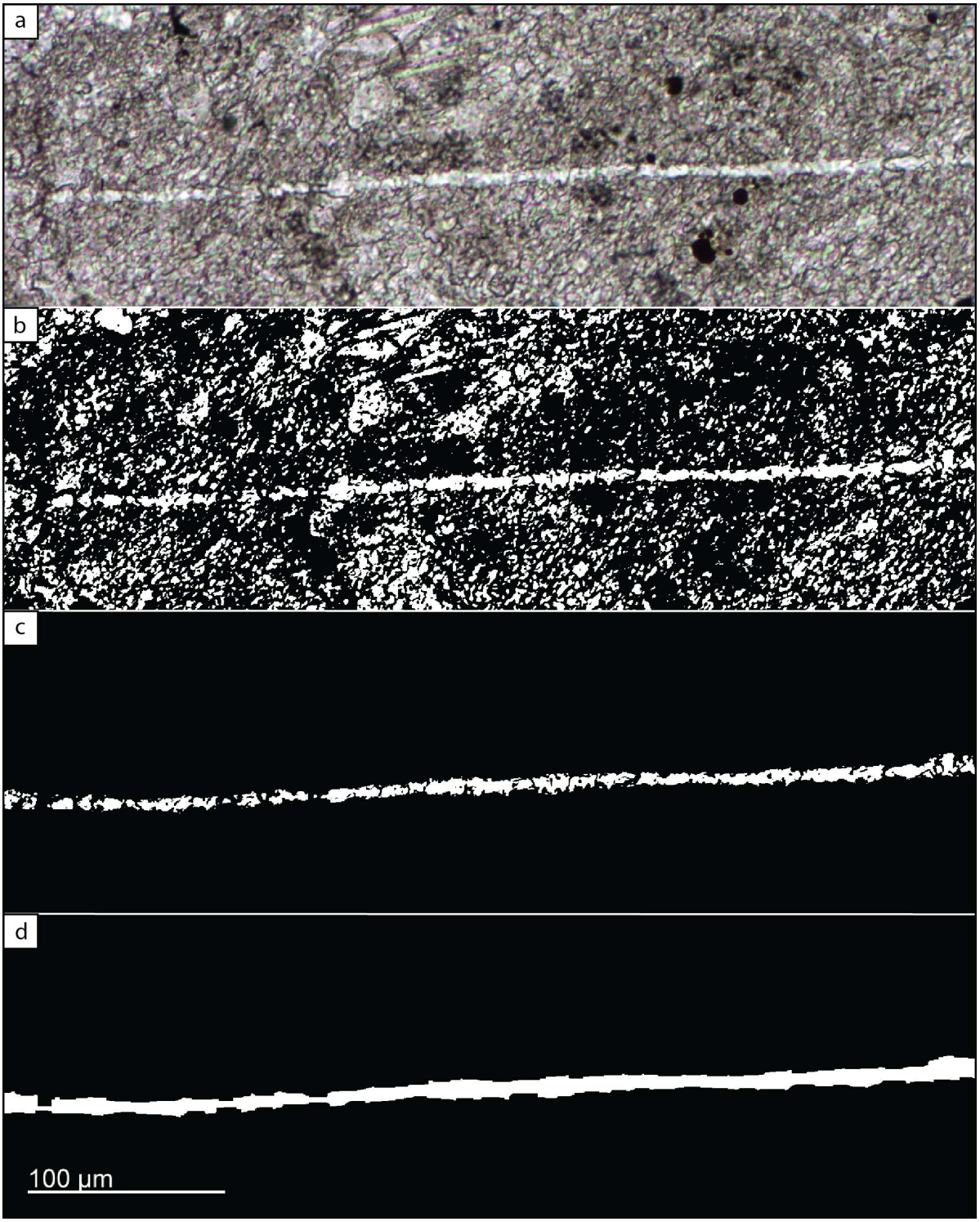


Figure 14: (a) Original Image (b) Discretized Image (c) Manually edited image to exempt the vein from the noisy background (d) Image after delation and erosion. Scalebar applies to all images.

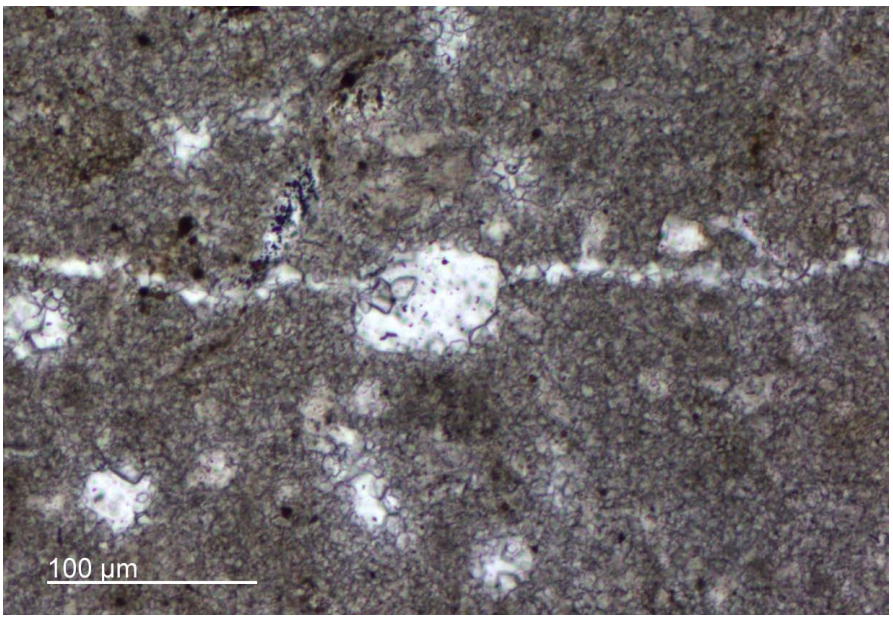


Figure 15: A microvein passes a grain in thin section C03. To avoid unrelaible measurements these areas are not taken into account.

due to these steps.

To obtain sinuosity the amount of pixels from the bottom of the image to the interface was used. In general, by observing with the naked eye, the sinuosity of microveins is very low so that this approach gives reasonable measurements if the smoothing span is chosen adequately. The smoothing span hereby defines how many neighboring values are used to calculate the average value at each point. This is equivalent using rulers of different lengths where the length defines the accuracy of the measurement or the size of the detectable features (e.g. roughness of the host rock interface). Using a span of $50\,\mu$m shows best results as presented in Figure 16. The grey graph represents the measured host rock interface trajectory. Direct measurement of sinuosity of this data would calculate the sinuosity of the host rock interface. Host rock structures also have a major impact on sinuosity smoothing with a span of $10\,\mu$m (blue graph). Using a span of $50\,\mu$m filters all signals at the scale of interface roughness out of the dataset, creating a representative graph of the veins' trajectory. The sinuosity s can be calculated by $s = l/d$ where l represents the length of the vein and d is the distance the vein puts back. To measure sinuosity at first a linear regression using χ^2 was conducted. Vein length can now be calculated using Pythagoras' theorem (Pythagoras et al., 555 B.C.) for all $n - 1$ point-doublets of the trajectory, where n represents the number of points measured. The total of all lengths equals the vein length l.

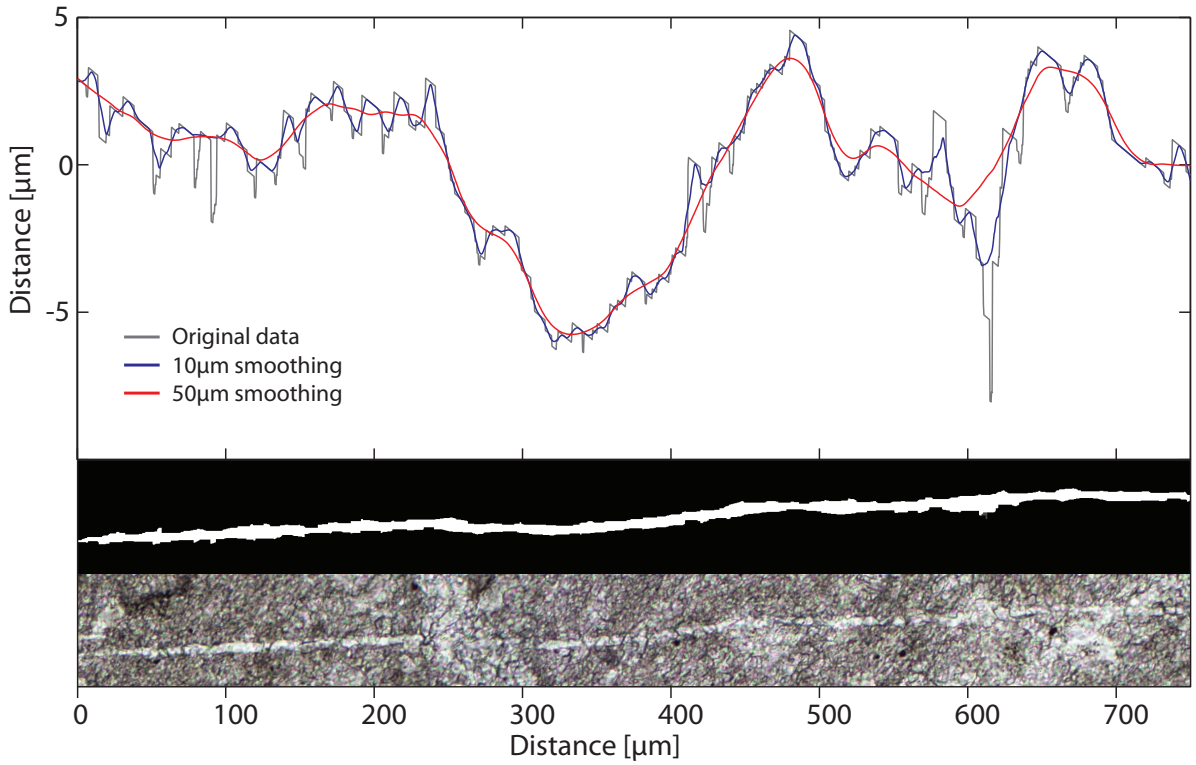


Figure 16: Graph illustrating different smoothing grades of the displayed vein (colored image). The grey graph represents the original data set which was obtained of the discretized image. Blue and red represent smoothing graphs for 10 and 50 μm smoothing grade respectively. Note the outlier at 600 μm that barely affects the smoothing.

2.3. SEM analysis

To examine the host rock interface at maximum possible detail one selective sample was investigated using an Scanning Electron Microscope (SEM). Since only one sample was analyzed using SEM this technique is only used to give an outlook for further investigations.

Microscopic analysis allowed to detect interesting spots on thin sections for SEM investigation. Thus it was possible to examine the same structures by light microscopy as well as electron microscopy. The selected sample was cut down to a size of 10x5x2 mm and then polished using an abrasive with a grainsize of 1000 meshes. Afterwards the sample was put into 10 per cent acetic acid for 15 seconds and then washed for 10 seconds using water. Afterwards it was glued onto a specimen holder. Before coating the sample with gold it was dried for 24 hours at 50 °C.

3. Observations and results

In the following subsections firstly the examined hand specimen will be described. After a short description of thin sections and SEM imagery general observations on microveins will be described. Part of this description are spatial distribution as well as orientation and microstructural analysis. At the end a proposal of microvein classification will be presented.

3.1. Hand specimens

In total twelve samples were taken for detailed investigation of microvein structure and orientation. Most of these samples were aimed to be taken away from veins. Table 1 gives an overview including coordinates of the collected samples. The samples are described in the following.

CM001, CM002

Both samples (Fig. 17 a, b) are taken at the Discotheque Pavement (Fig. 49, p. 80) that belongs to Natih-A formation. The samples show a heavy microvein density and several stylolites. Additionally CM002 has chert concretions on its surface, which is typical for the upper Natih layers.

CM003

Sample (Fig. 17 c) is taken out of an probable stylolite solution horizon at Hail al Shaz. The layers appearance (Fig. 50, p. 81) is very similar to typical Wellenkalk beds. Macroscopically no veins were visible in the field. Examining the polished samples reveals some dark traces. However typical microveins are missing.

CM004

This specimen (Fig. 17 d) is taken at Hail al Shaz (Fig. 50, p. 81) and belongs to the Upper Thithonian-Aptian beds. It clearly shows a high density of microveins with apertures up to 2 mm. The rock contains several macroscopically visible fossils.

CM006

Another sample out of a probable solution horizon from Wadi Dham (Swimming Pool Pavement, Fig. 51, p. 82). The fossil-rich dark limestone (Fig. 17 e) contains many stylolites and fractures. Furthermore the sample is very fragile and did not show any evidence for microveins at the first look. Some very small dark lines are visible in the scanned images as well as one mineralized fracture.

CM007

CM007 (Fig. 17 f) originates from Muti Conglomerate located south of Wadi Dham (Fig. 52, p. 83). It contains sub-mm to several cm large edge rounded clasts floating in a beige matrix. The clasts partially show high fossil densities. Neither in the field nor at scanned images the sample shows any evidence of microveins.

CM008

The dark grey limestone was sampled in Wadi Dham (Fig. 52, p. 83) and belongs to Muti A formation. The sample (Fig. 17 g) clearly shows a high density of microveins and stylolites. The microveins are mostly translucent and do not exceed an aperture of 1 mm. Around the subhorizontal stylolites and the E-W striking microveins some darkening of the rock is visible. These areas seem to be limited by NE-SW striking veins.

CM009

The dark blueish grey limestone origins from Lower Gorge Pavement (Fig. 53, p. 84), Muti A formation. The sample (Fig. 17 h) shows a high microvein and stylolite density. The visible microveins are mostly bedding parallel and show evidence to be younger than the stylolites. It will be later turned out that several microveins striking E-W are present.

CM010

The beige conglomerate (Fig. 18 a), sampled above Lower Gorge Pavement in Muti A beds (Fig. 54, p. 85), consists of mm to cm large rounded clasts showing a preferential orientation, dipping SE. The foliation is visible in the matrix as well as in the clasts. Microveins are frequent and generally dip NE while they have, in contrast to most other veins, a brownish color.

CM011

The sample (Fig. 18 b) was taken from Muti Shale next to the lower Gorge Pavement (Fig. 54, p. 85). The reddish brown shale is very hard and supposably has a high porosity expressing itself by spherical, 0.2 mm large pores. The shale contains several veins from sub-mm- to mm-scale which are filled either with non-calcitic or a dark grey reflecting material which could be an ore mineral. Pores adjacent to dark veins are also filled with the dark material. Therefore all visible pores might have been filled with this material that could be washed out during polishing.

Table 1: Detailed information about all collected samples.

Sample	Location Name	Easting	Northing	Formation
CM001	Discotheque Pavement	514424	2565846	Muti A
CM002	Upper Discotheque P.	514772	2566120	Muti A
CM003	Hail al Shaz	528187	2561762	Up. Tithonian-Aptian
CM004	Hail al Shaz	528489	2562398	Up. Tithonian-Aptian
CM005	Wadi Dham	507616	2569429	Natih
CM006	Wadi Dham	507616	2569429	Natih
CM007	Wadi Dham S	508789	2568911	Muti A
CM008	Wadi Dham E	507138	2568957	Muti A
CM009	Lower Gorge Pavement	513621	2573456	Muti A
CM010	Gorge Muti Conglomerate	513742	2573017	Muti A
CM011	Gorge Muti Shale	513823	2573017	Muti
CM012	Hail al Shaz Nhr Umr	523755	2562367	Nahr-Umr

CM012

The fossil rich limestone (Fig. 18 c) was sampled at Hail al Shaz, Nahr Umr Shale (Fig. 55, p. 86). It has a high microvein density with veins up to several mm aperture. Two vein types are macroscopically visible which are light beige and dark, transparent veins. Since the beige veins are truncated by dark veins they must be the older veinset.

3.2. Thin sections

Selection of thin sections depended on gathered information from the scanned images. The reasons for thin section creation as well as a short description of the rocks are explained in the following paragraph.

CM003 - C03

Since specimen CM003 did not show any usual microvein structures this thin section (Fig. 19) was prepared to investigate the appearance of microveins in possible pressure solution horizons.

The thin section was cut horizontal and shows a dark grey, fossil rich boundstone. Although no microveins are visible in small magnification there are two en echelon veins striking WNW-ESE. In contrast to the surrounding rocks no stylolites are visible in this thin section.

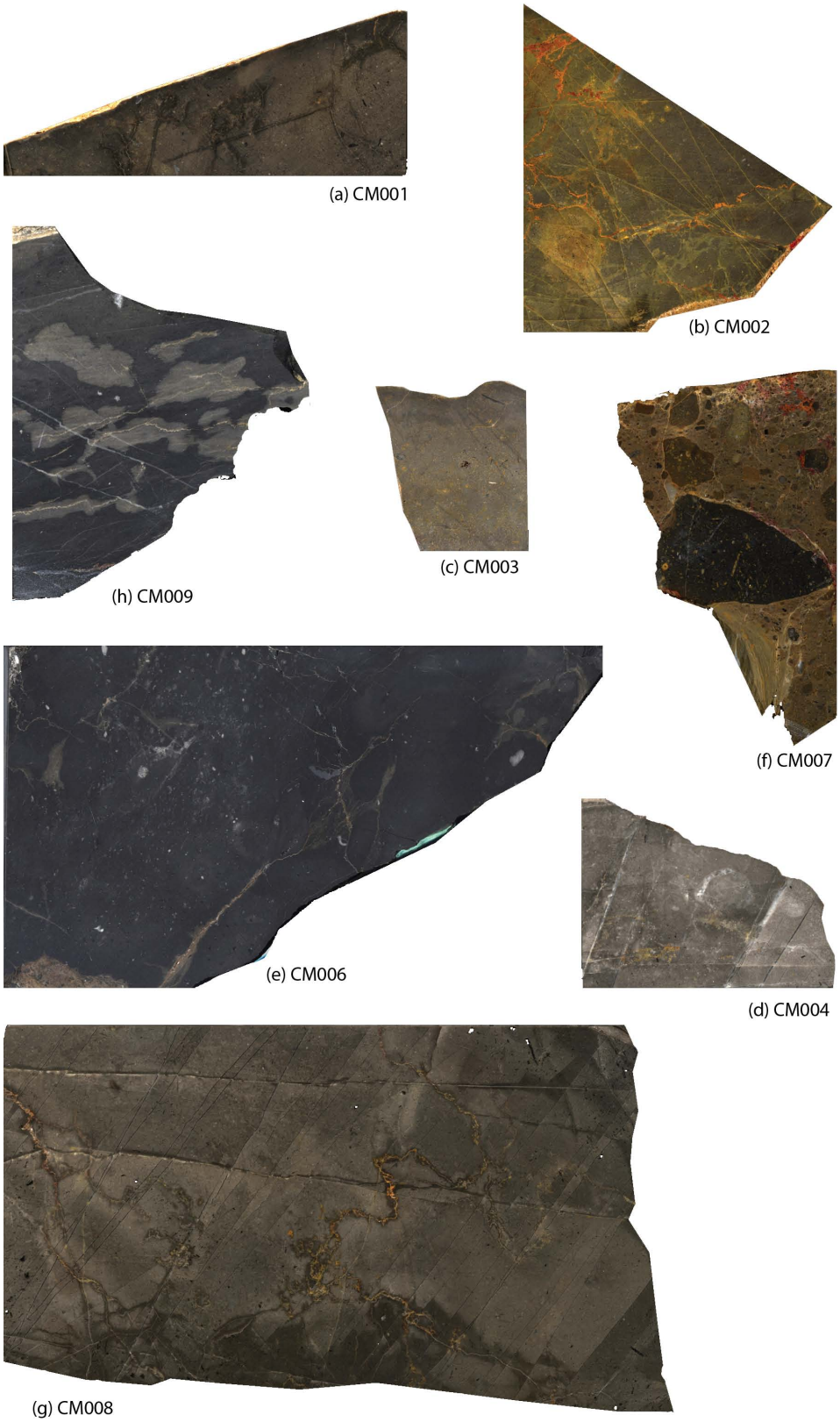


Figure 17: Horizontal cuts of samples CM001 to CM009. Note that these are no true color images as contrast was optimized due to feature recognition. Full resolution imagery is found on the DVD.

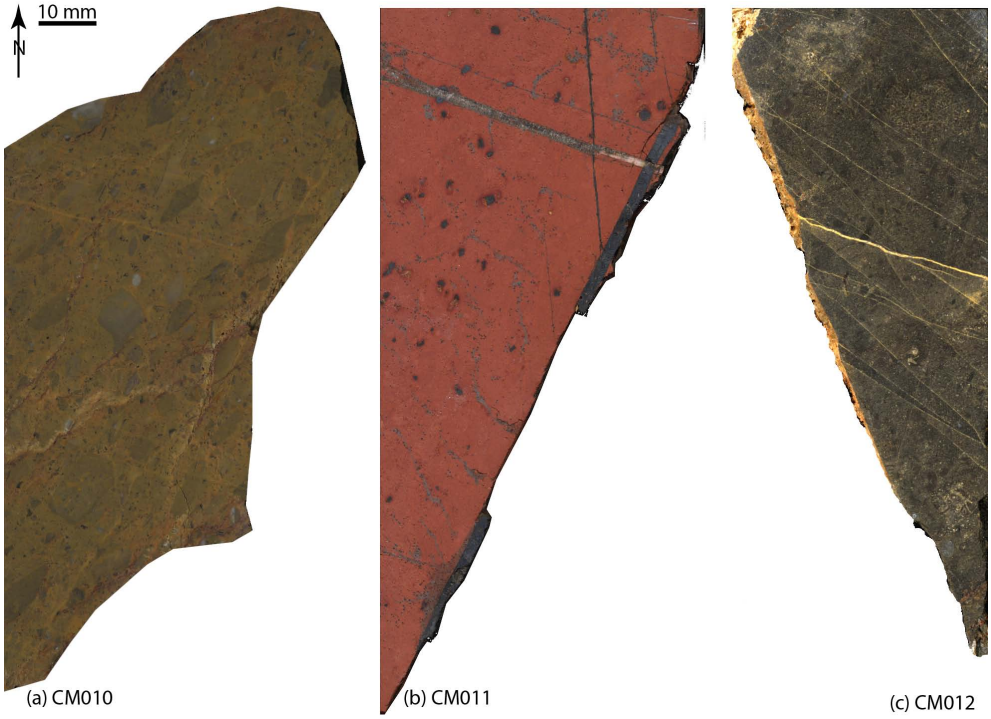


Figure 18: Horizontal cuts of samples CM010 to CM012. Note that these are no true color images as contrast was optimized due to feature recognition. Vein orientation suggests that there might be correlating vein sets which will be discussed in Section 3.4.1. Full resolution imagery is found on the DVD.

CM004 - C04.1, C04.2

Rock sample CM004 originated from Hail al Shaz and showed clearly visible microveins. Therefore two thin sections were created, one horizontal (Fig. 20) and one vertical striking W-E (Fig. 21). Both thin sections are from adjacent planes. Note that, because of thin section preparation, the geographic orientation of East and West are permuted and thus the horizontal plane in C04.1 differs from usual geographic orientation.

The fossil rich boundstone exhibits a medium high microvein density with apertures up to 1 mm. Furthermore veins in both thin sections show minor host rock inclusion bands as well as branching and floating host rock fragments. Some microvein displacing stylolites are present. The stylolites are assumed to strike subhorizontal or bedding parallel. Microveins mainly show up straight lines but also as curved lines.

CM009 - C09

This thin section (Fig. 22) was created for microvein aperture measurement and represents a horizontal cut. The boundstone shows a high vein density and contains much more small aperture microveins than reasonable big apertures. Veins mainly are straight but W-E striking veins bend slightly towards a strike of WSW-ENE in the SW-part of the thin section. Generally the abundant microveins create very low displacements when interacting with each other, assuming mode I fracturing.

CM010 - C10

Sample CM010 was collected in Muti A conglomerates and shows heavy vein density in the scanned imagery. The thin section (Fig. 23) was created to discover whether veins may occur in the clasts or also in the matrix. If this would have applied some veinsets developed before the development of this conglomerate. But the thin section shows that no microveins occur isolated in the clasts.

The rock shows a very high density in fossils and microveins with comparatively small apertures. As observed in the scanned images one veinset dominates the thin section and preferred orientation of the host rock components continues in smaller scale. Two other veinsets occur but are very rare. One of these veinsets dips to a lower degree, with about 30 ° towards North. The other veinset expresses itself by several mm long, bedding parallel veins. The thin section also shows that two vein colors appear in the dominating vein set. One set shows a bright white color while the other one shows a brownish color because of abundant inclusions. Vein intersections show that the white veins are younger than the brownish veins. Generally the veinsets indicate Mode I opening mode. Additionally stylolites occur frequently which are younger than the

surrounding veinsets. Also twin lamellae of calcite are abundant in the host rock but do not appear in any microvein.

CM012 - C12

A thin section of sample CM012 was created (Fig. 24) for microvein measurement. The fossil rich boundstone reveals a high vein density and mainly shows two dominating veinsets both dipping towards S. Furthermore Stylolithes are frequent. Like in thin section C09 there are clear and brownish microveins. Although the coloring of the brownish veins is weaker than the coloring in C09. Twin lamellae also occur in some brownish veins with apertures of about 150 μm but are truncated by younger, smaller veins.

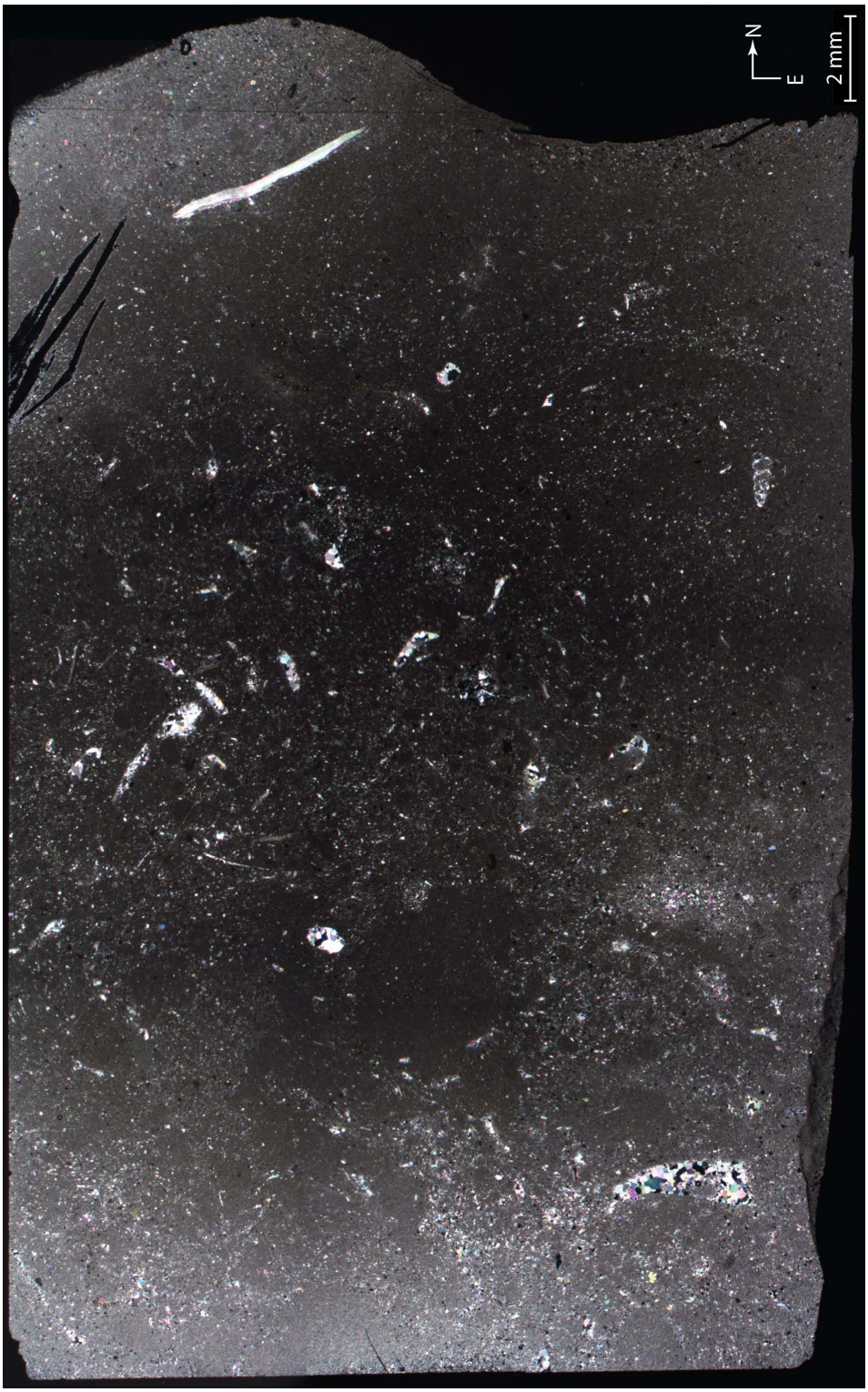


Figure 19: Stitched overview image of thin section C03, photographed with crossed polarizers.



Figure 20: Stitched overview image of thin section C04.1, photographed with crossed polarizers.

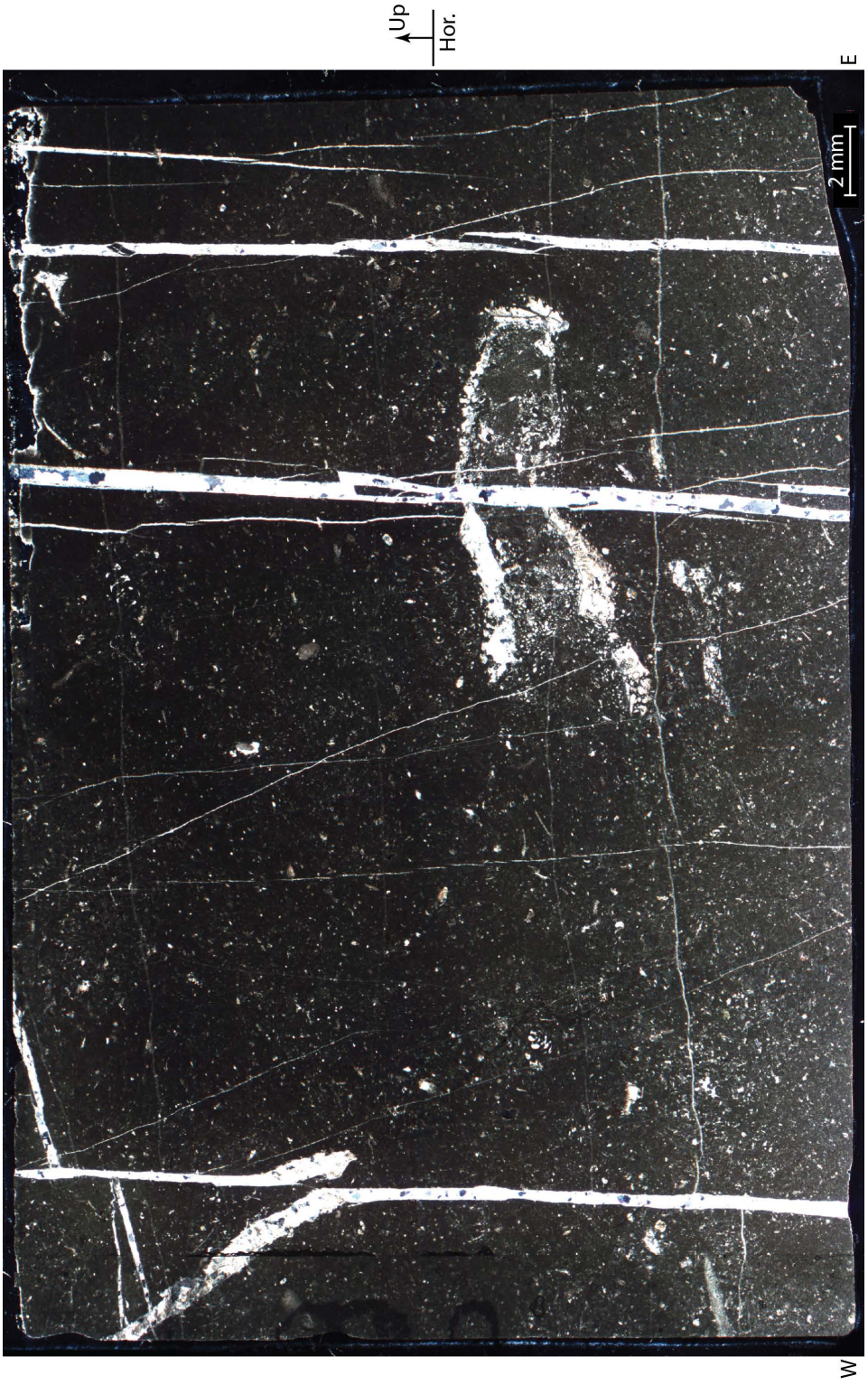


Figure 21: Stitched overview image of thin section C04.2, photographed with crossed polarizers.



Figure 22: Stitched overview image of thin section C09, photographed with crossed polarizers.



Figure 23: Stitched overview image of thin section C10, photographed with crossed polarizers.



Figure 24: Stitched overview image of thin section C12, photographed with crossed polarizers.

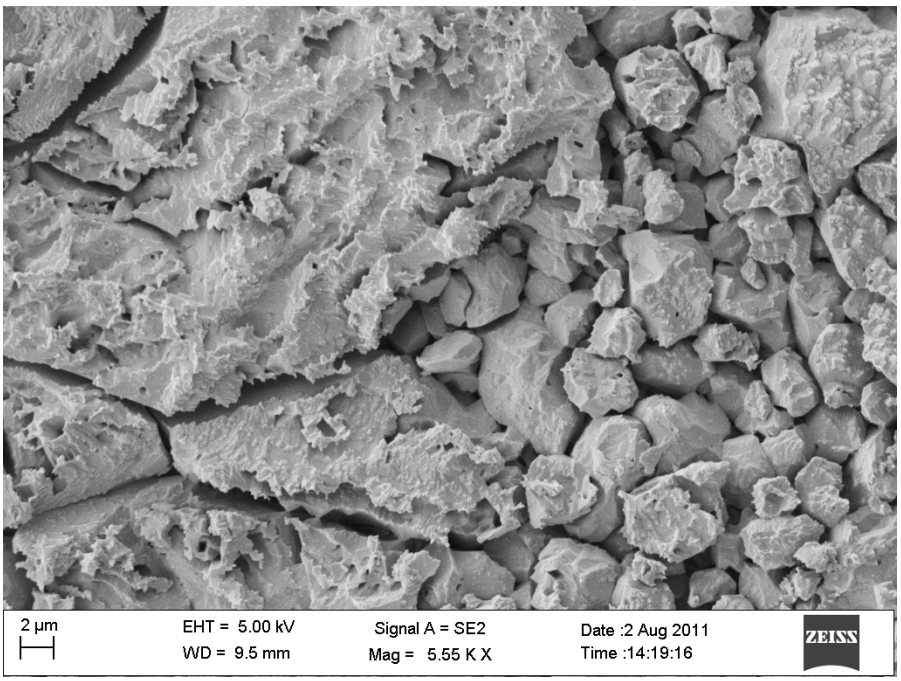


Figure 25: Detail image of host rock interface. Left: Gaps at the grain boundaries and irregular etching structures at crystals. Right: Micrite.

3.3. SEM Imagery

Investigating microveins using SEM technique offers the possibility to examine microvein structures at very high magnification. In contrast to transmitting light microscopy SEM images show the sample's surface and do not display any colors. As the SEM images in Figures 26, 27 show the contrast between host rock micrite and vein is very small making it hard to find small microveins. Generally the etching with acetic acid produced a strong morphology with deep gaps at the grain boundaries (Fig. 25). The measurement of micrite grain size shows an average grain size of 4.2 μm. Basically the micrite consists of grains without any visible porosity and grains with about 500 nm large pores.

Figure 26 shows a microvein with an aperture of roughly 35 μm. The grains show a blocky habitus without any signs of growth competition and vary between 10 and 40 μm in diameter. Additionally it can be observed that micrite grains can source as crystal growth seeds (red arrows, Fig. 26). Compared to the aperture the roughness of the interface is high, making it difficult to detect the true vein interface. Since the pictured microvein is comparably large, veins with apertures in micrite grain size will be hardly detectable using SEM imagery.

In Figure 27 a junction point is shown, imaging a microvein with an aperture of 100 μm including floating host rock fragments. At the right border some growth competition is visible while the center of the vein consists of blocky crystals with 20 to 100 μm large grains.

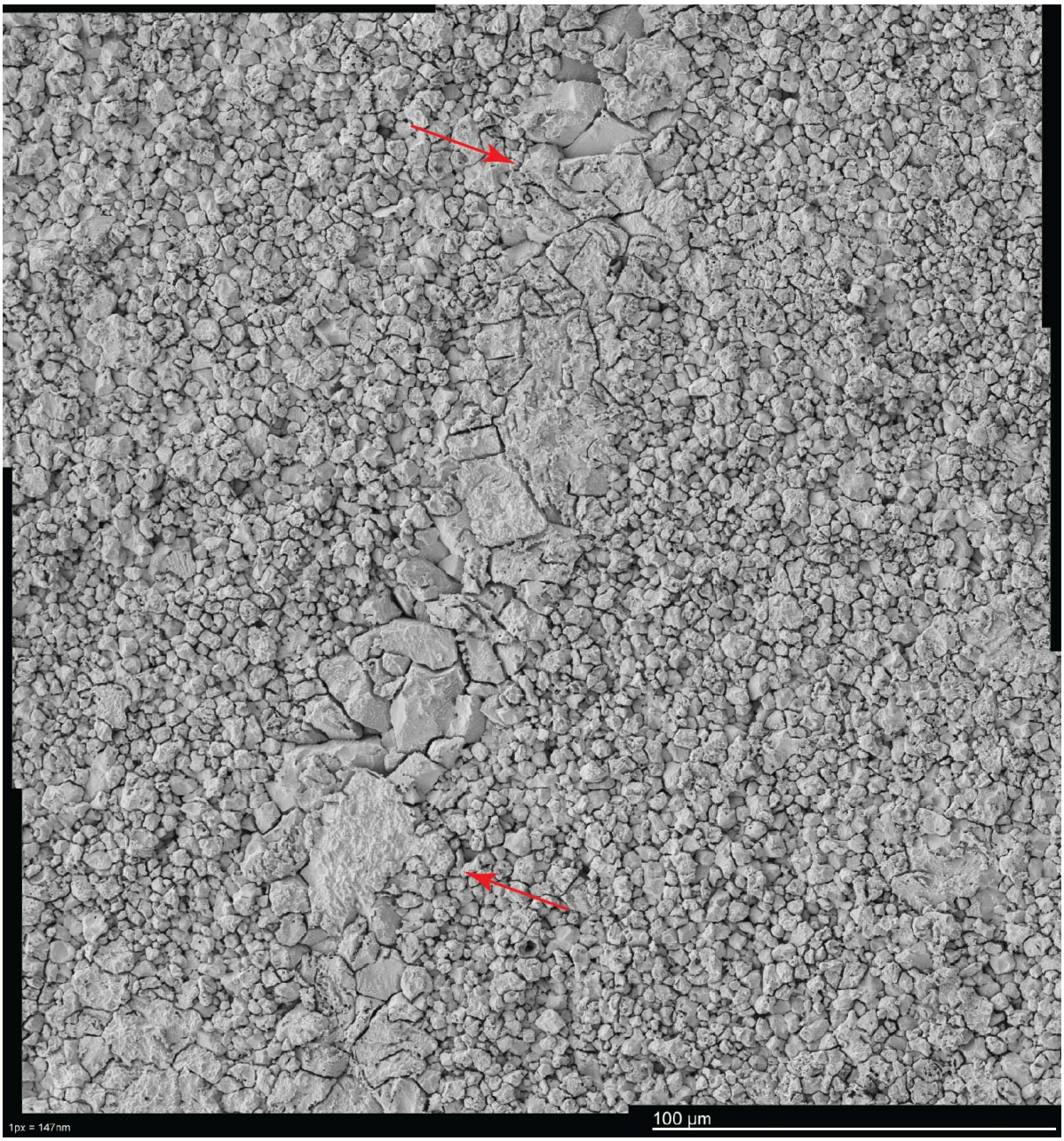


Figure 26: SEM imagery of a microvein with an aperture of approximately 35 μm showing grain growth starting at a micrite grain as seed (red arrows); (b) host rock inclusion (bottom) and growth competition texture. The red square illustrates the equivalent position on thin section C04.2.

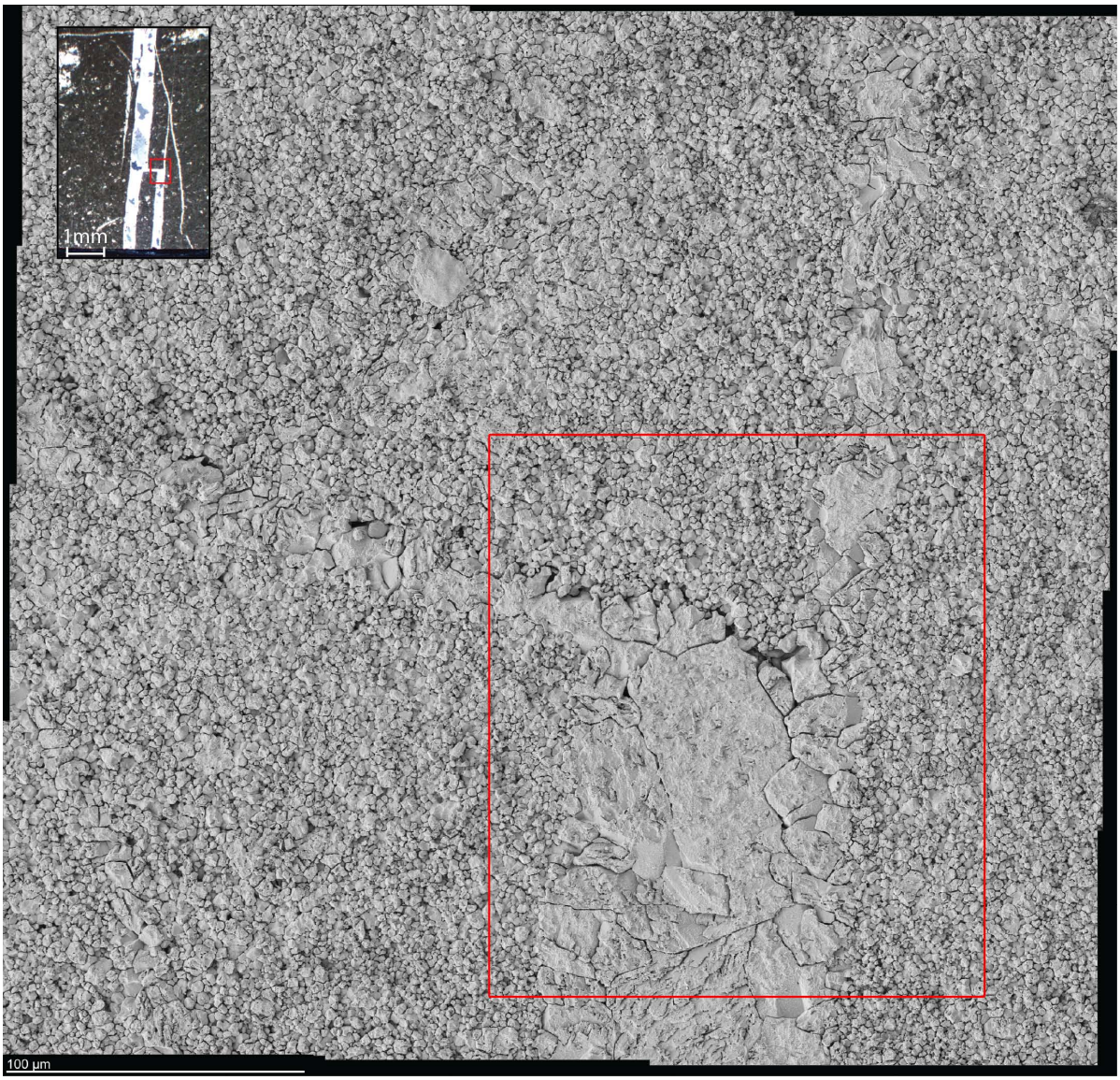


Figure 27: SEM imagery of a host rock inclusion (bottom left) and growth competition texture. The red square in the thin section-image in the top left corner illustrates the equivalent position on thin section C04.2. The red square in the SEM image shows the zoom-step for Figure 28.

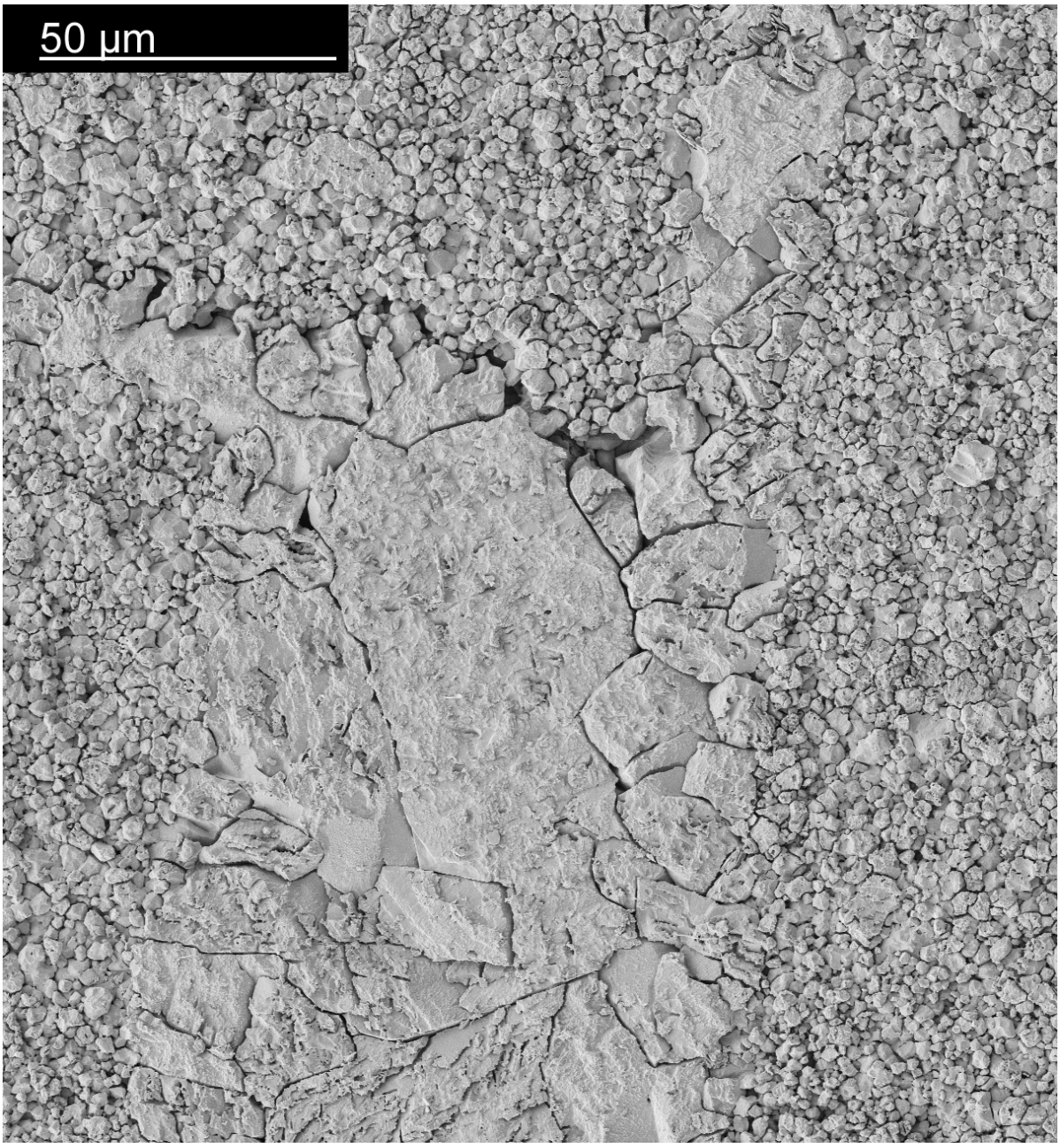


Figure 28: Growth competition habitus at the bottom right of the vein.

3.4. Vein description

In the following sections basic observations are shown which are basis of the discussion in Section 4. At first observations about spatial distribution and the orientation, derived from field observations and computer based measurements are described. The results of aperture and length measurements are shown and the frequency distribution of apertures is fitted by non-linear regression for further modeling. At the end, after description of typical morphology and special observations, microveins are divided in two basic types.

3.4.1. Spatial distribution and orientation

As observed in the field and in thin sections (Sec. 3.2) microveins are mostly dense spaced and occur in clusters, characterized by their appearance. Evidence of vein sets is also given in Figure 18 by parallel orientated vein intersection lineation.

To obtain general information about the occurrence of microveins several orientations were measured in the field. To extend these information additional orientations were measured at scanned sample surfaces as described in Section 2.1.

Figure 29 gives an overview about all measured microvein- and vein- orientations. First of all it can be seen that most microveins cut perpendicular to the bedding. In total seven general veinsets could be determined from stereogram data, recurring in several locations in the field area.

The red veinset can be found at three of the four major sites and thereby is the most dominant veinset. It strikes NE-SW and cuts almost perpendicular to the bedding. The dip only decreases at the south-east of Hail al Shaz (Fig. 29 m).

Another frequent set is the orange set striking roughly WWS-EEN. However it is not present around the Gorge Pavement (Fig. 29 d-f). The green set appears only in the Muti Shale (d), Muti Conglomerate (f) and the upper Discotheque Pavement (h).

The yellow veinset only occurs at Hail al Shaz and strikes SW-NE and is thereby locally restricted. In contrast a N-S striking veinset, marked purple, can be found in the Muti Shale (d) as well as in the Discotheque Pavement (g).

Bedding parallel veins are present at Wadi Dham (c) and Lower Gorge Pavement (e) marked blue.

In conclusion several veinsets could be determined intersecting the bedding mostly subvertically. Although the spots are 5 to 10 km apart some veinsets can be correlated. However, the amount and orientation of veinsets can vary at closely located sites, e.g. Gorge Pavement (e) and Muti Conglomerate (f) or Muti Shale (d).

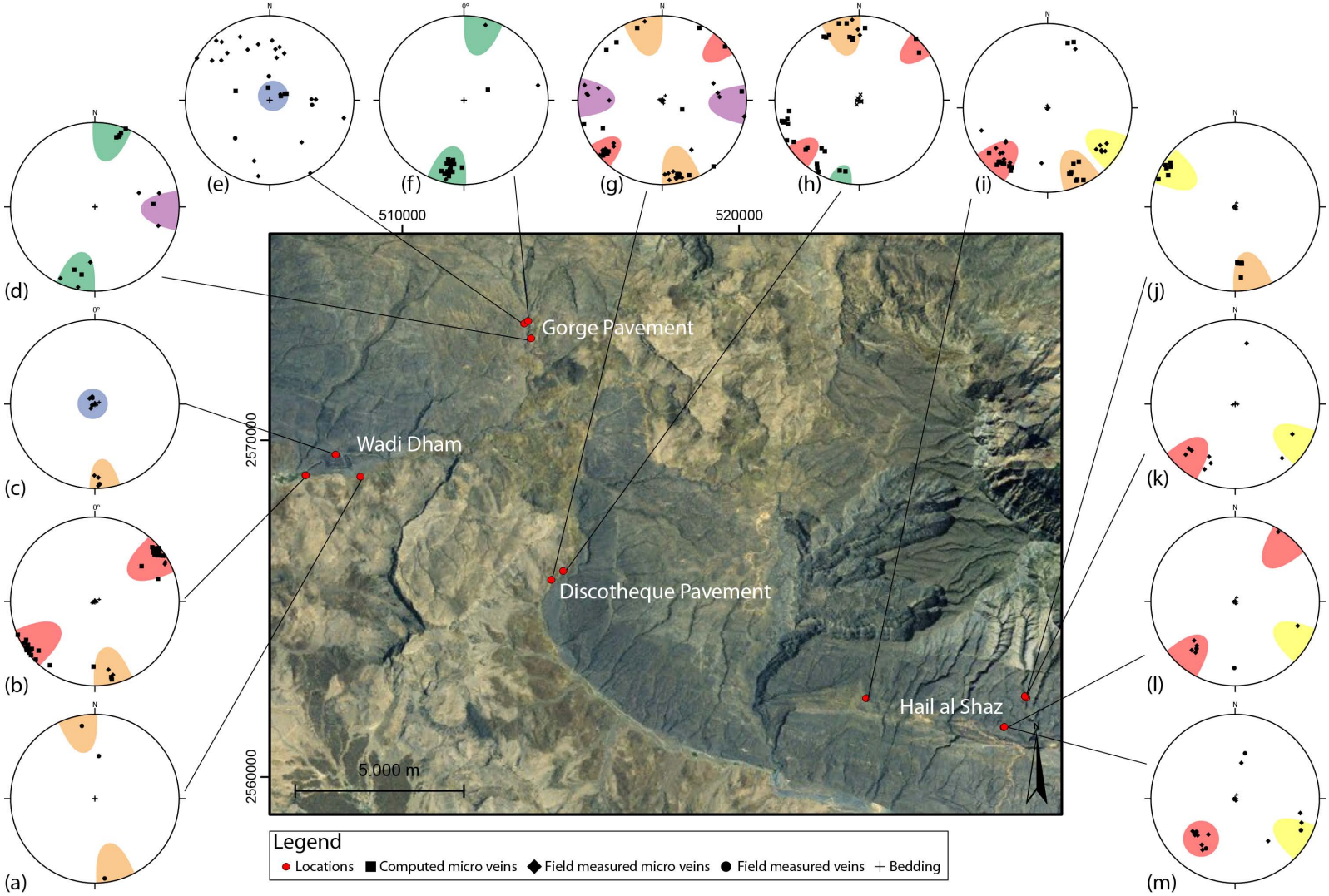


Figure 29: This illustration gives an overview about all measured microvein directions. Field measured microveins are differentially marked than computer-based measured microveins. Each stereogram plot has been rotated back to bedding for comparability. (a),(b),(c) Wadi Dham; (d),(e),(f) Gorge Pavement; (g),(h) Discotheque Pavement; (i),(j),(k),(l),(m) Hail al Shaz.

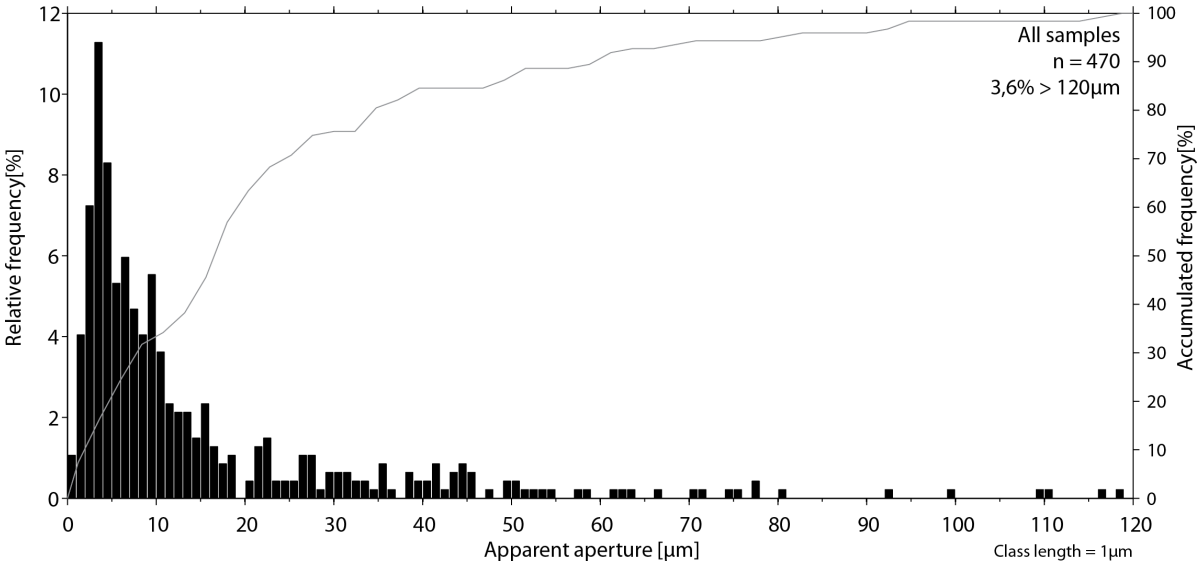


Figure 30: Apparent aperture frequency of samples CM004, CM009, CM010 and CM012. The histogram shows the distribution of all measured samples. The grey line represents the inverted cumulative frequency. Note that the histogram is cut off at 120 μm. The amount of veins situated above this apertures is noted in the top right corner of the histogram. Histograms for each sample can be found in Appendix C, Figure 56.

3.4.2. Aperture and Length

In order to obtain detailed information about the vein aperture distribution and the relation between length and aperture several measurements were taken.

Manual measuring

Measurement of aperture was conducted for two reasons. Firstly to compare computer based results with manually taken measurements and secondly to measure the distribution of apertures testing the hypothesis of a minimum opening aperture.

Figure 30 shows the frequency of apertures in thin sections C04.1, C04.2, C09, C10 and C12 as well as the inverse cumulative histogram of all measurements. In this kind of measurement four scan-lines were measured in the thin section and each vein was measured once at each line. Two lines were orientated parallel along the broad side of the thin section with a spacing of about 1 cm and two lines perpendicular to the first lines with a spacing of about 1,5 cm.

Regarding Figure 30 the aperture reaches a peak of over 11 % from 3 to 4 μm and drops correlating to a power law towards growing apertures. Between 0 and 4 μm the apparent aperture frequency rises from 1 % to the maximum of 11 %. As in the histogram displayed, 90 % of all veins are less than 60 μm in aperture.

Computer based measuring

Automated measurement was conducted in order to gain detailed information about two extending en echelon vein sets from samples CM003 and CM009. Therefore the length of each vein was determined as well as the apparent aperture (Sec. 2.2.2) alongside every point on the vein.

Figure 31 shows an example measurement of an approximately 750 μm long vein from sample CM009 (Thin section C09). The colored image at the bottom shows a true color image of the examined microvein taken without polarizers. The red and grey graphs show the apparent aperture measurements along the vein which is based on the binary, discretized image. Furthermore the grey graph shows the actual apparent aperture in each point while the red line shows the smoothed apparent aperture. The actual apparent aperture shows high peak values as well as several steps that arouse by erosion of the image during data processing. Figure 31 shows a clear vein reducing its aperture towards the vein tip. About 100 μm apart of the vein tip the final aperture of 6 to 7 μm is reached. This structural attribute can not be observed in most other microveins which generally show abruptly ending vein tips. Regarding the characteristics of smoothed apparent aperture graph in Figure 31 a fluctuation of aperture starts at 100 μm distance until 700 μm. The fluctuation shows changes in amplitudes from 1 to 4 μm which will be discussed in Section 4.2.

Amongst detailed aperture distribution for each vein the relation between aperture and length of many veins can be studied as well. Therefore Figure 32 shows a plot of apparent aperture versus length of two en echelon microveins in samples CM003 and CM009. Both veins did not show any microstructure that could be attributed to multiple opening events (Def. see Sec. 4.1). Microvein aperture does not exceed a maximum of 9 μm and a minimum of 5 μm while a general deviation of vein apertures from one to the other sample is observable. Average apertures of the microveins are 6.7 μm for CM009 and 7.7 μm for CM003. A correlation between aperture and length can not be observed whereas another feature is conspicuous. In both samples the scattering of apparent aperture declines towards growing length. But this could be an artifact caused by the low amount of measured veins resulting in a lack of veins with big apertures.

Power-law correlation

Visualizing the measured values using a cumulative distribution function after Pickering et al. (1995) is displayed in Figure 33. The regression curve follows a function

$$N = a\ u^D \tag{5}$$

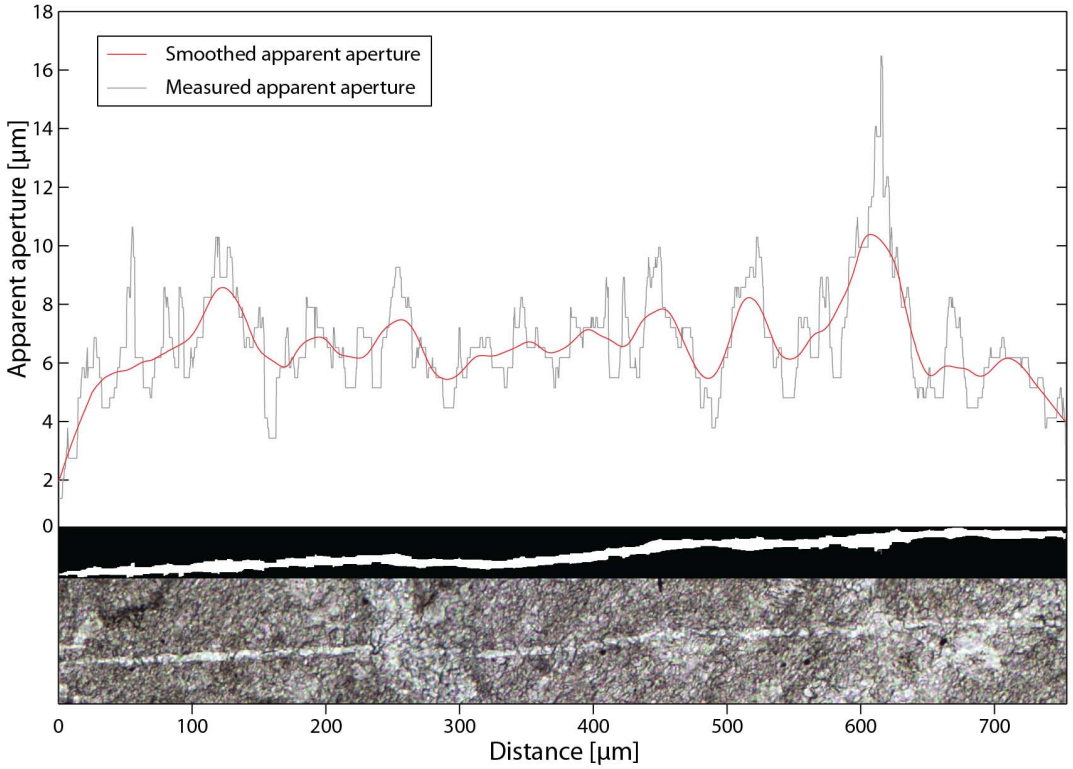


Figure 31: Bottom: The lower image shows a true color, non polarized microscopic image while the upper image represents the discretized vein. Top: Automated apparent aperture measurement of a vein from thin section C09. The grey graph shows the measured apparent aperture for each line while the red graph represents the smoothed apparent aperture. For smoothing all values in a 50 μm neighboring were considered.

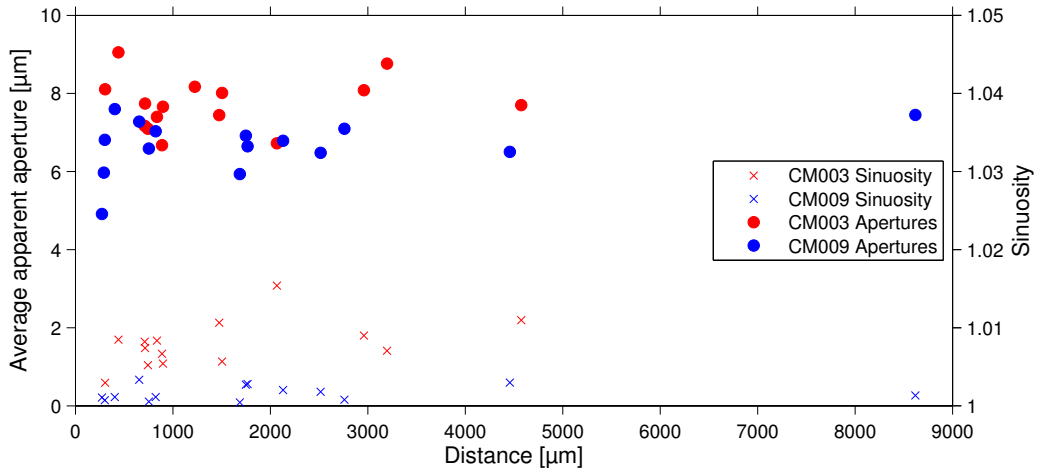


Figure 32: Circles: Average aperture distribution of two en echelon microveins in the samples CM003 and CM009, each consisting of 15 separate microveins. Crosses: Sinuosity, defined as length divided by distance, of the analyzed veins.

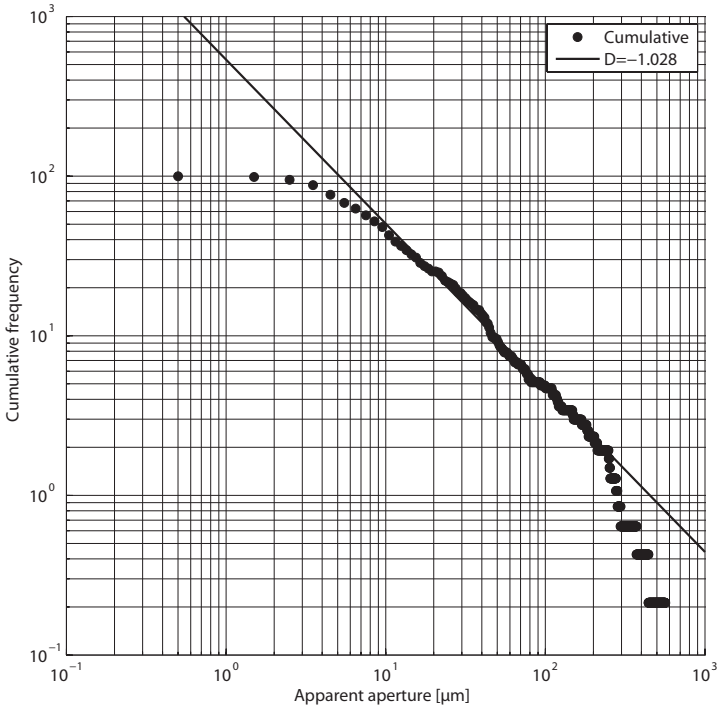


Figure 33: Log-log plot of cumulative distribution function.

where a is a constant, u is the cumulative number of values $\geq u$ and D represents the fractal dimension. The curve shows a left-hand truncation fall-off at about 10 μm. Data situated within the fall-off are note reliable and should therefore not be used (Pickering et al., 1995). A new interpretation approach of the LHT fall-off, especially for this population, will be presented in Section 4.3. Decline of frequency at apertures of 200 μm is called censoring (Pickering et al., 1995). This is due to thin section size and sampling spot location. Because samples were taken at spots distant of large veins, data at large vein apertures is biased. Hence the regression curve was calculated for apertures from 10 to 200 μm. The calculated fractal dimension is $D = -1.028$.

Another nonlinear regression was conducted to gather information for aperture simulation (Sec. 4.3) using the histogram data. Therefore at first all classes of the histogram (Fig. 30) where no vein could be measured were removed from the dataset. Otherwise no regression could be conducted because $log\,(0)$ is not defined. Additionally all values below the maximum frequency were removed since in the model this distribution is not assumed to follow a power law.

The assumed distribution which was used for non-linear regression is described by the equation

$$y = a\,x^b \tag{6}$$

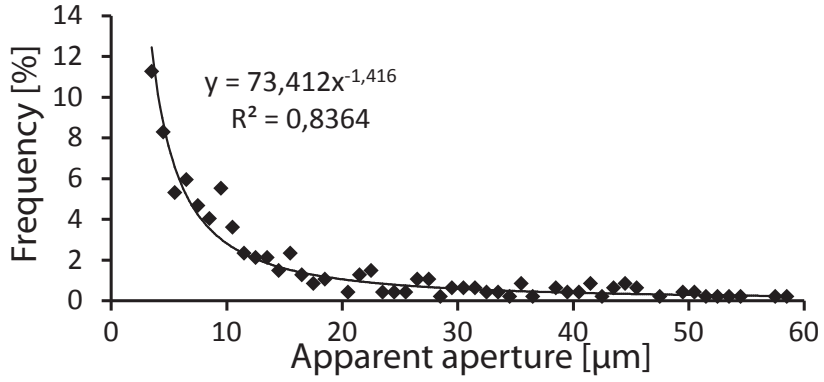


Figure 34: Nonlinear regression assuming distribution by Equation 6.

with frequency y and aperture x. Because 90 % of all measured microveins have apparent apertures lower than 60 μm only apertures up to 60 μm were taken into account for non-liner regression. The regression function is shown in Figure 34 with $a = 73.412$ and $b = -1.416$. The regression coefficient R^2 is calculated with 0.8364 and shows a good correlation to the given equation.

3.4.3. Microfabric

Microfabric of microveins gives, amongst others, indications about number of opening events, tectonic exposure or fracture behavior. Therefore several investigations were conducted on microscopic and submicroscopic scale which will be presented in the following paragraphs. Nomenclature for inter-granular, intra-granular and grain-boundary fracturing refers to Atkinson (1989).

Morphology

All microveins in the investigated thin sections show a blocky morphology (nomenclature after Bons (2000)). However, four types of crystal microstructures were determined (Figure 35):

1. Microveins with apertures up to about 10 μm generally show a blocky crystal habitus (Fig. 35 a). This structure is interpreted to arise from extreme growth competition or few nucleation seeds (Holland and Urai, 2010) and was also observed in one veinset with an average aperture of 70 μm (Thin section C04.1).

2. Microveins with apertures around 10 μm also show a blocky texture with syntaxial idiomorphic grains (Fig. 35 b) which arose of non-extreme growth competition (Holland and Urai, 2010). Microveins in an order of size about 10 μm rarely show this kind of microstructure.

3. Similar to this structure, a combination of (1) and (2) leads to idiomorphic habitus at the host rock interface and a blocky structure inside the vein (Fig. 35 c).

4. This structure was only found in large microveins with apertures of several hundred μm showing a generally blocky crystal growth (Fig. 35 d). These blocky crystals include small fragments of host rock inclusion bands with average diameters in μm-scale. These veins also show floating host rock fragments up to several mm in diameter.

Another observed structure is shown in Figure 26. The SEM-imagery shows a blocky microvein surrounded by micrite. One large grain in the vein has a bottleneck formed bridge connecting it with a grain in the matrix.

Observing microveins in ultra thin sections shows the rough interface of microveins, as pictured in Figure 37. Observing microveins in ultra thin sections with apertures of about 3 μm reveals a rough host rock interface as pictured in Figure 37. The thin section of Figure 37 origins from Discotheque-Pavement outcrop and gives a high detailed insight into a microveins' structure, since thickness effects are eliminated. Expansion of some micrite grains into the vein (red arrow) indicate grain-boundary fracturing.

Host rock related structures

As in Section 3.3 shown the micrite grain size is in the same order of size as microvein aperture. Therefore the interface of all microveins is reasonably rough compared to their aperture (to be discussed in Section 4.2). Furthermore in the observed samples several host rock inclusions in form of inclusion bands or floating blocks are present.

Figure 38 pictures a microvein with extreme growth competition structure in the center and syntaxial idiomorphic crystals at the host rock interface. Branching occurs as well as floating host rock fragments. Particularly eye-catching is the branch on top of the vein as it shows several host rock bridges This vein is interpreted to be the result of at least four opening events.

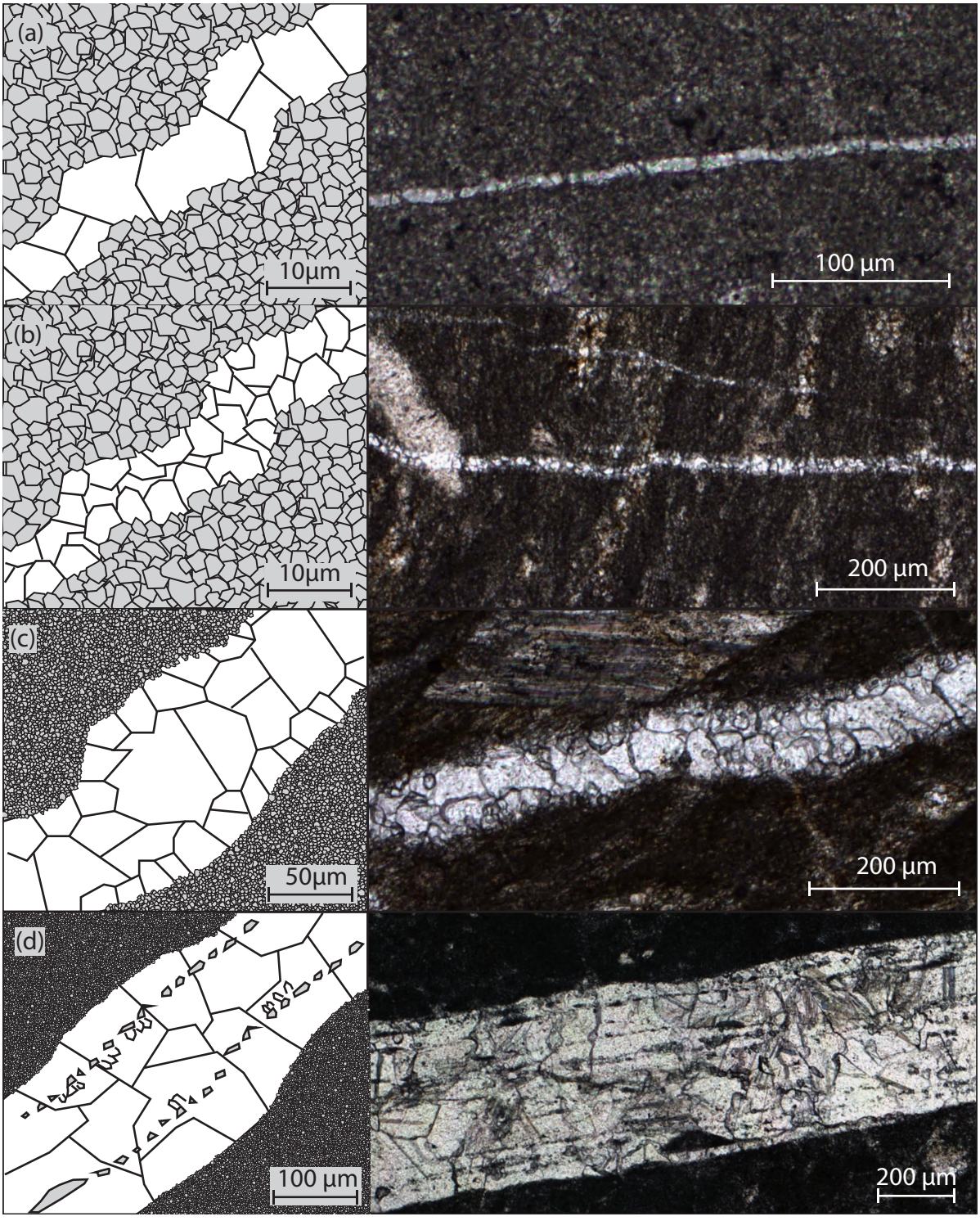


Figure 35: General observed microstructures in microveins. On the right side: example microveins, photographed in non-polarized light. (a) Extreme growth competition, (b) growth competition, (c) growth competition habitus at the interface and blocky crystals in the center, (d) blocky habitus but crystals include host rock inclusion bands. Sometimes idiomorphic crystals grow towards the center of the vein. Note the different scales.

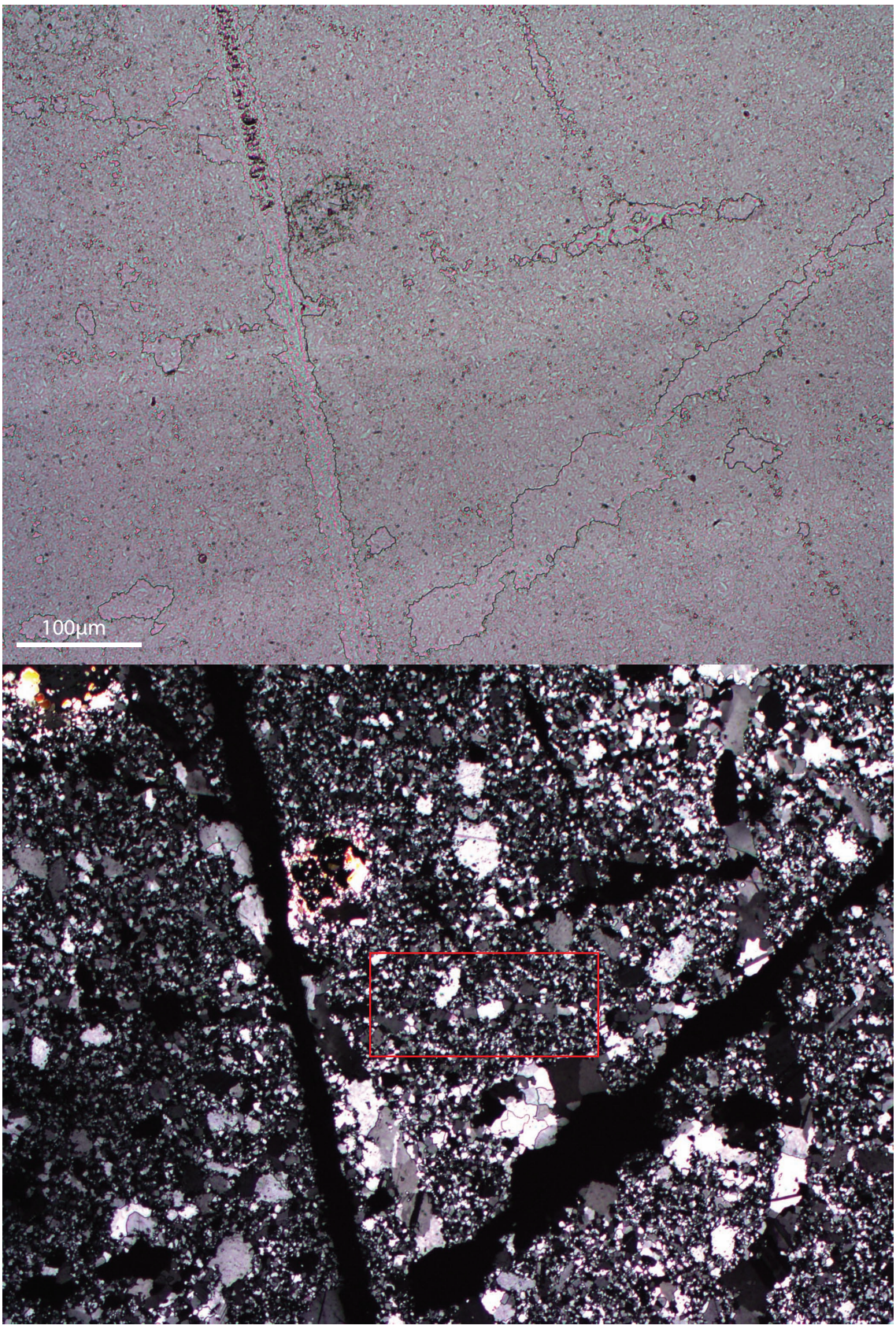


Figure 36: Top: Non-polarized image of a super thin thinsection. Only few structures are visible. Bottom: Cross-polarized image at the same position as above. The red square marks the position of Figure 37. The scale bar applies to both images.

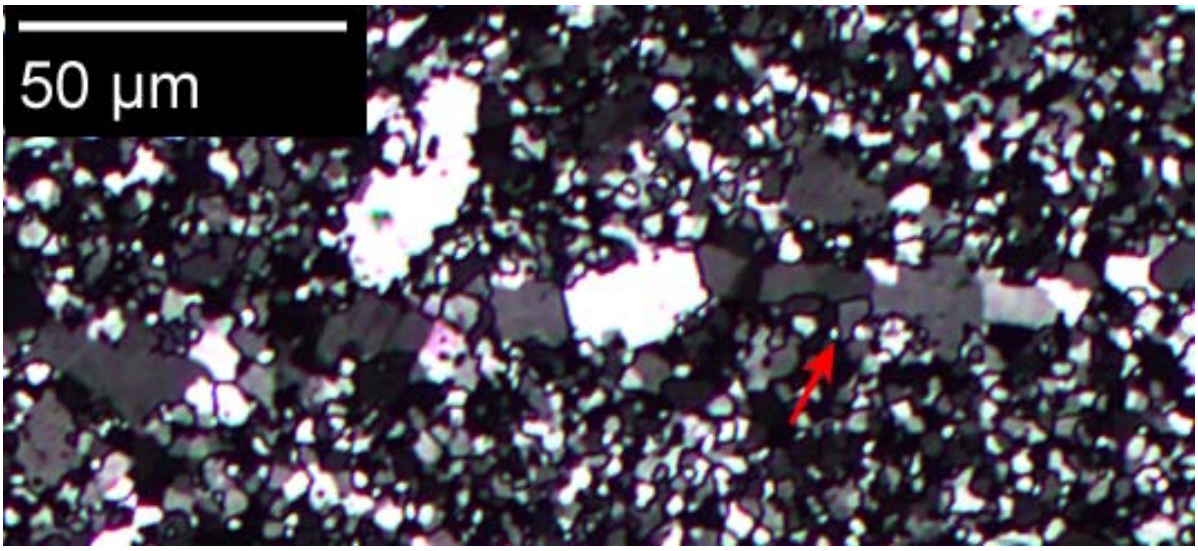


Figure 37: Photograph of a thin section with a thickness of roughly 3 μm. A microvein strikes left to right showing a blocky texture with evidence of extreme growth competition.



Figure 38: Non-polarized image of a vein in thin section C04.2 showing branching.

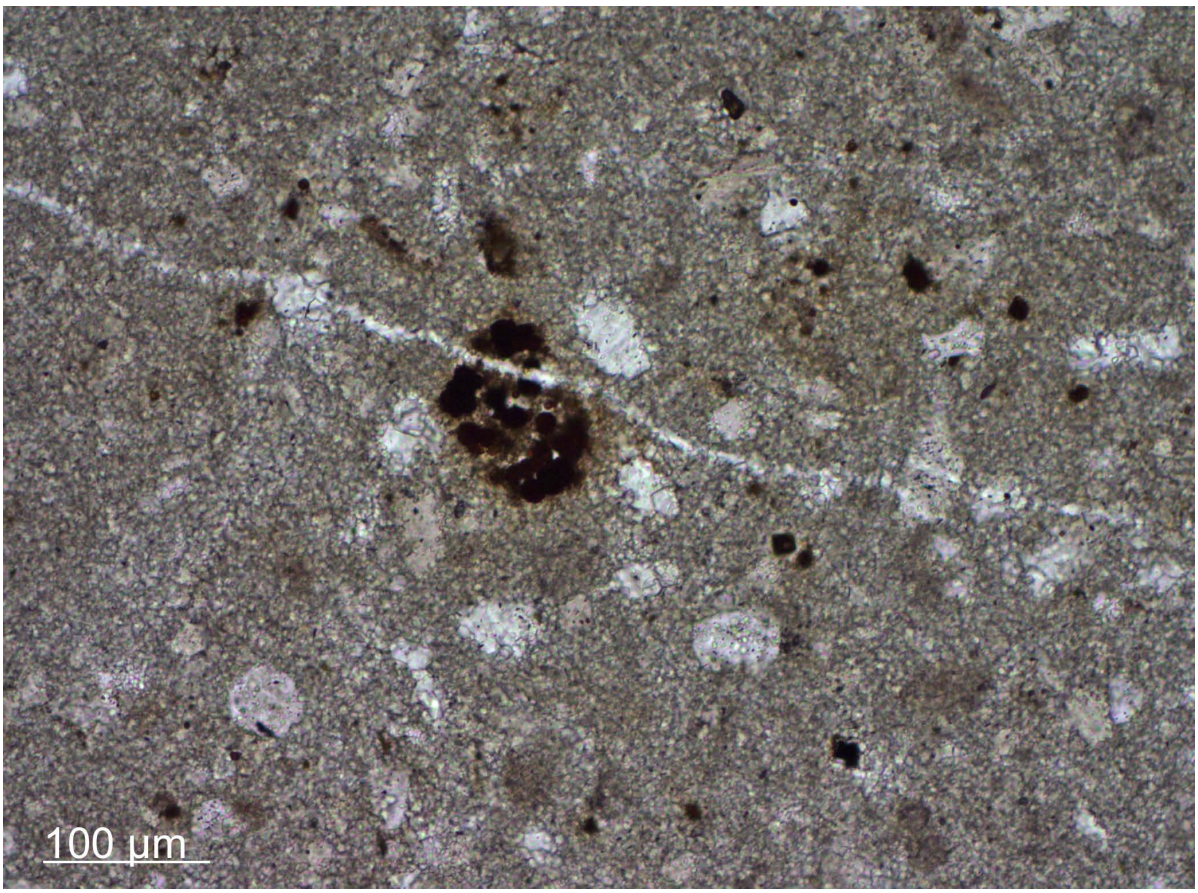


Figure 39: Microvein interacts with a circular structure in thin section C03 indicating Mode I fracturing. Image was taken without polarization.

3.4.4. Interaction

Observed microveins frequently show interaction with grains or fossils and other microveins. At first interactions with fossils are described while later the vein-to-vein interactions will be qualified.

Figure 39 and 57 (Page 88) show two veins interacting with microfossils. Figure 39 shows an approximately 7 μm thick microvein in thin section C03 crosscutting a dark structure. A circular structure, marked by the white arrow, was crosscut by the vein and displaced perpendicular to the vein's propagation direction. The well fitting semicircles indicate an intra-granular fracturing during propagation as well as Mode I fracturing. Figure 57 shows a fossil cut by a crack-seal vein in thin section C04.1. Although a minor dislocation at the bottom border of the fossil occurs, it shows up that this crack-seal vein opened favored by Mode I fracturing. However, the misfit at the bottom side can be explained either by oblique cutting or by mixed mode opening.

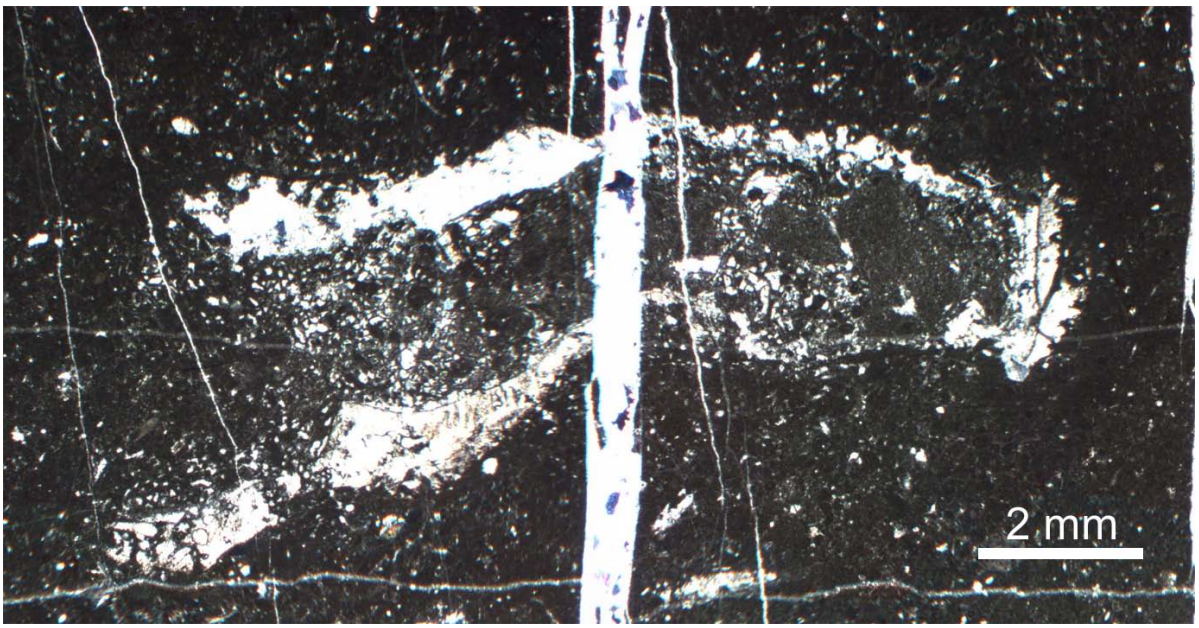


Figure 40: Microvein, created by multiple events, interacts with a fossil (thin section C04) indicating Mode I fracturing.

Another vein in thin section C04.1, belonging to the same veinset as the microvein in Figure 40 b is pictured in Figure 57. The stitched, non-polarized image shows a big vein interacting with two veins and a fossil. The vein shows up three criteria for shear opening modes. The vein seems to end at the fossil but is connected via a very thin microvein to the upper vein part. The big microvein shows a growth-competition morphology and truncates the fossil at a low angle while the connecting microvein tangentially continues the intersection line. The vein intersects with two other microveins in the lower and upper part of the image. The arrows on the right side of the image represent the in-plane moving directions of the right block. The displacements show an offset of 1.4 to 1.6 mm. This setup suggests a sinistral shear movement opening the vein. However this vein did not open as Mode I fracture and thus shows that fractures can open in different modes even though they belong to the same veinset.

Figure 41 shows two examples of veins intersecting with grains consisting of one calcite crystal. The sinuosity of the microvein is reduced in the calcite grain and the interface between grain and vein is very sharp and straight. On the other hand the right hand side shows a brownish vein intersecting a calcite with twin lamellas. In this case the vein border is not as sharp as in the first case but the vein interface seems to be smoother as well. Note that the vein also crosscuts the twin lamellae of the calcite. These two examples do not represent the general behavior of veins since, introduced in Section

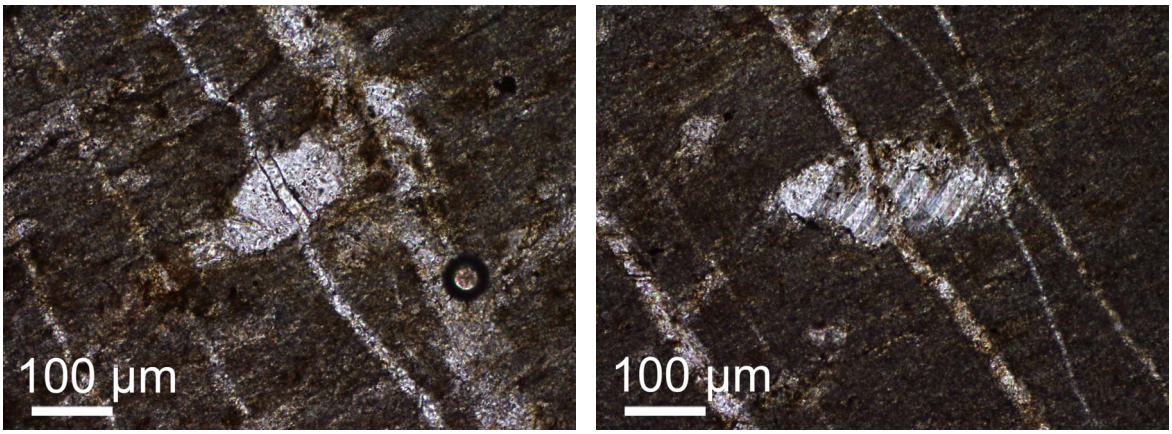


Figure 41: Two veins in thin section C10 interacting with single grains.

2.2.2 (Fig. 15), sometimes the veins crystal morphology is altered in the grains.

Most microveins with lengths smaller than thin section dimensions show a starting and an ending point. Also mostly microveins of low apertures around 10 μm seem to be one extending vein in low magnifications but reveal to be en echelon veinsets at higher magnifications. Two veins in thin section C04.1 show termination at intersection points with the same crack-seal vein which is evidence for an open fracture.

Vein to vein interaction revealed to be complex since deflection and shear movement could not be distinguished well. A vein showing offset at intersection with another vein is therefore not compellingly older than the other vein. Also age relationships in most of the thin sections could only be derived from structural differences such as vein color (see thin sections C10 and C12, Page 28).

3.4.5. Microvein types

In total microveins generally show an uniform appearance. Though basically two types of veins occurred in the thin sections. The classification is based on the microveins color and thereby also by the origin of fluids. Thin section C10 and C12 showed brownish veins being older than the bright veins representing both types. Each type can be subdivided into four classes of morphology, described in the previous Section 3.4.3. Since interbedded calcite grains or fossils are completely enclosed by micrite, transferring the stress-field onto the grain, the propagation of the fracture continues through the grain. By this a deflection of the microvein can be possible due to crystal orientation implying strength anisotropies.

4. Discussion

In the following section the previously presented observations and results will be interpreted and discussed. At first a general interpretation of microstructure will be proposed. Then possible indicators for veins being opened and sealed by one event will be discussed followed by the interpretation of apparent aperture distribution.

4.1. One event criteria

It is important to determine criteria of vein-development to infer from the microvein's structure to the fracturing process. Thereby most reliable information can be gathered from veins aroused at one event. In the course of this investigation no structure showing reliable evidence for one-event-veins could be found. For this reason only veins of a population can be determined that do not show any of the following structures and thus are most probable to be one-event-veins:

- **Host rock inclusion bands:** As introduced by (Ramsay, 1980) host rock inclusion bands origin from multiple incremental events
- **Floating host rock pieces:** Floating host rocks are similar to anastomosing vein networks proposed by (Holland and Urai, 2010)
- **Branching:** Branching is interpreted to be a pre-stage of anastomosing vein networks at subcritical crack growth (Atkinson, 1989; Holland and Urai, 2010)

4.2. Structure

In this section development of cement micro structure is discussed and whether the structures indicate single- or multi-phase opening. Afterwards the type of fracture propagation will be discussed.

Cement micro structure

Four general types of cement micro structures could be determined (Fig. 35, p. 47). Microstructures with grains much larger than the matrix grain size (Fig. 35 a) develop either by "extreme growth competition or the sparse distribution of nucleation sites along the fractures" (Holland and Urai, 2010). The structure could be observed in veins with apertures up to 70 μm which also showed structures related to multi-phase opening.

Slow growth competition leads, according to Holland and Urai (2010), to a microstructure as pictured in Fig. 35 b. Since the fractures were open for a certain time they could be easily reactivated.

Micro structures similar to Fig. 35 c are interpreted to form by a combination of slow and extreme growth competition. The change of crystal growth rate might be caused by a change in fluid composition.

Basically all observed microstructures, except inclusion bands, can develop from one or multiple events. Therefore, a detection of single- or multi-phase opening of veins can not be based on cement micro structure.

Fracture propagation

Structural analysis revealed that the microvein host rock interface is rough compared to the vein's aperture. This was deduced by SEM analysis (Fig. 26, 27) as well as analysis of very thin thin sections (Fig. 37).

Regarding SEM-imagery (Sec. 3.3) and thin section analysis (Sec. 3.4.3, Fig. 37) microveins propagate by grain boundary fracturing. However, fossils and grains much bigger than micrite are excepted from this rule as shown in Figures 39 and 39.

Grain boundary fracturing is supported by the average apparent aperture plot in Figure 31. As declared in Section 3.4.2 the average apparent aperture shows a fluctuation with amplitudes of 1 to 4 μm. This fluctuation, with amplitude variation similar to micritic grain size (Sec. 3.3), is interpreted to be an artifact of the rough interface.

Assuming grain boundary fracturing also explains some effects caused by interaction of thin microveins and thick thin sections. Figure 42 shows a microvein photograph of thin section C9. The transmissibility of the microvein is irregular and can be explained by a simple model pictured in Figure 43. The illustration on the left shows of a vein developed from grain boundary fracturing. The micrite grains disperse the transmitting light resulting in a contrast reduction, observed in Figure 42. Applying the model onto SEM imagery (Fig. 43 b) also shows the rough interface of veins which results in an irregular illumination.

Another observation to be interpreted as effect of grain boundary fracturing is given by microvein discontinuities. As in Section 2.2.3 mentioned some veins show discontinuities in data processing. These might as well caused by micrite grains extending into the veins' space (42 red arrow).

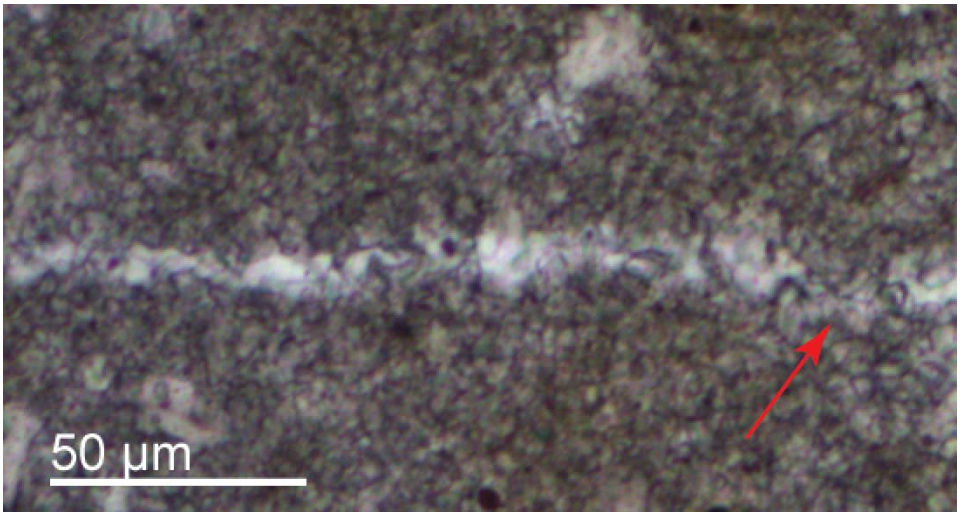
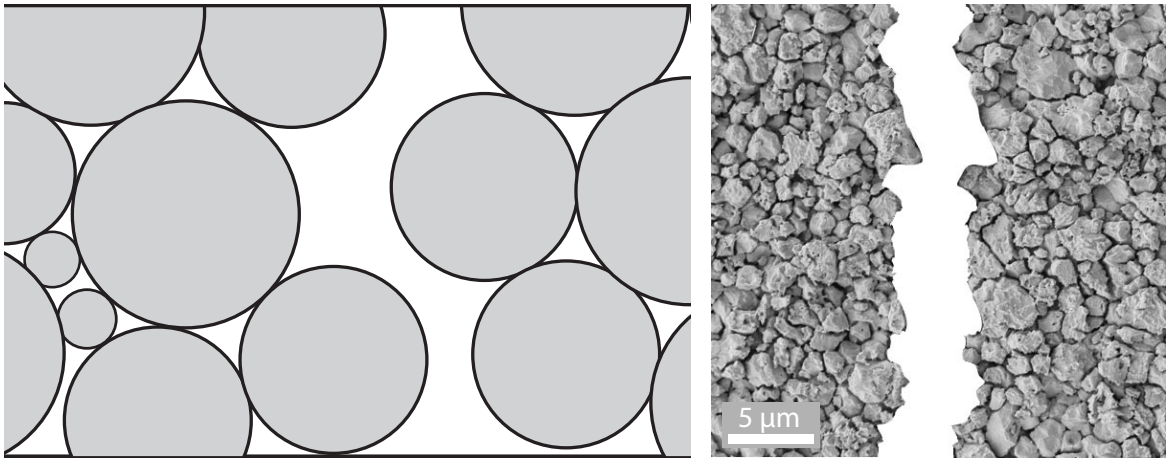


Figure 42: Photograph of a microvein with irregular illumination. The red arrow indicates grains which extend into the veins' space.



(a) (b)

Figure 43: (a) Simplified model for explanation of gradient illumination. Grey circles represent micritic matrix, white represents vein-filling. The high roughness of the interface, deduced by intra-granular fracturing, reduces contrast of transmitted light; (b) model applied onto SEM imagery. The hostrock was split along the matrix grain boundary simulating grain-boundary-fracturing.

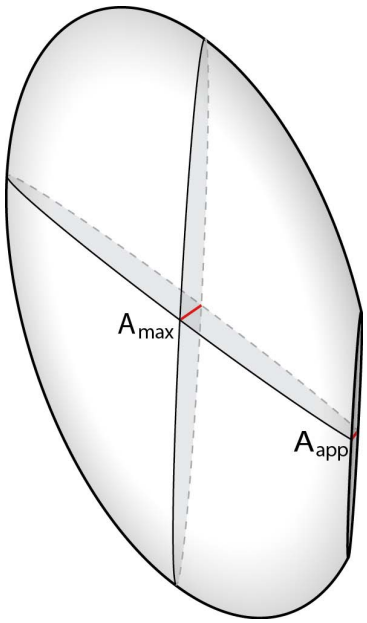


Figure 44: Basic illustration for the assumed cutting model. The vein is shown as an ellipsoid with a maximum Aperture A_{max}. Cutting the vein peripheral leads to very small apparent apertures.

4.3. Aperture distribution

As the measurement of apparent aperture distribution in Figures 30 and 33 show, apparent aperture frequency follows a power law. A LHT fall-off is observed for apertures $\leq 10\,\mu$m which is generally explained by reaching the resolving limit. In the following another approach will be described, explaining the fall-off assuming a minimum aperture.

4.3.1. Monte Carlo Simulation

The first assumption for the model is that microveins in thin sections are cut in random distances from their center. Secondly a minimum aperture c_0 is assumed. The situation of cutting is illustrated in Figure 44. To make the model as simple as possible it was additionally assumed that each vein is cut perpendicular to the plane spanned by both of their big semi-axes. Because fractures are described as very flat ellipsoids with equal semi-axis a and b (Atkinson, 1989) they can be described by the equation for ellipsoids which is

$$\frac{x^2}{a^2} + \frac{y^2}{b^2} + \frac{z^2}{c^2} = 1 \tag{7}$$

where a,b and c are the semi-axes of the ellipsoid. The problem can be reduced into two dimensions by cutting the ellipsoid parallel to the x-z-plane. Substituting $z = A/2$, where A is the aperture, and solving the equation to A gives the aperture at point x for given c and a:

$$A(x) = 2c\sqrt{1 - \frac{x^2}{a^2}} \tag{8}$$

Before the calculation of aperture can be conducted, the distribution of the small semi-axis c, which controls the aperture, must be defined. The distribution shall follow the function

$$\lambda_i = k\,\rho_i^{\tau} \tag{9}$$

where λ_i represents the frequency of the aperture ρ and k is a constant. This formula, equivalent to Equation 5 (Page 42), produces a distribution with $lim_{\rho \searrow 0} = \infty$.

To compute power-law distributed apertures the Monte Carlo simulation (see A.3) uses a hit-and-miss algorithm (Schmidt, 2010). The first step is to generate a uniformly distributed value ρ_i between minimum aperture a_{min} and maximum aperture a_{max}. A maximum aperture must be used to define the range of aperture values of the simulation. Simultaneously a second uniformly distributed value λ_i is generated. If $\lambda_i \leq k \cdot \rho_i^{\tau}$ (Eq. 9) the aperture ρ_i is used to calculate the apparent aperture using Equation 8. The exponent τ, describing the distribution, is given in the following paragraphs. Then the long semi-axis a is defined by the ratio $a = f \cdot \rho_i$, implying the ellipsoids diameter is f-times bigger than its aperture. In the model f accounts for values from 100 to 1000. This assumption is derived from Figure 32 as it represents roughly the relation between aperture and length. However, the ratio has no influence on the resulting distribution since the cutting point on the x-axis is uniformly calculated.

For first simulation approaches the parameters derived by non-linear regression in Section 3.4.2 (Fig. 34) were used. The diagram in Figure 45 illustrate the simulation results for the appropriate values and the cumulative frequency of simulation and analysis. The cumulative frequency of the simulation shows generally a too low frequency compared to the microscopic analysis.

It is important to note that the parameters of the probability functions do not describe the real distribution of veins because the microscopic analysis contains all kinds of veins. This especially includes crack-seal microveins and deviation from real aperture aroused by oblique intersection of microveins. Their measurement tampers the analysis and therefore the regression parameters as well. So additionally a cutting algorithm was implemented, post-processing the calculated apparent apertures after $a_a = a_0/sin(\alpha)$ where α is a uniformly distributed angle between α_{min} and 90 °. This post-processing produces a well estimated error caused by different angle cuttings and shifts the com-

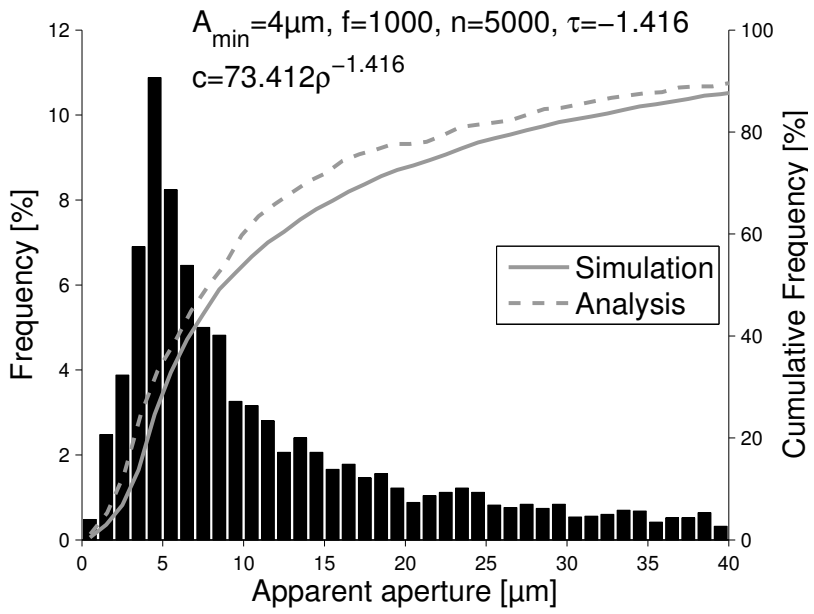


Figure 45: Comparison between microscopic analysis and simulation. The bars represent the simulated distribution. Modeling parameters are displayed on top of the histogram and were derived from Figure 34.

puted apertures towards bigger apertures.

Assuming an estimated minimum cutting angle of 45 ° enlarges the gap at larger apertures. Therefore the exponent τ must be lowered to reach the best fitting curve. Lowering τ produces a higher slope towards small apertures and respects the occurrence of larger veins caused by multiple events as well (like crack-seal). Using a trial-and-error approach on τ leads to the histogram displayed in Figure 46 (left hand side) fitting very well on the microscopic analysis data.

Comparison of the simulated and measured distribution using cumulative frequency after Pickering et al. (1995) is pictured in Figure 47. The fractal dimension of the model is $D = -1.006$ and also shows the good correlation between modeled and measured vein population.

Comparison

Holland and Urai (2010) measured the fractal dimension of a two-dimensional vein pattern using a box-counting algorithm for box sizes of 10 μm to 10 mm. The power-law correlated distribution showed a fractal dimension of $D = 1.89$. Downscaling of D to one dimension leads to $D = 0.89$ which deviates 13 % from the dimension measured in this study. Both values of fractal dimension therefore show that similar systems were measured. However, the deviation can be explained by the crack-seal network which was measured by Holland. In contrast in this thesis solitary microveins were measured.

LHT fall-off is common in vein aperture analyses (Barton and Zoback, 1990; Pickering

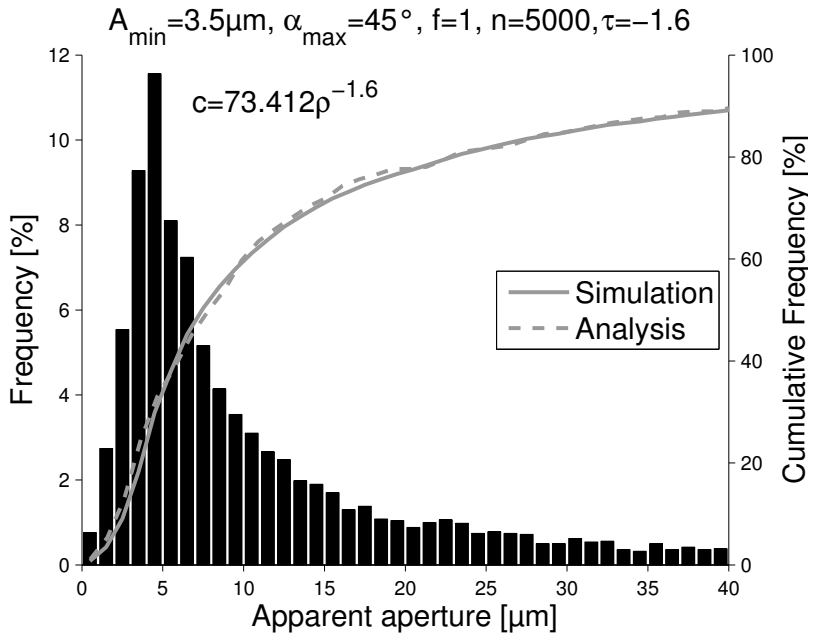


Figure 46: Model using cutting simulation for uniformly distributed cutting angle $\alpha \in [45°; 90°]$. For better fit τ was adjusted.

et al., 1995; Odling, 1997; Renard et al., 2005) and must therefore not be underestimated. However, some studies do not show a LHT fall-off which presumably is caused by the ending of the self-similar system before effects of resolution affect the measurements (Wong et al., 1989; Holland and Urai, 2010). Since in this study resolution effects occur they will be taken into account in the following interpretation.

Interpretation

Generally the modeling approach very well fits to the measured apparent aperture distribution. However, there are many sources of errors like veins created by multiple events or LHT fall-off due to cutting effects. Therefore basically two opportunities are available explaining the shape of the frequency distribution.

1. **Minimum aperture**

   As the model shows the distribution can result from a minimum vein aperture. The minimum aperture might be evidence for the mineralization of fractures at a certain minimum aperture. This assumption is derived from the fact that fractures exist in all apertures following a power law (Atkinson, 1989; Wong et al., 1989). Then the function describing the fracture aperture distribution also describes the distribution of vein apertures. Since microveins arise of fractures, their frequency distribution would follow the same distribution as the fracture distribution with a maximum peak at the minimum vein aperture.

   Another process creating the distribution might be snapping of microveins. This

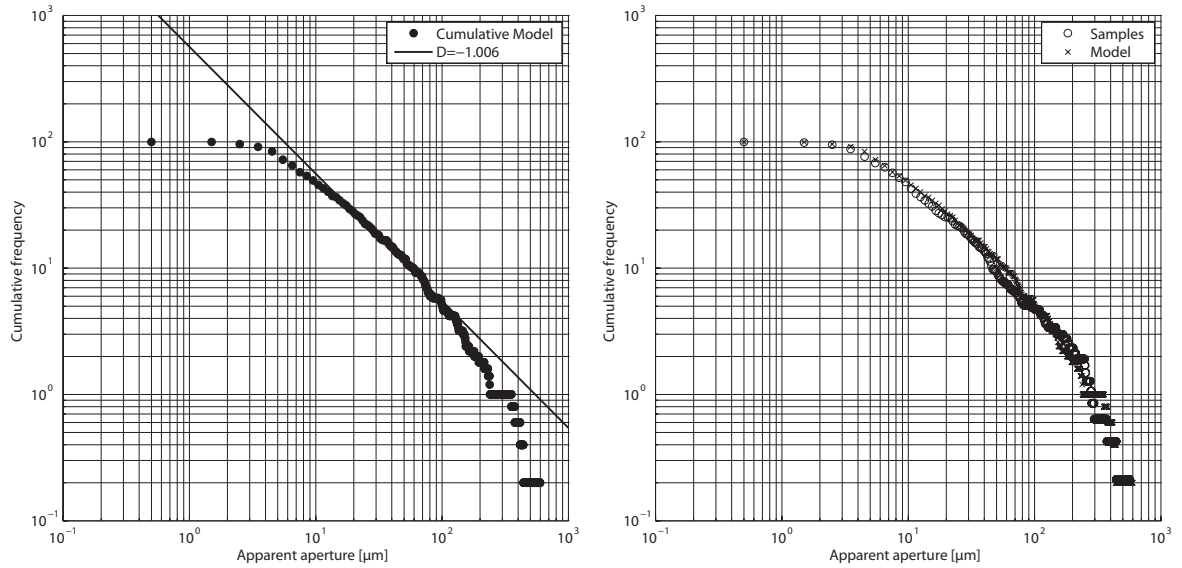


Figure 47: Left: Cumulative frequency distribution of modeled distribution (Fig. 46 left hand side, n=500). Fractal dimension D is -1.006 for apertures from 10 to 100 μm. Right: Cumulative distributions of samples and model plotted into one diagram.

is equivalent to a mixture of models 2, 4 and 5 for mechanical strength proposed by Holland and Urai (2010). In these models (Fig. 48) tensile strength of "the matrix is much weaker than the interface of the cement" (2), "the cement is slightly stronger than the other elements" (4) or "the strength of the interface is significantly smaller than the other two materials" (5) (Holland and Urai, 2010). Assuming a minimum aperture a certain percentage of fractures might develop, following model 4 or 5, at the interface of mineralized former fractures forming host rock inclusion bands. The remaining percentage of fractures would then create solitary veins, following model 2, which could also result in a power-law aperture distribution.

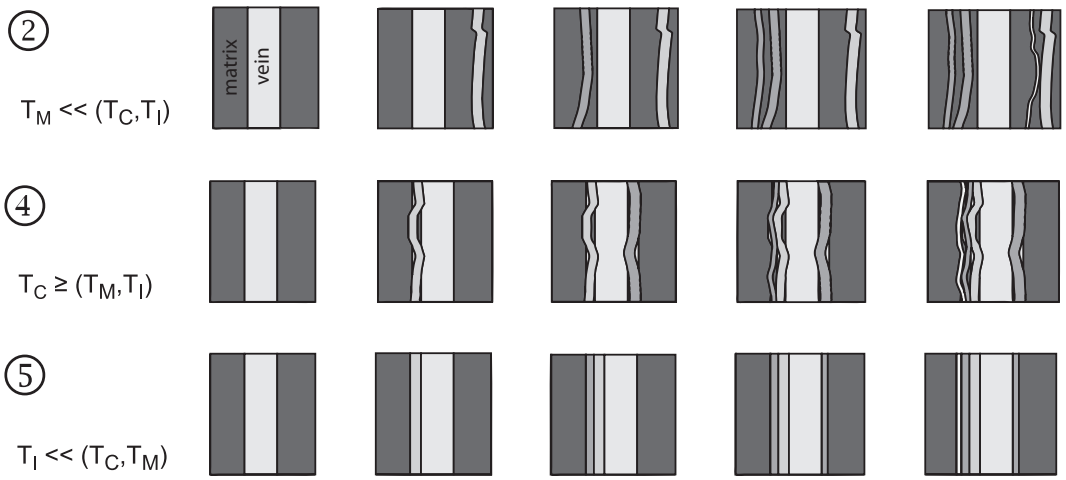


Figure 48: Conceptional model on the impact of mechanical strength of matrix T_M, vein cement T_C and the interface T_I (Holland and Urai, 2010).

2. **Resolution**

   The thickness of the observed thin sections were about 30 μm and by this about ten times larger than the probable minimum vein aperture. Therefore a microvein with an aperture smaller than 3.5 μm could be undetected if it intersects the cutting plane at a low angle as introduced in Section 2.2.3 (Fig. 12). Examining the lengths of joints in a joint system at different scales, Odling (1997) observed several power-law distributions. Each of the distributions at high scales had a LHT fall-off where small scale distributions show a log-linear curve. Hence it is possible, that the distribution of microveins continues below the maximum peak at 3.5 μm.

5. Conclusion

1. In all thin sections microveins were identified, in rock which have no veins visible with the naked eye. These samples were difficult to find in the field. The hypothesis "microveins are ubiquitous in the southern Jabal Akhdar" can not be rejected.

2. The central hypothesis of a minimum vein aperture could not be rejected as well. Thin section analysis shows that there are much less microveins below a thickness of 3.5 μm than above. A Monte Carlo Simulation with the proposed model of a minimum aperture shows a significant correlation between model and measured population. However, this can also be caused by decreasing visibility of veins slightly oblique to the line of sight in the microscope. Also comparison with other studies which sampled power-law distributed populations (Pickering et al., 1995; Odling, 1997; Renard et al., 2005) dispute the proposed model. Therefore, more work is needed to test this hypothesis.

3. In the fine-grained matrix (average grain size 4.2 μm) veins develop in grain boundary fractures by epitaxial growth on matrix grains.

4. In larger grains (e.g. fossils) veins develop in intra-granular fractures.

5. Extreme growth competition produces veins with larger grains than the matrix.

6. The presence of inclusion bands, branching veins etc indicates multiphase opening and sealing of a vein. The absence of these suggests, but does not prove, a single crack-seal event.

6. Outlook

Microveins are easier to examine in 3 μm thin sections as shown in Section 3.4.3. They decrease cutting effects and thus allow a better examination of microstructures. Enhancement of resolution power is given in usage of oil immersion objectives as well as usage of blue light. Here 100x oil immersion objectives are not usable for thick thin sections as some attempts at this study showed. The usage of blue light results, according to Equation 4, in a higher resolution power since the short wavelength allows more details to be observed. Compared to 30 μm thin sections those with a thickness of 3 μm show very little contrast. Therefore, usage of cathodoluminescence could improve the measurements. Furthermore, to reduce the LHT fall-off, only microveins of one set

should be examined. This allows to perpendicular cut the veins for thin section analysis and thus reduces errors due to cutting effects.

SEM imagery of microveins by etching of a polished surface showed good results at the first attempt. Even though the resolving power is much higher than light-microscopes' resolution, microveins smaller than 10 μm are presumably hard to find. Although a first try to detect veins by changes in chemical composition failed (EDX mapping) further work on this sector could be successful. The samples' morphology was, due to the strong acid, very high and made interface detection difficult. Thus more details might be observed if the samples are etched with weaker acids.

7. Acknowledgements

The creation of this Bachelor Thesis offered me the unique chance to create a scientific work for the very first time. Furthermore in the course of this thesis I had the possibility to work on a topic from the first sampling in the field to the interpretation of my observations in the end.

Therefore first of all I would like to thank Prof. Dr. Janos Urai for supporting my efforts doing my Bachelor Thesis in Oman Mountains and giving me such a versatile topic. At this point I would also like to thank Max Arndt and Simon Virgo, who I could attend to on my field work trip to Oman, for the outstanding support in all stages of my work.

I am also pleased to thank Werner Kraus, for cutting the samples and preparing my thin sections, as well as Joyce Schmatz, giving me the opportunity to examine a sample in a SEM.

Special thanks goes to Sina Panitz, supporting me in any part of the work and for proofreading the first version of this thesis. Furthermore I would like to thank Steffen Abe for proofreading.

Last but not least I would like to thank my parents for financial and ideal support, making it possible reaching the Bachelor's degree in Applied Geosciences.

This Thesis is part of the DGMK-Project 718 "Mineral Vein Dynamics Modelling". It has been funded by the companies ExxonMobil Production Deutschland GmbH, GDF SUEZ E&P Deutschland GmbH, RWE Dea AG and Wintershall Holding GmbH in the course of the E&P-Forschungsfonds of the WEG Wirtschaftsverband Erdöl- und Erdgasgewinnung e.V..

References

Barry Kean Atkinson, editor. *Fracture Mechanics of Rock*. Academic Press Limited, 1989.

C. A. Barton and M. D. Zoback. Self-similar distribution of macroscopic fractures at depth in crystalline rock in the cajon pass scientific drillhole. *Rock Joints*, 1990.

Stephan Becker, Christoph Hilgers, Peter A. Kukla, and Janos L. Urai. Crack-seal microstructure evolution in bi-mineralic quartz-chlorite veins in shales and siltstones from the rwth-1 well, aachen, germany. *Journal of Structural Geology*, 33:676–689, 2011.

Paul D. Bons. The formation of veins and their microstructures. http://virtualexplorer.com.au/special/meansvolume/contribs/bons/index.html, 2000. URL `http://virtualexplorer.com.au/special/meansvolume/contribs/bons/index.html`.

J.-P. Breton, F. Béchennec, J. Le Métour, L. Moen-Maurel, and P. Razin. Eoalpine (cretaceous) evolution of the oman tethyan continental margin: insights from a structural field study in jabal akhdar (oman mountains). *GeoArabia*, 9(2), 2004.

Marc Holland and Janos L. Urai. Evolution of anastomosing crack-seal vein networks in limestones: Insight from an exhumed high-pressure cell, jabal shams, oman mountains. *Structural Geology*, 32(9):1279–1290, 2010.

Mathworks. *Image Processing Toolbox - User's Guide*, Matlab R2011a edition, 2011.

NOAA/NGDC & CIRES. World magnetic model, 2009. URL `http://ngdc.noaa.gov/geomag/WMM/`.

Noelle E. Odling. Scaling and connectivity of joint systems in sandstones from western norway. *Journal of Structural Geology*, 19(10):1257–1271, 1997.

Jon E. Olson. Sublinear scaling of fracture aperture versus length: An exception or the rule? *Journal of Geophysical Research*, 108(B9), 2003.

Timothy S. Paulsen, Richard D. Jarrard, and Terry J. Wilson. A simple method for orienting drill core by correlating features in whole-core scans and oriented borehole-wall imagery. *Journal of Structural Geology*, 24:1233–1238, 2002.

G. Pickering, J. M. Bull, and D. J. Sanderson. Sampling power-law distributions. *Tectonophysics*, 248, 1995.

Gérard Poupeau. Late thermal evolution of the oman mountains subophiolitic windows: Apatite fission-track thermochronology. *Geology*, 26(12):1139 – 1142, 1998.

Alexander Raith. Creation of a high resolution panorama, capturing a high density calcite vein network from a polished limestone outcrop in the oman mountains. BSc Thesis, RWTH Aachen, 2010.

John G. Ramsay. The crack-seal mechanism of rock deformation. *Nature*, 284, March 1980.

Francois Renard, Muriel Andreani, Anne-Marie Boullier, and Pierre Labaume. *Crack-seal patterns: records of uncorrelated stress release variations in crustal rocks*, volume 243, pages 67 – 79. Geological Society, London, Special Publications edition, 2005.

Jörn Schmidt. *Programmierung naturanaloger Verfahren - Soft computing und verwandte Methoden mit 9 Tabellen [mit Online-Service]*. Vieweg Teubner, Wiesbaden, 1st edition, 2010. ISBN 9783834808226.

Michael P. Searle. Sequence of thrusting and origin of culminations in the northern and central oman mountains. *Journal of Structural Geology*, 7(2):129 – 143, 1985.

Michael P. Searle. Structural geometry, style and timing of deformation in the hawasina window, al jabal al akhdar and saih hatat culminations, oman mountains. *GeoArabia*, 12 (2):99 – 130, 2007.

Robert J. Twiss and Eldridge M. Moores. *Structural Geology*. Number Second Edition. Susan Finnemore Brennan, 2007.

Jan M. Vermyle and Christopher H. Scholz. Relation between vein length and aperture. *Journal of Structural Geology*, 17(3):423 – 434, 1995.

C. Y. Wang and Y. Sun. Oriented microfractures in cajon pass drill cores: Stress field near the san andreas fault. *Journal of Geophysical Research*, 95:11135–11142, 1990.

Teng-Fong Wong, Joanne T. Fredrich, and Gabriel D. Gwanmesia. Crack aperture statistics and pore space fractal geometry of westerly granite and rutland quartzite: Implications for an elastic contact model of rock compressibility. *Journal of Geophysical Research*, 94(B8): 10267 – 10278, 1989.

Patrick Wüstefeld. Capturing a world-class outcrop of a quality calcite vein network on a polished limestone outcrop in the oman mountains: Creation of a high resolution panorama and microstructural vein description. BSc Thesis, RWTH Aachen, 2010.

A. MATLAB Code

A.1. Spatial orientation calculation

A.1.1. StrikeDipEW_HOR.m

Listing 1: StrikeDipEW_HOR.m

```
%% Strike-Dip Calculation EW-HOR Planes
%
% The data must be recorded as alternating pairs of
% EW and HOR-values. Encoding must be ANSI! Length-Data is not used.
% Bugs using Photoshop for angle-measurement: eastwards / westwards dipping
% can not be recognized
%
% This script was tested for all quadrants

clear all

[filename,path] = uigetfile('*.txt','West-East / Horizontal');
data = readPS(filename,path);

% Sort data
% ---------
% Seperates EW and HOR records (Odd index = EW, even = HOR)

n = length(data);
EW = [];
HOR = [];

for i=1:n
    if mod(i,2) == 1
        EW(length(EW)+1,1) = data(i);
    else
        HOR(length(HOR)+1,1) = data(i);
    end
end
clearvars n i data textData

% Geographic angle conversion (HOR)
% ---------------------------------

n = length(HOR);
for i=1:n
    if HOR(i) > 0
        HOR(i) = HOR(i) - 180;
    end
    HOR(i) = abs(HOR(i)) + 90;
end
clearvars i n

%% Define quadrants
prompt = 'Enter quadrant (eg. a3)';
dlg_title = 'Define the quadrant for angle conversion';
temp = inputdlg(prompt,dlg_title);
quadrant = temp{1,1};

%% a-quadrants

if quadrant(1) == 'a'

if quadrant == 'a1' | quadrant == 'a4'
    for i=1:length(HOR)
        a=EW(i);
        if a < 0
            EW(i) = 180 - abs(a);
        end
    end
elseif quadrant == 'a2' | quadrant == 'a3'
    for i=1:length(HOR)
        a=EW(i);
        if a > 0
            EW(i) = 180 - a;
        else
            EW(i) = abs(a);
        end
    end
else
    msgbox('Wrong input','Error','error')
    stop
end

%% b-quadrants
```

```
elseif quadrant(1) == 'b'

if quadrant == 'b1' | quadrant == 'b4'
    for i=1:length(HOR)
        a = EW(i);
        if a > 0
            EW(i) = 180-a;
        else
            EW(i) = abs(a);
        end
    end
elseif quadrant == 'b2' | quadrant == 'b3'
    for i=1:length(HOR)
        a = EW(i);
        if a < 0
            EW(i) = 180 - abs(a);
        end
    end
else
    msgbox('Wrong input','Error','error')
    stop
end

end

%% Vector based calculation

% Create normal vector on plane
% ----------------------------
% u = vector in hor-plane
% v = vector in vertical plane

for i=1:length(HOR)

    u(1) = sin(HOR(i)*pi/180);
    u(2) = cos(HOR(i)*pi/180);
    u(3) = 0;

    v(1) = cos(EW(i)*pi/180);
    v(2) = 0;
    v(3) = -sin(EW(i)*pi/180);

    % Crossproduct
    n = cross(u,v);

    % Normalize
    n_abs = sqrt(n(1)^2 + n(2)^2 + n(3)^2);

    n = n/n_abs;

    % Vector must face upwards
    if n(3) < 0
        n = -1*n;
    end

    % Calculate Dip
    DIP(i,1) = 90 - asin(n(3))*180/pi;

    % Calculate Dip Direction
    c = n(1)/abs(n(1)) * acos(n(2));
    l = sqrt(n(1)^2 + n(2)^2);
    if c < 0
        DD(i,1) = 360 + n(1)/abs(n(1)) * acos(n(2)/l)*180/pi;
    else
        DD(i,1) = n(1)/abs(n(1)) * acos(n(2)/l)*180/pi;
    end

    clearvars u v n

end

%% Write stereo32-file

filename = regexprep(filename, '.txt','.stereo');
stereo32(DIP,DD,filename,path);
msgbox('Finished')
```

A.1.2. StrikeDipNS_HOR.m

Listing 2: StrikeDipNS_HOR.m

```
%% Strike-Dip Calculation NS-HOR
%
% This script calculates true dip and dip direction from adjacent planes
% that have been measured in Photoshop (R).
% The data must be recorded as alternating pairs of NS and HOR-values.
% Encoding should be ANSI.
```

```
%
% This script was tested for all quadrants
%
% If the outputfile is empty check the encoding of the input file!
%
% Notes:
% Dip angle conversion
% --------------------
% The Dip angle is measured from N to S
% Dip < 90deg = top to North dipping
% Dip > 90deg = top to South dipping

clear all

[filename,path] = uigetfile('*.txt','North-South␣Horizontal');
data = readPS(filename,path);

% Sort data
% ---------
% Seperates NS and HOR records (Odd index = NS, even = HOR)

n = length(data);
NS = [];
HOR = [];

for i=1:n
    if mod(i,2) == 1
        NS(length(NS)+1,1) = data(i);
    else
        HOR(length(HOR)+1,1) = data(i);
    end
end
clearvars n i data textData

% Geographic angle conv ersion (HOR)
% ----------------------------------

n = length(HOR);
for i=1:n
    if HOR(i) > 0
        HOR(i) = HOR(i) - 180;
    end
    HOR(i) = abs(HOR(i)) + 90;
end
clearvars i n

%% Define quadrant
prompt = 'Enter␣quadrant␣(eg.␣a3)';
dlg_title = 'Define␣the␣quadrant␣for␣angle␣conversion';
temp = inputdlg(prompt,dlg_title);
quadrant = temp{1,1};

%% a-quadrants

if quadrant(1) == 'a'

% Dip angle conversion
% --------------------

if quadrant == 'a1' | quadrant == 'a2'

    for i=1:length(NS)
        a = NS(i);
        if a > 90
            NS(i) = 270 - a;
        elseif a > 0
            NS(i) = 90 - a;
        elseif a > -90
            NS(i) = 90 + abs(a);
        elseif a >= - 180
            NS(i) = abs(a) - 90;
        end
    end

elseif quadrant == 'a3' | quadrant == 'a4'

    for i=1:length(NS)
        a = NS(i);
        if a > 90
            NS(i) = a - 90;
        elseif a > 0
            NS(i) = a + 90;
        elseif a > -90
            NS(i) = 90 - abs(a);
        elseif a >= -180
            NS(i) = 270 - abs(a);
        end
    end
else
    msgbox('Wrong␣input','Error','error')
```

```
    stop
end

%% For b-quadrants

elseif quadrant(1) == 'b'

if quadrant == 'b1' | quadrant == 'b2'
    for i=1:length(HOR)
        a = NS(i);
        if a > 90
            NS(i) = a-90;
        elseif a > 0
            NS(i) = a+90;
        elseif a > -90
            NS(i) = 90-abs(a);
        elseif a >= -180
            NS(i) = 270-abs(a);
        end
    end

elseif quadrant == 'b3' | quadrant == 'b4'

    for i=1:length(HOR)
       a = NS(i);
        if a > 90
            NS(i) = 270-a;
        elseif a > 0
            NS(i) = 90-a;
        elseif a > -90
            NS(i) = 90+abs(a);
        elseif a >= -180
            NS(i) = abs(a)-90;
        end
    end

else
    msgbox('Wrong input','Error','error')
    stop
end

end

%% Vector based calculation

% Create normal vector on plane
% -----------------------------
% u = vector in hor-plane
% v = vector in vertical plane

for i=1:length(HOR)

    u(1) = sin(HOR(i)*pi/180);
    u(2) = cos(HOR(i)*pi/180);
    u(3) = 0;

    v(1) = 0;
    v(2) = cos(NS(i)*pi/180);
    v(3) = -sin(NS(i)*pi/180);

    % Crossproduct
    n = cross(u,v);

    % Normalize
    n_abs = sqrt(n(1)^2 + n(2)^2 + n(3)^2);

    n = n/n_abs;

    % Vector must face upwards
    if n(3) < 0
        n = -1*n;
    end

    % Calculate Dip
    DIP(i,1) = 90 - asin(n(3))*180/pi;

    % Calculate Dip Direction
    c = n(1)/abs(n(1)) * acos(n(2));
    l = sqrt(n(1)^2 + n(2)^2);
    if c < 0
        DD(i,1) = 360 + n(1)/abs(n(1)) * acos(n(2)/l)*180/pi;
    else
        DD(i,1) = n(1)/abs(n(1)) * acos(n(2)/l)*180/pi;
    end

    clearvars u v n

end

%% Write stereo32-file
```

```
filename = regexprep(filename, '.txt','.stereo');
stereo32(DIP,DD,filename,path);
msgbox('Finished!')
```

A.1.3. readPS.m

Listing 3: readPS.m

```
%% Reads Photoshop txt-Files
% file must be ANSI encoded

function [angle] = readPS(filename,path)

fid = fopen([path,filename]);

% Read only angles
data = textscan(fid, '%*q␣%*q␣%*q␣%*q␣%*q␣%*q␣%*q␣%*q␣%q',...
    'Delimiter', '\t', 'HeaderLines', 1, 'EndOfLine', '\n');

fclose(fid);

% Save angles as strings
angle_str = data{1,1};

angle=zeros[length(angle_str),1];

for i=1:length(angle_str)
    % replace ',' with '.'
    angle_str(i)=regexprep(angle_str(i), ',','.');
    % convert string to double
    angle(i,1)=str2double(angle_str(i));
end
```

A.1.4. stere32.m

Listing 4: stereo32.m

```
%% stereo32
% Creates an output file for Stereo32 from one column arrays 'inp_dip' and
% 'inp_dipdir'

function stereo32(inp_dip,inp_dipdir,filename,path)

%check, if array sizes are equal; if not there will be an error because
%nrows is undefined
n_dip = size(inp_dip);
n_dipdir = size(inp_dipdir);
if n_dip==n_dipdir
    nrows = n_dip;
end

%default string for stereo32
def_sym_str = '␣P␣Scan␣{N=C,M=3100000000000000000100}';

%% Writing the file
fid = fopen([path,filename],'w');

% creates strings for dip and dip-direction, which will be merged and
% written into the file
for i=1:nrows
    %creating dip-string
    if inp_dipdir(i,1) < 10
        dipdir = ['␣␣',sprintf('%g',round(inp_dipdir(i,1)*100)/100)];
    elseif inp_dipdir(i,1) < 100
        dipdir = ['␣',sprintf('%g',round(inp_dipdir(i,1)*100)/100)];
    else
        dipdir = sprintf('%g',round(inp_dipdir(i,1)*100)/100);
    end
    %creating dip direction string
    if inp_dip(i,1) < 10
        dip = ['␣',sprintf('%g',round(inp_dip(i,1)*100)/100)];
    else
        dip = sprintf('%g',round(inp_dip(i,1)*100)/100);
    end
    %merge strings
    str = [dipdir,'␣␣',dip,def_sym_str];
    %write into file
    fprintf(fid, '%s\n',str);
end

fclose(fid);
```

A.2. Automated aperture measurement

A.2.1. execute_me.m

Listing 5: aperture.m

```
function aperture(filename)

% This script loads discretized images of veins (256 grayscale) and returns
% the listet values. It starts counting from the top left corner of the
% image and counts rows before colums. The measured values are:
%
% rock_top  - Number of black pixels / distance from the top border to the
%             first white pixel
% rock_bot  - Number of black pixels / cumulative distance since the first
%             white pixel
% rock_bot2 - Number of black pixels / distance since the last white pixel
%             to the bottom border of the image
% vein      - Number of white pixels / cumulative distance in a column
% vein2     - Total number of pixels / distance from first to last white
%             pixel
%
% The returned values are rock_bot, vein, vein2

% ##########################################
% Define process parameters in this part
% ##########################################

% Factor defines the scale of one pixel in µm
% for 20x Objective use 1px = µ0.3432m
  factor = 0.3432;

% ##########################################

fprintf(['Imagefile: ',filename,'\n']);
img = imread(filename);
img = img(:,:,1);

[n_rows,n_cols] = size(img);

% Predifine size of arrays
rock_bot(n_cols) = 0;
rock_bot2(n_cols) = 0;
rock_top(n_cols) = 0;
vein(n_cols) = 0;

fprintf('Processing...\n');

for i=1:(n_cols)

    % sec indicates the actual position in relation to the vein
    % top - above the vein
    % bot - below the vein
    sec = 'top';
    rock_bot(i) = 0;
    rock_top(i) = 0;
    vein(i) = 0;
    rock_bot2(i)=0;
    for j=1:n_rows
        if (img(j,i) == 0) & (sec == 'bot')
            rock_bot(i) = rock_bot(i) + 1;
        elseif img(j,i) == 255
            vein(i) = vein(i) + 1;
            sec = 'bot';
        elseif (img(j,i) == 0) & (sec == 'top')
            rock_top(i) = rock_top(i) + 1;
        end
    end
    % Count from bottom to top for rock_bot2
    for j = 1:n_rows
        if img(n_rows-j+1,i) == 0
            rock_bot2(i) = rock_bot2(i) + 1;
        else
            break
        end
    end
end

% Convert pixel values into µm
vein = vein * factor;
rock_bot = rock_bot * factor;
rock_bot2 = rock_bot2 * factor;
rock_top = rock_top * factor;
x = [1:n_cols] * factor;

% Calculate vein aperture from rock_top2
```

```
vein2 = n_rows*factor - rock_bot2 - rock_top;

% Write data into File

filename = regexprep(filename, '.tif','.txt');
fid = fopen(filename,'w');

fprintf(fid,'%s\n\n',regexprep(filename,'.txt',''));

fprintf(fid,'%s\t','x µ[m]');
fprintf(fid,'%s\t','Hostrock µ[m]');
fprintf(fid,'%s\t','Aperture 1 µ[m]');
fprintf(fid,'%s\t','Aperture 2 µ[m]');
fprintf(fid,'\n');
fprintf(fid,'%f\t%f\t%f\t%f\n',[x;rock_bot;vein;vein2]);

fclose(fid);

fprintf('Finished Image\n\n');
```

A.2.2. aperture.m

Listing 6: aperture.m

```
function aperture(filename)

% This script loads discretized images of veins (256 grayscale) and returns
% the listet values. It starts counting from the top left corner of the
% image and counts rows before colums. The measured values are:
%
% rock_top  - Number of black pixels / distance from the top border to the
%             first white pixel
% rock_bot  - Number of black pixels / cumulative distance since the first
%             white pixel
% rock_bot2 - Number of black pixels / distance since the last white pixel
%             to the bottom border of the image
% vein      - Number of white pixels / cumulative distance in a column
% vein2     - Total number of pixels / distance from first to last white
%             pixel
%
% The returned values are rock_bot, vein, vein2

% ##########################################
% Define process parameters in this part
% ##########################################

% Factor defines the scale of one pixel in µm
% for 20x Objective use 1px = µ0.3432m
  factor = 0.3432;

% ##########################################

fprintf(['Imagefile: ',filename,'\n']);
img = imread(filename);
img = img(:,:,1);

[n_rows,n_cols] = size(img);

% Predifine size of arrays
rock_bot(n_cols) = 0;
rock_bot2(n_cols) = 0;
rock_top(n_cols) = 0;
vein(n_cols) = 0;

fprintf('Processing...\n');

for i=1:(n_cols)

    % sec indicates the actual position in relation to the vein
    % top - above the vein
    % bot - below the vein
    sec = 'top';
    rock_bot(i) = 0;
    rock_top(i) = 0;
    vein(i) = 0;
    rock_bot2(i)=0;
    for j=1:n_rows
        if (img(j,i) == 0) & (sec == 'bot')
            rock_bot(i) = rock_bot(i) + 1;
        elseif img(j,i) == 255
            vein(i) = vein(i) + 1;
            sec = 'bot';
        elseif (img(j,i) == 0) & (sec == 'top')
            rock_top(i) = rock_top(i) + 1;
        end
    end
    % Count from bottom to top for rock_bot2
```

```
    for j = 1:n_rows
        if img(n_rows-j+1,i) == 0
            rock_bot2(i) = rock_bot2(i) + 1;
        else
            break
        end
    end
end

% Convert pixel values into µm
vein = vein * factor;
rock_bot = rock_bot * factor;
rock_bot2 = rock_bot2 * factor;
rock_top = rock_top * factor;
x = [1:n_cols] * factor;

% Calculate vein aperture from rock_top2
vein2 = n_rows*factor - rock_bot2 - rock_top;

% Write data into File

filename = regexprep(filename, '.tif','.txt');
fid = fopen(filename,'w');

fprintf(fid,'%s\n\n',regexprep(filename,'.txt',''));

fprintf(fid,'%s\t','x µ[m]');
fprintf(fid,'%s\t','Hostrock µ[m]');
fprintf(fid,'%s\t','Aperture 1 µ[m]');
fprintf(fid,'%s\t','Aperture 2 µ[m]');
fprintf(fid,'\n');
fprintf(fid,'%f\t%f\t%f\t%f\n',[x;rock_bot;vein;vein2]);

fclose(fid);

fprintf('Finished Image\n\n');
```

A.2.3. process.m

Listing 7: process.m

```
 function [dist_total, aperture_mean, sinuosity] = process(filename)

% This script ist designed to process aperture vein data obtained by the
% aperture.m-script
% ------------------------------------------------------------------------
% Process:
% 1. Delete all zero-Data at beginning and end of the table
% 2. Calculate average aperture for visualization
% 3. Calculate total distance
% 4. Calculate Sinuosity
% 5. Return total distance, mean aperture and sinuosity
% ------------------------------------------------------------------------

% ############################################################
% Define process parameters in this part
% ############################################################

% Define minimum lack of veins for deleting rows in µm (!)
  min_veinlack = 10;

% Degree of smoothing neighbouring data in µm
  degree = 50;

% ############################################################


% Import data
% ----------------------------------------------------------
data = importdata(filename,'\t',3);

% Data structure with tab delimiters (first 3 lines are text):
% ----------------------------------------------------------
% Name_of_the_File
%
% x µ[m] Hostrock µ[m]    Aperture 1 µ[m]  Aperture 2 µ[m]
% 0.343200      70.699200       0.000000        -70.699200
% ...        ...          ...          ...
% ----------------------------------------------------------

data = data.data;
l = length(data);

%% Step 1
% Delete Zeros in apertures at beginning of the table
% ----------------------------------------------------------
```

```
del_row = 0;
for i=1:l
    if data(i,3) == 0
        del_row = del_row + 1;
    else
        break
    end
end
for i=del_row:-1:1
    data(i,:) = [];
end
l = length(data);

% Delete Zeros in apertures at the end of the table
% -------------------------------------------------------------
del_row = 0;
for i=l:-1:1
    if data(i,3) == 0
        del_row = del_row + 1;
    else
        break
    end
end
for i=l:-1:(l-del_row+1)
    data(i,:) = [];
end
l = length(data);
clearvars del_row

% Correct length table
% -------------------------------------------------------------
% steps delta_l
delta_l = data(2,1) - data(1,1);
for i=1:l
   data(i,1) = i*delta_l;
end

% Convert absolute degreeinto relative for rlowess smoothing
% -------------------------------------------------------------
% equivalent pixel length
degree = degree/delta_l;
% calculate percentage of actual dataset
degree = degree/length(data);

%% Step 2
% calculate average aperture
% -------------------------------------------------------------

% Delete Zero-Apertures
% -------------------------------------------------------------
% use aperture2

% min_veinlack is defined at the beginning
min_pix = ceil(min_veinlack/delta_l);

aperture = data(:,4);
l_a = length(aperture);

k = 0;
for i=l_a:-1:1
    if aperture(i) <= 0
        aperture(i) = 0;
        k = k + 1;
    elseif aperture(i) > 0 && k > min_pix
        % delete rows form i+1 to i+k which contain zeros
        aperture(i+1:i+k,:) = [];
        k = 0;
    end
end

% Smooth data and calculate mean aperture
% -------------------------------------------------------------

aperture_s = smooth(aperture,degree,'rlowess');
aperture_mean = mean(aperture_s);

%% Step 3
% Calculate total distance
l = length(data);
delta_h = data(l,2)-data(1,2);
dist_total = sqrt(delta_h^2 + data(l,1)^2);

%% Step 4
% Calculate sinuosity
% -------------------------------------------------------------

hostrock = data(:,2);
% A) Cut off minimum hostrock-values / parts with lack of veins
% -------------------------------------------------------------
```

```
for i=1:l
    if hostrock(i)==0
        hostrock(i) = hostrock(i-1);
    end
end

% B) Flatten
% ------------------------------------------------------------

% B.1) linear regression chi^2
% ------------------------------------------------------------

x = data(:,1);

s_x = 0;
s_y = 0;
s_xy = 0;
s_x2 = 0;

y_m = mean(hostrock);
x_m = mean(x);
for i=1:l
    s_x = s_x + x(i);
    s_y = s_y + hostrock(i);
    s_xy = s_xy + x(i)*hostrock(i);
    s_x2 = s_x2 + x(i)^2;
end

b_xy = (l*s_xy-s_x*s_y)/(l*s_x2-s_x^2);
a_xy = y_m - b_xy*x_m;

% B.2) Flatten relating best-fit line
% ------------------------------------------------------------

for i=1:l
    hostrock(i) = hostrock(i) - (a_xy+b_xy*x(i));
end

% C) Smooth data
% ------------------------------------------------------------

% degree of smoothing is defined at the beginning

hostrock_s = smooth(hostrock,degree,'rlowess');

% D) Calculate Length
% ------------------------------------------------------------

len = 0;

for i=1:l-1
    len(i) = sqrt(delta_l^2 + (hostrock_s(i)-hostrock_s(i+1))^2);
end

len_total = sum(len);
sinuosity = len_total/dist_total;
```

A.3. Modelling aperture distribution

A.3.1. model.m

Listing 8: model.m

```
% Model to describe distribution of vein apertures in thinsections. Cracks
% are assumed to be ellipsoids with f-times bigger axes (a,b) than
% apertures (c). Minimal crack aperture is given by c0, the distribution of
% crack apertures decreases with rand^3

clear all;

% ######################################
% Define Parameters
% ######################################
% min_aperture      Minimum aperture
% max_aperture      Maximum aperture
% f                 Scale factor for a/b axis
% k                 Amount of simulated values
% a_d               Distribution coefficient
% tau               Distribution exponent
% shift_dist        determines distribution to use
% cut_simul         true = cutting is simulated
% max_alpha         maximum cutting angle
% class_l           Class length for histogram
% plot_dist_func    plots distribution function if true
% font_size         font size of plot annotations
```

```
% Vein properties
min_aperture = 3.5;
max_aperture = 120;
f = 1;

% Modeling properties
k = 500;
% Distribution properties
a_d = 73;
tau = -1.6;
shift_dist = false;
cut_simul = true;
max_alpha = 25;

% Histogram properties
class_l = 1;

% Plotting properties
plot_dist_func = false;
font_size = 15;

%% ######################################
% Here starts the code
%  ######################################
z(1) = 0;

fprintf('Starting␣simulation\n');
h = waitbar(0,'Simulation␣in␣progress...');
for j=1:k

    match = false;

    % Calculate random apertures following given distribution
    while match == false
        r_x = min_aperture + rand()*(max_aperture-min_aperture);
        r_y = 500*rand();
        if shift_dist == true
            if r_y < a_d*(r_x-min_aperture)^(tau) %727
                match = true;
            end
        else
            if r_y < a_d*r_x^(tau) %727
                match = true;
            end
        end
    end

    %define c, which is half aperture
    c = r_x/2;
    %define b, which depends on c
    b = f*c;
    %define cutting point random on b
    y=b*rand();

    z(length(z)+1)=2*c*sqrt(1-y^2/b^2);

    progress = j/k*100;
    waitbar(j/k,h,sprintf('%d%%␣-␣Simulation␣in␣progress...',floor(j/k*100)));
end
close(h);
z(:,1) = [];

%% execute cutting simulation

if cut_simul == true
    fprintf('Starting␣cutting\n');
    for i = 1:length(z)
        alpha = (90 + rand()*(90-max_alpha))*pi/180;
        %alpha = max_alpha*pi/180;
        z(i) = abs(z(i)/sin(alpha));
    end
end


%% ##############################################
%                  Histrogram
%  ##############################################
fprintf('Histrogram␣calculation...\n');
data = z;

n=length(data);

% min / max
xmin=0;
xmax=max(data);

% Calculate amount of classes
b = class_l;
k = ceil(xmax/b);
```

```
h=zeros(k,1);

for i=1:k
    x(i) = b/2 + b*(i-1);
end

for i=1:n
    idx=floor((data(i)-xmin)/b)+1;
    if(idx==(k+1))
        idx=k;
    end
    h(idx)=h(idx)+1;
end

% Normalize

fprintf('Normalize\n');
h = h/sum(h)*100;

% Calculate cumulative frequency

fprintf('Calculating␣cumulative␣frequency\n');
f_c(1) = h(1);
for i=2:length(h)
    f_c(i) = f_c(i-1) + h(i);
end

%% load cumulative from measurements

fprintf('Loading␣cumulative␣frequency␣from␣measurement\n');
t = load('cumulative_all.mat');
t = t.t;

fprintf('Norming␣on␣the␣same␣length\n');
% norm on the same length
for i = 1:length(t)
    if t(i,1) > max_aperture
        t(i:length(t),:)=[];
        break
    end
end

t = t/max(t(:,2))*100;

%% Calculate graph with true distribution

for i=1:length(x)
    c0_dist(i) = x(i)^(tau);
end

%% plot

fprintf('Creating␣plot\n');
% Create figure
figure1 = figure('PaperType','A4',...
    'Color',[1 1 1]);
    %'PaperSize',[20.98404194812 29.67743169791]);

xp_max = 40;


% Create bar
[AX,H1,H2] = plotyy(x,h,x,f_c,'bar','plot');


% Defining properties
set(get(AX(1),'Xlabel'),...
    'String','Apparent␣aperture␣μ[m]',...
    'FontSize',font_size);

set(get(AX(1),'Ylabel'),...
    'String','Frequency␣[%]',...
    'FontSize',font_size);

set(get(AX(2),'Ylabel'),...
    'String','Cumulative␣Frequency␣[%]',...
    'FontSize',font_size);

set(H1,'FaceColor',[0 0 0],...
    'EdgeColor',[0 0 0]);
set(H2,'Color',[0.6 0.6 0.6],...
    'LineWidth',2);
set(AX(1),...
     'TickDir','out',...
     'Box','off',...
     'XLim',[0 xp_max],...
     'YTick',[0:2:12],...
     'YLim',[0 12]);
set(AX(2),...
```

```
     'TickDir','out',...
     'Box','off',...
     'XTick',[],...
     'XLim',[0 xp_max],...
     'YTick',[0:20:100],...
     'YLim',[0 100],...
     'YColor',[0 0 0]);

% Add analyzed cumulative distribution
hold all
axes(AX(2))
lh = line(t(:,1),t(:,2));
set(lh,...
    'Color',[0.6 0.6 0.6],...
    'LineStyle','--',...
    'LineWidth',2);

leg = legend('Simulation','Analysis');

set(leg,...
    'Location','East',...
    'FontSize',font_size);
%    '{\alpha}_{max}=',num2str(max_alpha∞),', '...

if cut_simul == false
annotation('textbox',[0.15 0.9 0.1 0.1],...
    'String',['A_{min}=',num2str(min_aperture,2),'μm, '...
        'f=',num2str(f),', '...
        'n=',num2str(n),', '...
        '{\tau}=',num2str(tau)],...
    'FontSize',font_size,...
    'LineStyle','none');
else
annotation('textbox',[0.15 0.92 0.1 0.1],...
    'String',['A_{min}=',num2str(min_aperture,2),'μm, '...
        '{\alpha}_{max}=',num2str(max_alpha),'∞, '...
        'f=',num2str(f),', '...
        'n=',num2str(n),', '...
        '{\tau}=',num2str(tau)],...
    'FontSize',font_size,...
    'LineStyle','none');
end

if shift_dist == true
    equation_string = ['c=',num2str(a_d),'({\rho}-',num2str(min_aperture),'){^{',num2str(tau),'}}'];
else
    equation_string = ['c=',num2str(a_d),'{\rho^{',num2str(tau),'}}'];
    c0 = 0;
end

tb = annotation('textbox',[0.25 0.8 0.1 0.1],...
    'String',equation_string,...
    'LineStyle','none',...
    'FontSize',font_size,...
    'HorizontalAlignment','left');

%% calculate and plot distribution function
if plot_dist_func == true
dist_x = [1:1:xp_max];

if shift_dist == true
    for i = 1:length(dist_x)
        dist_y(i) = real(a_d*(dist_x(i)-min_aperture)^tau);
    end
else
    for i = 1:length(dist_x)
        dist_y(i) = real(a_d*dist_x(i)^tau);
    end
end

plot(dist_x,dist_y,'r','Parent',AX(1));
leg = legend('Simulation','Analysis','Calculation','Distr. Fct.');
set(leg,...
    'Location','East',...
    'FontSize',font_size);
%    '{\alpha}_{max}=',num2str(max_alpha∞),', '...
end
fprintf('End\n############################\n');
```

B. Outcrops



Figure 49: Top: Outcrop location CM001. Red arrow shows location of the sample. Bottom: Outcrop location CM002.



Figure 50: Top: Outcrop of sample CM003. Foreground: enthusiastic geologist acting as scale. Bottom: Sample CM004.

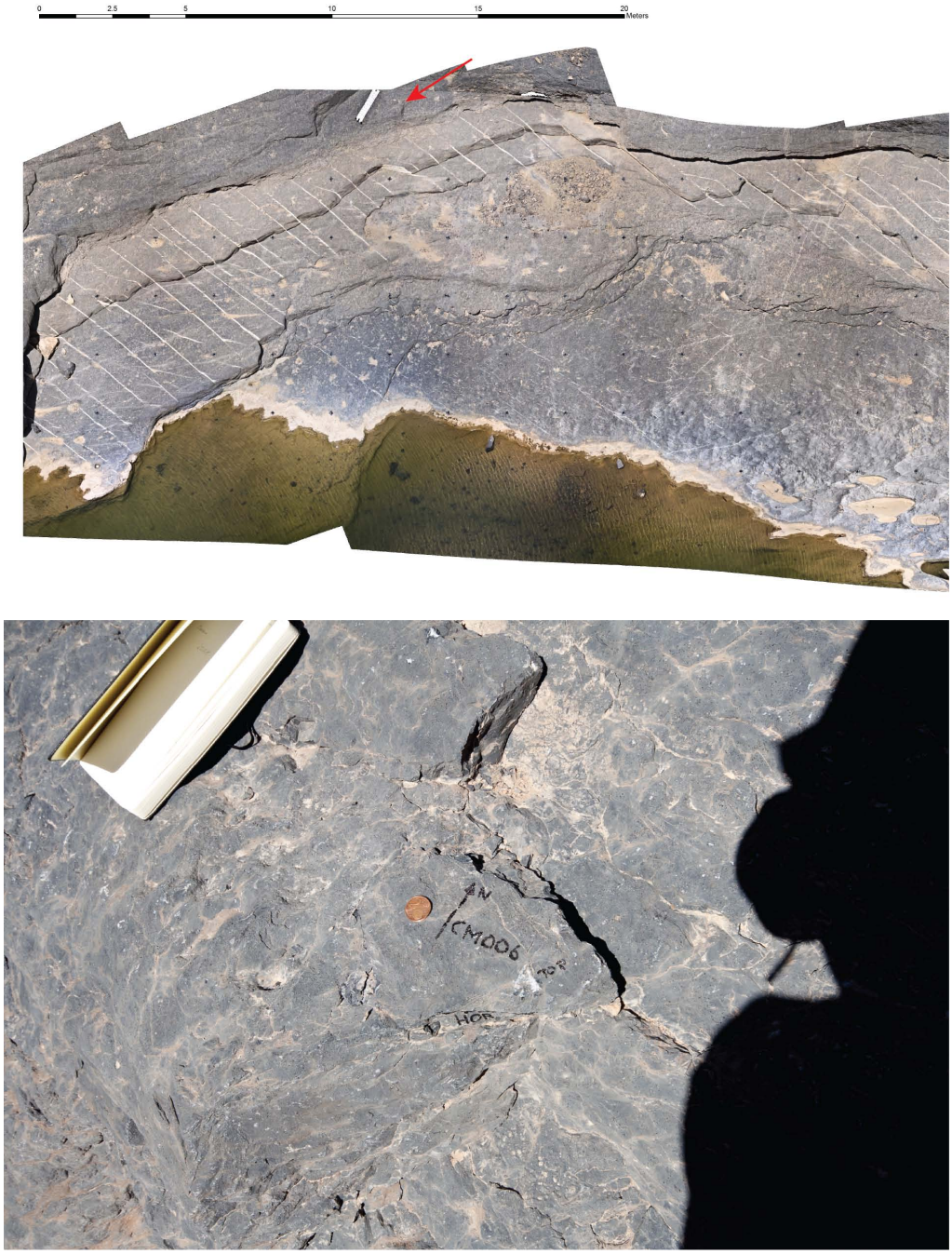


Figure 51: Top: Stitched overview image of western part of Swimmingpool Pavement (Wüstefeld, 2010). The Arrow points the sampling spot of CM006. Bottom: Detail image of Sample CM006.



Figure 52: Top: Outcrop CM007. Bottom: Outcrop CM008.

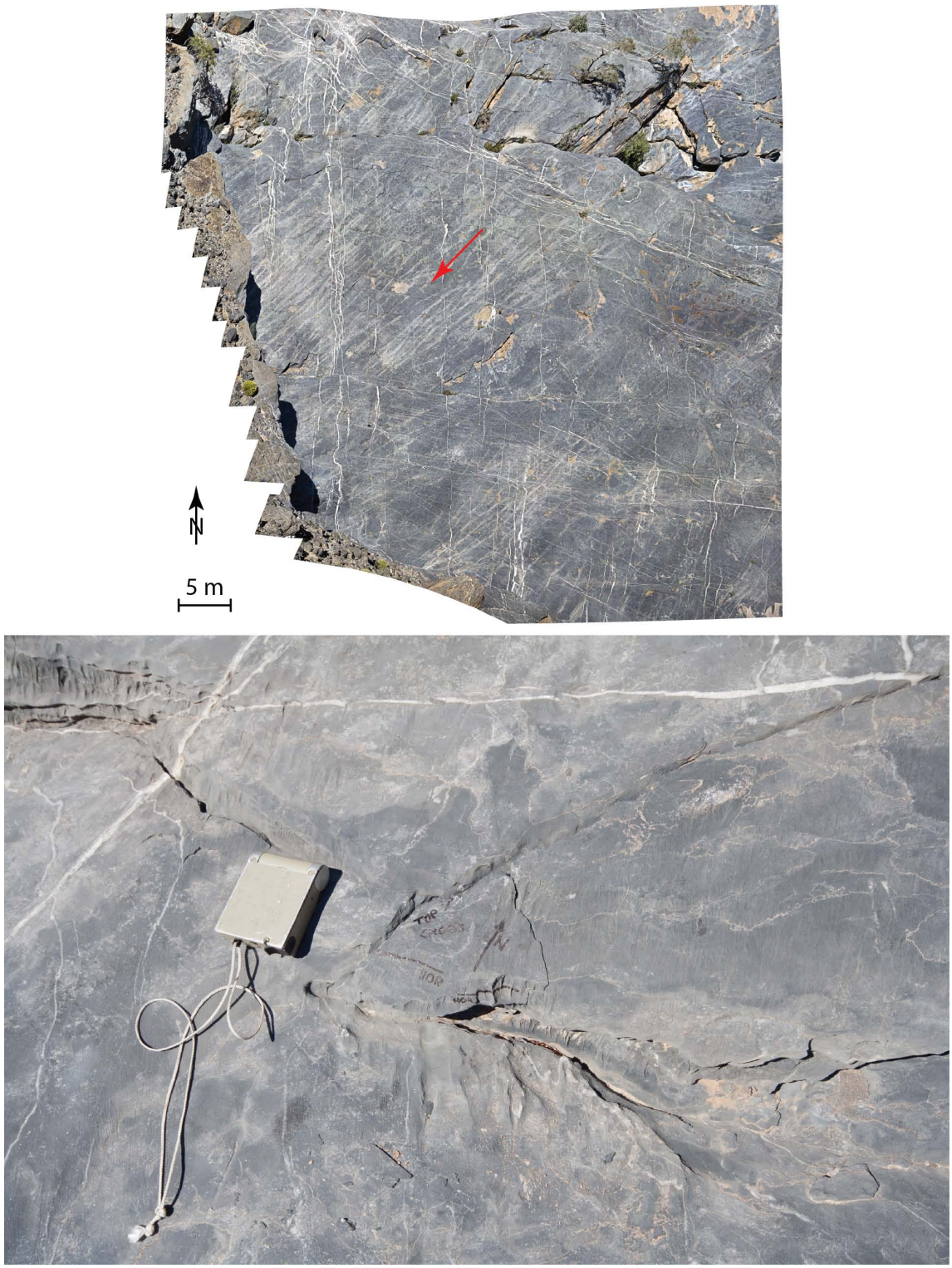


Figure 53: Top: Stitched outcrop panorama of Lower Gorge Pavement (Raith, 2010). The red arrow marks the sampling spot of sample CM009. Bottom: detail image of sample CM009.



Figure 54: Top: Outcrop CM010. Bottom: Outcrop CM011.

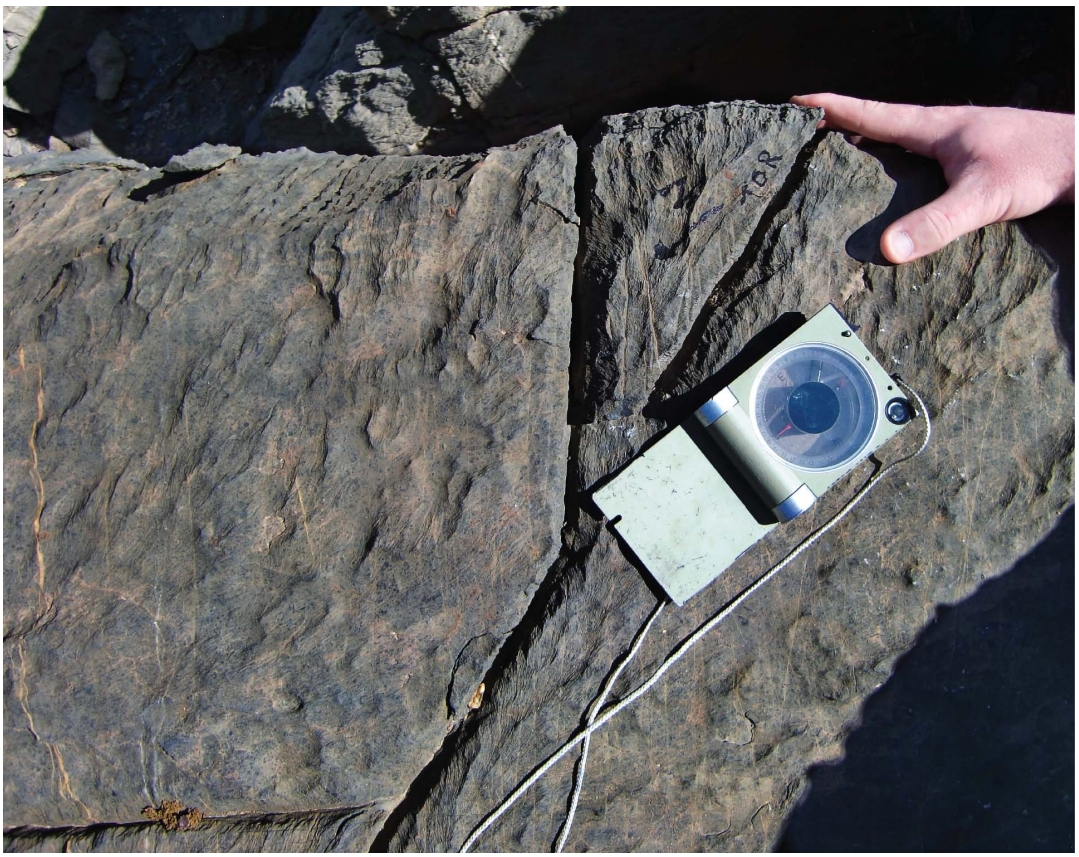


Figure 55: Sample CM012.

C. Additional material

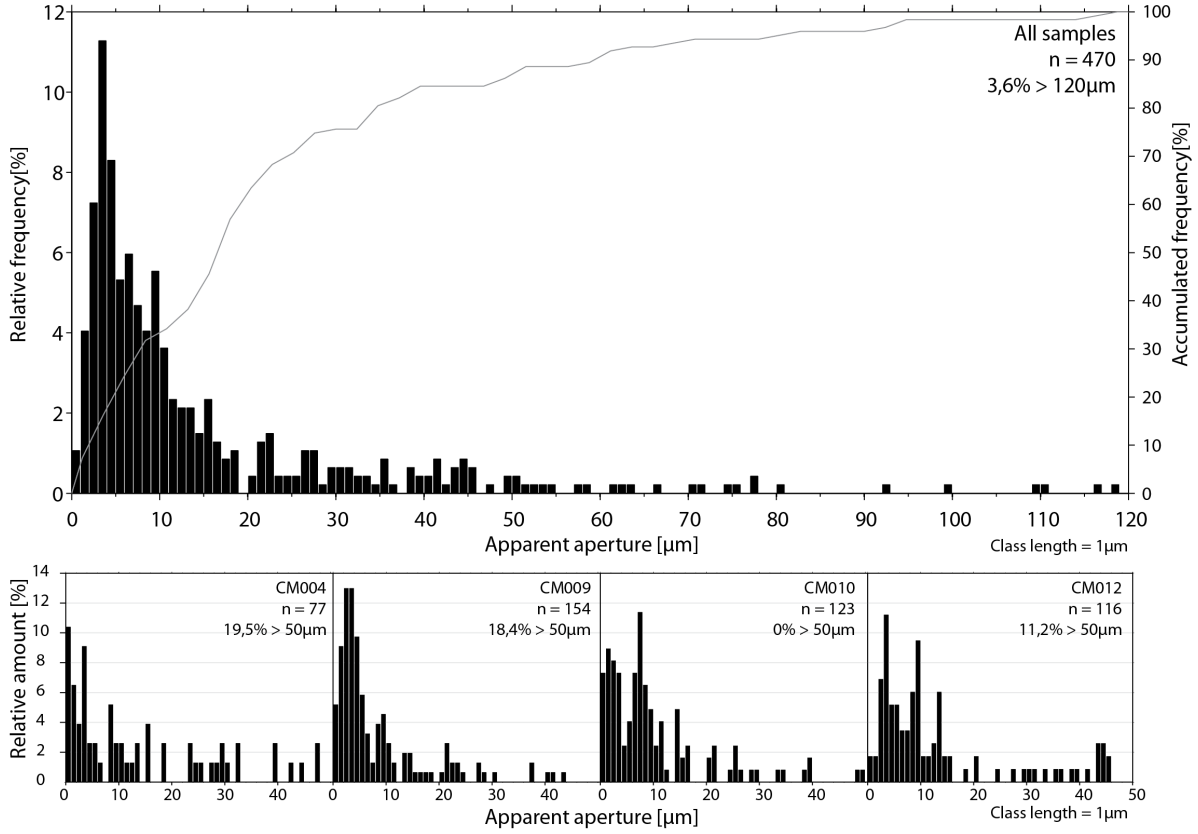


Figure 56: Top: Apparent aperture distribution of all measured samples (CM004,CM009,CM010,CM012). Bottom: Individual distributions of each sample. Note that all histograms are cut off at 120 μm. The amount of veins above this aperture are noted in the top right corner of each histogram.



Figure 57: Stitched image of a microvein in thin section C04.1 showing shear indicators at several intersections. See text (Page 50) for further information.

D. Field measurements

Type	Azimuth	Dip	Comment
Discotheque Pavement 40Q 514424 2565846			
Bedding	241	20	
Bedding	246	10	
Bedding	251	12	
Bedding	250	12	
Bedding	259	16	
Bedding	261	14	
Bedding	253	15	
Bedding	263	12	
Bedding	259	14	
Bedding	274	15	
Microvein	48	77	
Microvein	95	70	
Microvein	354	85	
Microvein	44	65	
Microvein	49	73	
Microvein	266	82	
Microvein	325	73	
Microvein	48	71	
Microvein	353	80	
Microvein	356	80	
Microvein	92	51	
Microvein	46	76	
Microvein	102	74	
Microvein	347	83	
Microvein	103	63	
Microvein	252	79	
Microvein	102	78	
Microvein	96	71	
Microvein	46	63	
Microvein	349	80	
Microvein	262	81	
Microvein	345	84	
Microvein	168	88	
Microvein	349	85	
Microvein	349	86	
Microvein	345	87	
Upper Discotheque Pavement 40Q 514772 2566120			
Vein	182	80	
Vein	176	86	
Vein	185	76	
Bedding	276	14	
Bedding	248	20	
Bedding	295	15	
Bedding	260	15	
Bedding	274	20	
Bedding	278	20	
Bedding	267	17	

Type	Azimuth	Dip	Comment
Hail al Shaz 1 40Q 527854 2561473			
Microvein	50	58	
Microvein	52	60	
Microvein	288	76	
Microvein	39	61	
Microvein	188	56	
Microvein	42	49	
Microvein	57	60	
Microvein	280	74	
Microvein	319	57	
Microvein	35	64	
Microvein	53	60	
Vein	294	77	
Vein	33	61	
Vein	191	67	
Vein	54	57	
Bedding	161	9	
Bedding	189	7	
Bedding	174	11	
Bedding	185	15	
Bedding	162	10	
Bedding	177	7	
Hail al Shaz 2 40Q 527878 2561487			
Vein	42	65	
Microvein	289	73	
Vein	1	67	
Microvein	40	68	
Microvein	50	62	
Microvein	44	69	
Microvein	32	84	
Microvein	44	63	
Hail al Shaz 3 40Q 528517 2562352			
Bedding	172	13	
Bedding	176	14	
Bedding	189	13	
Bedding	156	13	
Microvein	25	63	
Microvein	190	85	
Microvein	30	59	
Microvein	50	67	
Microvein	27	70	
Microvein	47	72	
Microvein	47	66	
Microvein	317	70	
Microvein	294	68	
Hail al Shaz 4 40Q 528187 2561762			
Bedding	197	18	

Type	Azimuth	Dip	Comment
Wadi Dham 1 40Q 507616 2569429			
Bedding	213	10	
Bedding	236	11	
Bedding	216	5	
Bedding	212	10	
Bedding	227	10	
Bedding	200	87	
Fracture Edge	4	85	
Fracture Edge	181	82	
Fracture Edge	182	82	
Fracture Edge	349	77	
Wadi Dham 2 40Q 508017 2569565			
Microvein	188	17	
Microvein	222	1	
Microvein	356	81	
Microvein	175	14	
Microvein	357	82	
Microvein	209	6	
Microvein	359	74	
Microvein	204	6	
Microvein	356	76	
Vein	191	15	
Wadi Dham 3 40Q 507138 2568957			
Bedding	157	18	
Vein	350	80	
Vein	181	70	a=3cm
Vein	354	70	a=1cm
Wadi Dham 4 40Q 507138 2568957			
Microvein	62	85	
Microvein	60	80	
Microvein	345	79	
Microvein	57	82	
Microvein	347	74	
Microvein	61	84	
Lower Gorge Pavement 40Q 513621 2573456			
Microvein	317	45	
Microvein	317	74	
Microvein	330	69	
Microvein	198	29	
Microvein	319	87	
Microvein	320	77	
Microvein	20	56	
Microvein	255	54	
Microvein	311	89	
Microvein	252	50	
Microvein	11	66	
Microvein	157	87	
Vein	274	83	

Type	Azimuth	Dip	Comment
Lower Gorge Pavement 40Q 513632 2573421			
Microvein	280	74	
Microvein	168	89	
Microvein	305	84	
Microvein	184	82	
Microvein	188	84	
Microvein	298	75	
Microvein	335	80	
Microvein	185	73	
Microvein	193	78	
Vein	54	54	a=4mm
Vein	173	52	a=4mm
Vein	260	48	a=4mm
Gorge Muti Konglomerat 40Q 513742 2573533			
Microvein	256	82	
Microvein	17	77	
Microvein	15	70	sinistral en echelon set
Gorge Muti Shale 40Q 513823 2573017			
Bedding	138	4	
Microvein	257	74	
Microvein	6	64	
Microvein	250	56	
Microvein	12	86	breaking edge
Microvein	286	73	breaking edge
Hail al Shaz Nahr Umr 40Q 523755 2562367			
Microvein	26	85	
Bedding	201	4	
Bedding	192	3	
Bedding	180	3	
Bedding	184	8	
Bedding	192	6	
Microveins	46	70	yellow
Microveins	53	72	yellow
Microveins	205	80	yellow
Microveins	40	76	yellow
Microveins	53	61	yellow
Microveins	52	62	yellow
Microveins	72	77	yellow
Microveins	307	76	dark blue
Microveins	308	77	dark blue
Microveins	309	72	dark blue
Microveins	306	79	dark blue
Microveins	300	77	dark blue
Microveins	304	73	dark blue
Microveins	41	73	yellow
Microveins	47	72	yellow
Microveins	35	72	yellow, no-shear
Microveins	6	62	white-beige

E. Data DVD